

Modeling and Maximum Power Extraction from Perovskite Solar Cell



By Author

Zeeshan Yousaf

(Registration No: 00000330588)

A thesis submitted to the National University of Sciences and Technology, Islamabad,

in partial fulfillment of the requirements for the degree of

Master of Science in
Electrical Engineering

Supervisor: Dr. Azhar Ul Haq

College of Electrical and Mechanical Engineering

National University of Sciences & Technology (NUST)

Islamabad, Pakistan

(August 2024)

THESIS ACCEPTANCE CERTIFICATE

It is certified that final copy of MS/MPhil thesis written by Mr. Zeeshan Yousaf (Registration No. 00000330588) Entry-2020, of (College of E&ME) has been vetted by the undersigned, found complete in all respects as per NUST Statutes/Regulations, is free of plagiarism, errors, and mistake and is accepted as partial fulfillment for award of MS degree. It is further certified that necessary amendments as pointed out by GEC member of the scholar have also been incorporated in the said thesis.

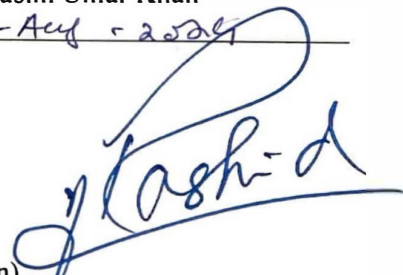
Signature: 

Name of Supervisor Dr. Azhar Ul Haq

Date: 15 - Aug - 2024

Signature (HoD): 
Dr. Qasim Umar Khan

Date: 15 - Aug - 2024

Signature (Dean) 
Brig Dr. Nasir Rashid

Date: 15 AUG 2024

DEDICATION

This thesis is dedicated to Allah Almighty, the most Merciful. I then dedicate this thesis to my parents Mr. and Mrs. Muhammad Yousaf who have invested in me with their efforts, love, care, and financial support in completing this milestone.

ACKNOWLEDGEMENTS

In the name of the ALLAH, the most Gracious, the most Merciful. All the praise be to Allah Almighty, the God of the whole universe and the Master of the Day of Judgement. First, and foremost, I am grateful and will be thankful to Allah, The Almighty, The Compassionate, for helping me in completing this thesis with His Blessings.

In completing and succeeding this thesis, I would like to thank my supervisor, Mr. Dr. Azhar Ul Haq, for his extensive and excellent assistance, guidance, and support. I would like to appreciate and express my gratitude to Dr. Azhar Ul Haq for his valuable supervision, guidance, kindness, motivation, and encouragement during the whole study which helped in attaining the required objectives to complete this research and dissertation.

I want to thank and express my gratitude to N. E. Courtier, J. M. Cave, A. B. Walker, G. Richardson, and J. M. Foster who developed MATLAB based environment 'IonMonger' in 2019 for the researchers to investigate the field of Perovskite Solar Cells further and in 2022, W. Clark with his colleagues, improved this. By using this IonMonger, the impact of scan rate on the J – V hysteresis in a three-layered perovskite solar cell is understood and evaluated. This algorithm helped me generate J-V hysteresis, understand the main causes of it, and analyze the impact of scan rates on the performance of PSCs. This effort of Courtier et.al and W. Clark with his colleagues is highly appreciated and encouraged.

I highly appreciate and deepest thanks to my parents Mr. and Mrs. Muhammad Yousaf for their immense support in every walk of life. I would like to express my heartiest acknowledgment and thanks to my parents for putting a lot of effort, love, and investment

into my education, and in my life. Without the kindness, blessings, and support of my parents, I could never have achieved any goal.

In the end, I would like to thank many colleagues in the Perovskite Solar Cell community who have contributed a lot of effort in this research area for the improvement and progress with their deep investigations, discussions, and recommendations.

ABSTRACT

This study depicted maximum power extraction from perovskite solar cells under the noticeable current density – voltage (J-V) hysteresis. The main objectives of this study were to analyze the impact of scan rate on the J-V characteristics of PSC, and then to develop a maximum power point tracking algorithm that could be efficient enough to predict the most suitable maximum power point, even under the high levels of J-V hysteresis. IonMonger, a MATLAB-based environment developed by Courtier et.al, was used to study the impact of scan rate and its direction on the J-V characteristics of a three-layered PSC (Electron transport layer, Perovskite absorber layer, Hole transport layer). It was observed that by increasing the scan rate from 50mV/s to 200mV/s, the losses in the current density, at the interfaces, due to interfacial recombination increase, and ultimately the hysteresis level increases. The hysteresis index is used as a parameter to evaluate the hysteresis level present in the J-V characteristics of PSC. When the interfacial recombination rates and effective doping densities of ETL and HTL were tuned, the hysteresis was reduced to the minimum and the impact of scan rate and direction on the J-V characteristics became negligible. A Random Forest Regression model is used to develop an MPPT that could track the most suitable MPP even under a high level of hysteresis. It was depicted in this study that even at high values of J-V hysteresis, the RFR – MPPT predicted the MPP characteristics of PSC efficiently and did not overestimate and underestimate the performance of PSC. 0.42mW/cm² or 1.9% of MPP-power difference was noticed in the prediction of MPP when there was a high level of hysteresis content present and when there was negligible hysteresis present. The credibility of RFR – MPPT was also investigated by comparing it with the two highly performed MPPTs in the solar industry, and the RFR – MPPT performed very accurately and efficiently as compared to Perturb & Observe and Incremental Conductance algorithms.

Keywords: RFR – MPPT, three-layered perovskite solar cell, interfacial recombination, J-V hysteresis, scan rate, Electron Transport layer (ETL), Hole Transport Layer (HTL).

TABLE OF CONTENTS

| | |
|---|-------------|
| ACKNOWLEDGEMENTS | II |
| ABSTRACT | IV |
| TABLE OF CONTENTS | V |
| LIST OF TABLES | VIII |
| LIST OF FIGURES | IX |
| LIST OF ABBREVIATIONS | XI |
| CHAPTER 1: INTRODUCTION | 1 |
| 1.1 Background and Scope | 2 |
| 1.1.1 Related Technologies | 5 |
| 1.2 Problem Statement | 11 |
| 1.3 National Needs | 12 |
| 1.4 Research Motivation | 13 |
| 1.5 Research Objectives | 14 |
| 1.6 Applications of the Research | 15 |
| 1.7 Thesis Organization | 16 |
| CHAPTER 2: FUNDAMENTALS AND LITERATURE REVIEW | 18 |
| 2.1 Perovskite Solar Cell's Background | 19 |
| 2.1.1 Materials of Perovskite | 21 |
| 2.1.2 Development of Perovskite Solar Cell | 23 |
| 2.2 Perovskite Solar Cells and Hysteresis | 24 |
| 2.3 Influential Factors Impacting Hysteresis in Perovskite Solar Cells | 24 |
| 2.3.1 Cell Architecture | 24 |
| 2.3.2 Perovskite Material | 25 |
| 2.3.3 Impact of Different Testing Conditions | 25 |
| 2.4 Possible Origins of Hysteresis in Perovskite Solar Cells | 26 |
| 2.4.1 Ferroelectric Effect | 26 |
| 2.4.2 Unbalance Charge Carrier Transport | 27 |
| 2.4.3 Migration of Ion Vacancy | 28 |
| 2.4.4 Trap Assisted Charge Recombination | 28 |
| 2.4.5 Challenges to These Possible Origins | 29 |
| 2.5 Performance Parameters of Solar Cells | 29 |
| 2.5.1 V_{oc} – Open Circuit Voltage | 30 |
| 2.5.2 I_{sc} – Short Circuit Current | 31 |
| 2.5.3 FF – Fill Factor | 31 |
| 2.5.4 Output Current | 31 |
| 2.5.5 Maximum Power | 32 |
| 2.5.6 Quantum Efficiency | 32 |

| | | |
|---|--|-----------|
| 2.5.7 | J-V Plot – Current Density-Voltage Characteristics | 32 |
| 2.6 | Maximum Power Point Tracking (MPPT) Techniques | 33 |
| 2.6.1 | Perturb and Observe (P&O) | 33 |
| 2.6.2 | Incremental Conductance (IC) | 34 |
| 2.6.3 | Fuzzy Logic Control (FLC) | 36 |
| 2.6.4 | Neural Network (NN) | 36 |
| 2.7 | Related Research | 36 |
| 2.7.1 | Modeling Solution of Vacancy Motion and Charge Transport in PSCs | 37 |
| 2.7.2 | Modeling of PSC with respect to Structural Similarity | 37 |
| 2.7.3 | Progress in PSCs | 38 |
| 2.7.4 | Behavioral Modeling of PSCs | 38 |
| 2.7.5 | Tracking of MPP by a Predictive Algorithm | 39 |
| 2.7.6 | Hysteresis in PSCs caused by Ion Migration’s Numerical Modeling | 39 |
| 2.7.7 | MPPT for Measurement of PCE of Metastable PSCs | 40 |
| 2.8 | Limitations and Bottlenecks of the Existing Work | 40 |
| 2.9 | Summary | 41 |
| CHAPTER 3: MODELING OF PEROVSKITE SOLAR CELL IN MATLAB | | 42 |
| 3.1 | Drift Diffusion Method | 43 |
| 3.1.1 | Mathematical Modeling and Equations | 43 |
| 3.2 | Grid Discretization | 51 |
| 3.3 | Implementation in MATLAB | 52 |
| 3.3.1 | Input Parameters and Initial Conditions | 53 |
| 3.3.2 | Non-Dimensionalization of Model Parameters | 55 |
| 3.3.3 | Numerical Solver | 57 |
| 3.4 | Summary | 58 |
| CHAPTER 4: RANDOM FOREST REGRESSION BASED MPPT | | 59 |
| 4.1 | Random Forest Regression – RFR-MPPT | 59 |
| 4.1.1 | Bootstrap Sampling | 60 |
| 4.1.2 | Construction of Decision Trees | 60 |
| 4.1.3 | Prediction Aggregation | 61 |
| 4.1.4 | Data Collection and Building of Random Forest (RF) Model | 62 |
| 4.1.5 | Prediction Strategy for RFR-MPPT | 64 |
| 4.2 | Summary | 65 |
| CHAPTER 5: RESULTS AND DISCUSSION | | 66 |
| 5.1 | Impact of Scan Rate on J – V Hysteresis | 67 |
| 5.1.1 | At the Scan Rate of 50mV/s | 68 |
| 5.1.2 | At the Scan Rate of 100mV/s | 69 |
| 5.1.3 | At the Scan Rate of 150mV/s | 71 |
| 5.1.4 | At the Scan Rate of 200mV/s | 72 |
| 5.1.5 | Impact of Parameter’s Changing on J – V Hysteresis | 73 |
| 5.2 | Prediction of MPP and Extraction of Maximum Power | 76 |
| 5.2.1 | Extraction of Maximum Power under J – V Hysteresis | 77 |
| 5.2.2 | Extraction of Maximum Power under Negligible J – V Hysteresis | 79 |
| 5.3 | Comparison of RFR – MPPT with Conventional MPPTs | 80 |

| | |
|--|-----------|
| 5.3.1 P&O – Perturb and Observe | 81 |
| 5.3.2 IC – Incremental Conductance | 82 |
| 5.4 Summary | 84 |
| CHAPTER 6: CONCLUSION AND RECOMMENDATIONS | 85 |
| REFERENCES | 88 |

LIST OF TABLES

| | Page No. |
|--|-----------------|
| Table 3. 1: Input Parameters Used | 54 |
| Table 5. 1: Impact of Scan Rate on Hysteresis Before Changing Input Parameters | 67 |
| Table 5. 2: Optimization of PSC's Parameters..... | 74 |
| Table 5. 3: Results obtained after changing PSC's Input Parameters | 75 |
| Table 5. 4: Prediction of Maximum Power Point Values by implementation of RFR- MPPT under Noticeable Hysteresis | 77 |
| Table 5. 5: Prediction of Maximum Power Point by implementation of RFR-MPPT Values under Minimum Hysteresis..... | 79 |
| Table 5. 6: MPP Tracking by Implementing P&O Algorithm under Noticeable Hysteresis | 81 |
| Table 5. 7: MPP Tracking by Implementing IC Algorithm under Noticeable Hysteresis | 83 |

LIST OF FIGURES

| | Page No. |
|---|----------|
| Figure 1. 1: CdTe PV Cell’s layered structure..... | 6 |
| Figure 1. 2: Schematic View of CIGS Solar Cell | 8 |
| Figure 1. 3: Schematic View of QD Solar Cell | 10 |
| Figure 1. 4: Schematic of DSSC..... | 11 |
| | |
| Figure 2. 1: Planar shape of Perovskite Solar Cell | 20 |
| Figure 2. 2: ABX ₃ Structure of PSC | 21 |
| Figure 2. 3: Map of the structure of ABX ₃ considering “t” and “u”..... | 22 |
| Figure 2. 4: PV and IV Curves with Labels..... | 30 |
| Figure 2. 5: P&O Algorithm | 34 |
| Figure 2. 6: IC Algorithm | 35 |
| | |
| Figure 3. 1: Three-Layered Planar Architecture of PSC..... | 43 |
| Figure 3. 2: Implementation Flow Chart in MATLAB..... | 53 |
| | |
| Figure 4. 1: RFR-MPPT's Flow Chart | 62 |
| | |
| Figure 5. 1: Light Intensity (Irradiance) | 67 |
| Figure 5. 2: Graphical Representation of Hysteresis at a Scan Rate of 50mV/s. (a) Applied Voltage is displayed with respect to time taken for the complete process. (b) J-V characteristic curve with the current-density Losses due to Interfacial Losses. (c) J-V characteristic curve showing the hysteresis content present. (d) Hysteresis content showing in PV curve..... | 69 |
| Figure 5. 3: Graphical Representation of Hysteresis at a Scan Rate of 100mV/s. (a) Applied Voltage is displayed with respect to time taken for the complete process. (b) J-V characteristic curve with the current-density Losses due to Interfacial Losses. (c) J-V characteristic curve showing the hysteresis content present. (d) Hysteresis content showing in PV curve..... | 70 |
| Figure 5. 4: Graphical Representation of Hysteresis at a Scan Rate of 150mV/s. (a) Applied Voltage is displayed with respect to time taken for the complete process. (b) J-V characteristic curve with the current-density Losses due to Interfacial Losses. (c) J-V characteristic curve showing the hysteresis content present. (d) Hysteresis content showing in PV curve..... | 71 |
| Figure 5. 5: Graphical Representation of Hysteresis at a Scan Rate of 200mV/s. (a) Applied Voltage is displayed with respect to time taken for the complete process. (b) J-V characteristic curve with the current-density Losses due to Interfacial Losses. (c) J-V characteristic curve showing the hysteresis content present. (d) Hysteresis content showing in PV curve..... | 73 |

| | |
|---|----|
| Figure 5. 6: Results obtained after changing the PSC's Parameters that lead to minimum hysteresis at each Scan Rate | 76 |
| Figure 5. 7: RFR-MPPT's Prediction and Tracking of Maximum Power Point, under hysteresis, shown in red circle on the J-V curves at Scan Rate (a) 50mV/s (b) 100mV/s (c) 150mV/s (d) 200mV/s. 'U' means 'upper line showing Reverse Scan', 'B' denoting 'Bottom line showing Forward Scan' | 78 |
| Figure 5. 8: RFR-MPPT's Prediction and Tracking of Maximum Power Point, under hysteresis, shown in red circle on the J-V curves at Scan Rate (a) 50mV/s (b) 100mV/s (c) 150mV/s (d) 200mV/s. 'U' means 'upper line showing Reverse Scan', 'B' denoting 'Bottom line showing Forward Scan' | 80 |
| Figure 5. 9: MPP Tracking by P&O under Noticeable Hysteresis at Scan Rate (a) 50mV/s (b) 100mV/s (c) 150mV/s (d) 200mV/s..... | 82 |
| Figure 5. 10: MPP Tracking by IC under Noticeable Hysteresis at Scan Rate (a) 50mV/s (b) 100mV/s (c) 150mV/s (d) 200mV/s..... | 83 |

LIST OF ABBREVIATIONS

| | |
|------|-------------------------------------|
| PSC | Perovskite Solar Cell |
| PV | Photovoltaic |
| Voc | Open – Circuit Voltage |
| MPPT | Maximum Power Point Tracking |
| J | Current density |
| HTL | Hole Transport Layer |
| V | Voltage |
| Pmax | Maximum Power |
| ETL | Electron Transport Layer |
| Vmpp | Maximum Power Point Voltage |
| BOS | Balance of the System |
| FF | Fill Factor |
| Jsc | Short–Circuit Current |
| HI | Hysteresis Index |
| Jmpp | Maximum Power Point Current Density |
| R | Recombination Rate |
| G | Irradiance / Light Intensity |
| MPP | Maximum Power Point |

| | |
|----------|-----------------------------|
| PCE | Power Conversion Efficiency |
| q | Charge |
| P&O | Perturb and Observe |
| V_{bi} | Built-in Voltage |
| RFR | Random Forest Regression |
| IC | Incremental Conductance |

CHAPTER 1: INTRODUCTION

This chapter is about the introduction of solar photovoltaic cells. The complete background of solar cells, their evolution, and their progress are discussed in detail. Furthermore, the scope, problem statement, national needs, motivation behind the research in this specific area, research objective, and its possible application are discussed in this chapter.

One of the most serious difficulties is meeting the world's expanding energy needs. As the world's population rises and living standards improve, so does overall energy consumption. Today, fossil fuels provide most of the energy generated by humans; yet, fossil fuel reserves, the primary source of energy, are finite. Global warming's major cause is the use of fossils as it has bad impacts on the environment. Resources of fossil fuel are in short supply. It is very important to depend on commercially viable and ecologically benign technology. If energy is produced from the latest technologies like photovoltaic cells has developed as an ecologically clean, cost-competitive, and sustainable energy source. Solar energy provides all the energy on the planet in different forms. The sun provides warmth and sustenance to every living thing. Energy from the sun is used by people in many ways. At any one time, approximately 125000TW of energy from solar strikes our earth. Therefore, for power generation, energy from solar has great advantages as it is renewable, abundant, and clean.

Latest technologies like solid-state photovoltaic cells (PV), are utilized to directly collect solar energy and transform it into electrical power. PVs have evolved as a comparatively sustainable, ecologically clean, and cost-competitive energy source evolution of the industry, on the other hand, a constant decline in cells is happening and module costs are getting us nearer to the grid parity than ever before. For cost reduction and boosting efficiency to achieve the full capacity of photovoltaic energy, there is still much work to be done. A photovoltaic panel is created using PV cells which make modules and photovoltaic arrays are formed. The balance of the system (BOS) is made up of many components such as batteries, cables, fuses, inverters, and so on. The sun tracking mechanism is employed in some systems, which raises the cost, but the efficiency of the

module increases. The performance is affected when there is cloudy weather or in the dark because the cell does not work.

1.1 Background and Scope

Energy is critical to humanity's technical and socioeconomic growth. Most people depend on coal, natural gas, and oil to meet their energy demands; however, the resources of fossil fuels are finite. The world's supply of fossil fuels will run out, and they will become costly. Greenhouse gases are emitted by the usage of fossil fuels, causing global warming, and polluting the water, soil, and air. As the world's population grows, so does the worldwide need for energy, as electricity is both a lifeline and a status symbol in civilized nations. Petroleum reserves, a well-known important energy resource, are being used extensively as the human population grows and industrial growth accelerates. Humanity is on the verge of an energy disaster. To deal with the situation, new energy sources must be developed to investigate and properly utilize renewable resources. Renewable energy resources, which primarily include hydropower, geothermal, solar, hydrogen, biogas, and oceans, provide environmentally friendly fossil fuel alternatives. These sources will never deplete and emit no greenhouse emissions or other pollutants. Solar energy is plentiful, inexpensive, renewable, clean, wasteless, and a good source of energy. Energy conversion of solar to electricity is directly using solar cells, which are electrical devices (SC). SC is mostly made of silicon. Silicon is one of the most available elements on Earth. Silicon cells are physically simple and have no moving parts, they may function for several years with little improvement and can perform well in shading conditions [1]. Initially, French physicist E. Becquerel discovered the phenomena of photovoltaics in 1839. Becquerel discovered the formation of a voltage when he focused sunlight onto an electrode while working with a cell having two electrodes immersed in a solution that was conducting electricity. Becquerel noticed, after placing the cell under light, that power output is enhanced [2]. A solar steam engine was proposed by a French mathematician A. Mouchet, in 1860, and developed a solar-powered engine for the first time through the efforts of Abel Pifre. The prototypes of that engine are modern parabolic dish collectors. The PV effect in selenium is observed by Richard Evans Day and William Grylls Adams [3]. A device named “Bolometer” was invented by Samuel P. Langly in 1880

[4]. The first solar cell, having an efficiency of 1%, was made from selenium wafers in 1838 by Charles Fritts, a scientist from America, who used an extremely thin gold coating on the semiconductor Selenium to form the connections [5]. Several other scientists and researchers proceeded further in the development of this technology. In 1904 it was discovered by Wilhelm Hallwachs that it is photosensitive when Copper is combined with Cuprous Oxide [6]. A useful method for monocrystal silicon was invented by Jan Czochralski which served as a cornerstone for modern Si technology in 1918 [7]. In 1953, the first solar cell was created, having 4 percent efficiency, by a scientist's group at Bell Labs, United States [8]. Cadmium sulphide developed by [9] had similar conversion efficiency in the same era. This advancement and improvement are still ongoing, and several generations and varieties of PV cells have been generated in the contemporary period. The usage of photovoltaic solar cells has recently expanded, and several research organizations and PV companies are working to expand the use of solar energy. The most recent literature provides the highest confirmed one sun, concentrated module efficiencies, and other related parameters [10].

To catch heat radiation, the first solar collector was built by Horace-Benedict de Saussure in 1767, a Swiss physicist. Saussure's box, which could achieve temperatures of 230° F, was widely considered the first solar oven. In 1873, Willoughby Smith discovered selenium's photoconductivity. Willoughby Smith discovered that selenium creates solar energy in 1876, which extended the original discovery. The use of selenium was attempted in the construction of solar cells. The cell failed miserably, but a crucial concept was learned electricity can be obtained from light without the use of moving parts or heat of a solid. The findings paved the way for future advances in solar power history. Several innovations to the progress of solar energy utilization were created between 1883 and 1891, including Light Discoveries and Solar Cells. The first solar cell was introduced in 1883. Selenium wafers were to be wrapped around the cell. It was discovered in 1887 by a scientist named Heinrich Hertz that a spark occurred between two electrodes due the UV radiation. A collector having copper boxes and coils was designed by William J. Baileys in 1908. The collector outperformed the previous one, in which the insulation of copper was a key difference. Today's devices are designed using these advancements. Albert Einstein explained the photoelectric effect in a research article in 1905, but there was no

experimental proof for it. The photoelectric effect was empirically validated in 1916 by a physicist named Robert Millikan. Following WWII, the popularity of solar power in the United States skyrocketed in 1947, and equipment of solar became popular among Americans. Solar energy equipment was in high demand. To power, the equipment of space exploration like satellites, the energy from solar was utilized and it was published in 1958. The efficiency and production cost of solar were under discussion for almost two decades, from 1959 to 1970. During that time, the maximum of 14 percent efficiency was the solar cells, and the cost of manufacturing was incompatible with the efficiency because it was too expensive to manufacture solar cells but had low efficiency. A corporation known as Exxon manufactured a low-cost and efficient solar panel in the 1970s, and the landmark moment of solar energy history started. The United States government founded the Solar Energy Research Institute in 1977 to encourage the use of solar energy. Other governments rapidly followed suit throughout the world. Paul Macready created the first solar-powered airplane in 1981. More than 1600 cells were employed on the airplane's wings. It took off from France and flew to the United Kingdom. The first solar-based automobiles were developed in Australia in 1982. From 1986 to 1999, huge developments and construction were made in terms of solar energy facilities. By 1999, the biggest plant had been built, generating 20 kilowatts, and the most efficient PV cell was made, having an efficiency of 36%. The government of Spain halted support for the country's sustained solar power generation as there was a worldwide financial crisis occurred in 2008. This created a huge bad impact on industry, worldwide. Two solar companies, Solyndra and Evergreen, went bankrupt in 2010 because the demand for their products was reduced. There has been a huge investment in the installations of solar for utility purposes in the last few years. One of the world's largest solar parks, in 2012, is in Golmud China having a 200 megawatts capacity. A solar park is following the previous one in Gujarat, India, in which solar farms are distributed across Gujarat with having 605 megawatts capacity. The great wall of solar power is the world's largest solar farm to date. It is situated in Tengger Desert, China. This solar farm has a capacity of 1.5 gigawatts of power and has a lot of room to expand.

1.1.1 *Related Technologies*

A thin-film PV cell is composed of one or more thin layers of PV material deposited on a substrate like plastic, metal, or glass. For commercial applications, thin-film PV cells are used (a-Si, TF-Si). It is much thinner than first-generation silicon cells, with thickness ranging from a few nanometers to tens of micrometers, whereas silicon wafers are about 200 μm big. Therefore, these cells are more drag-free, lighter, and flexible. Integrated photovoltaic systems are built by this cell. A material, glazing and semi-transparent that can be bonded onto windows, is also built by this technology. Some of the largest PV facilities employ a stiffed thin-film PV panel in commercial applications. It is always a less costly technology than the technology of silicon cells, but less efficient. With time, these cells improved a lot, topped with 21% lab efficiency of CIGS and CdTe. It is now becoming the dominant material that can be used in many PVs [10]. Regardless of these advances, thin-films in worldwide solar manufacture have never exceeded 20% in the last two decades and have lately decreased to approximately 9% in 2013 [11]. Dye-sensitized, organic, polymer, quantum dot, nanocrystal, copper zinc tin sulphide, perovskite, and micro-morph PV cells, are frequently referred to as third-generation photovoltaic cells. These technologies are under development and have limited availability commercially.

1.1.1.1 CdTe – Cadmium Telluride Solar Cells

CdTe is a PV technology using cadmium telluride, a semiconductor having a thin film that absorbs and transforms sunlight into power [12]. It is the only technology in thin film that is less expensive than typical crystalline silicon solar cells [13]. This technology requires the least amount of water, has the smallest footprint of carbon, and has the shortest energy payback period of any solar technology [14]. The payback period of energy for CdTe is less than a year, allowing for carbon reduction faster while avoiding energy shortages. By recycling, when the cells are at the end of their lifetime, the risk of toxicity of cadmium to the environment can be reduced [15]. The scalability of CdTe may be limited in the industry in the midterm due to the use of rare materials. The exceptional quantity of tellurium in the earth's crust, of which telluride is the anionic form, is equivalent to that of platinum and contributes to the module's cost [16]. Topaz or the other largest solar farms

in the world uses CdTe photovoltaics as powerplants. Half of the thin film market or even more is accounted with the technology of CdTe in 2013 and contributed the PV output of 5.1% worldwide [17]. First Solar, situated in Tempe, Arizona, is a well-known producer of CdTe technology.

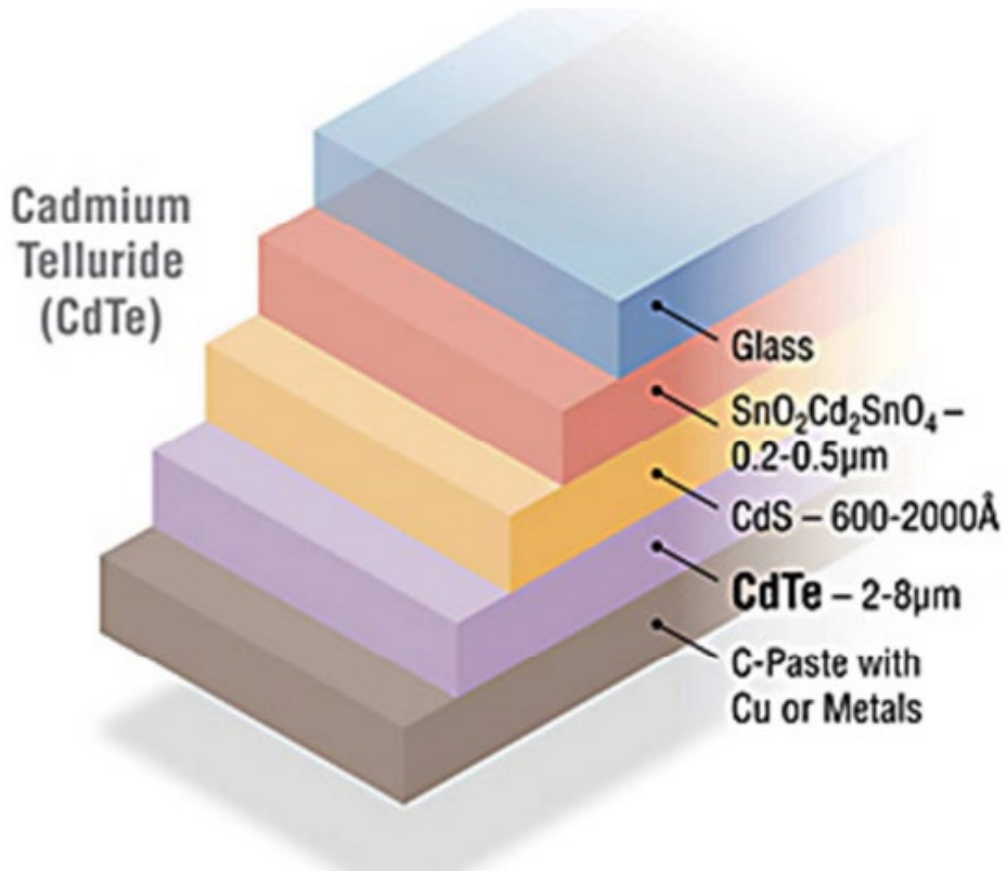


Figure 1. 1: CdTe PV Cell's layered structure [18]

One of the most fatal and toxic chemicals is cadmium whereas combining it with telluride makes it less hazardous than alone in terms of toxicity but it is not toxic-free. If it is handled improperly, it can be fatal and hazardous. In addition, cadmium chloride mixture is used for recrystallization of films of cadmium telluride, a dangerous one. Cadmium telluride safety for long-term and disposal is a big challenge in the commercialization of cadmium telluride PV panels on a large scale. Significant attempts have been made to understand and tackle these problems. United States researchers from the Energy's Brookhaven National Laboratory's department determined that using CdTe PV modules on

a broad scale has no health or environmental risks and that any environmental concerns can be resolved by recycling the modules when they are at the end of life. These modules generate no pollutants and deliver considerable environmental benefits by substituting fossil fuels when in operation. These modules appear more beneficial than any other Cd applications in use now. The European Union and China, on the other hand, take a far more cautious approach to CdTe safety: in the EU, compounds containing cadmium are declared to be severe carcinogens, while the export of Cd products is only allowed by China. Europe is addressing this issue so that Cadmium Telluride usage can be controlled. According to current opinion, rooftop installation in residential and industrial buildings poses no substantial environmental concern using CdTe [19].

1.1.1.2 CIGS – Copper Indium Gallium Selenide Solar Cells

The material that is most problematic and fascinating in solar is CIGS. It was part of the solar thin-film hype cycle that saw Solyndra, Nano-Solar, and MiaSolé almost become household names. A thin-film solar cell that transforms sunlight into energy is a copper indium gallium selenide solar cell (or CIGS cell, also known as a CI(G)S or CIS cell). A small coating of copper, indium, gallium, and selenide is deposited on a glass or plastic foundation, together with front and rear electrodes for current collection. Because the material absorbs sunlight aggressively and has a high absorption coefficient, it requires a thinner covering than other semiconductor materials.

Along with cadmium telluride and amorphous silicon, CIGS is one of three popular thin-film PV technologies. CIGS layers are very flexible like other materials, allowing them to be positioned on flexible substrates. However, because all these approaches rely on high-temperature deposition operations, glass-based cells frequently give the best performance. Nonetheless, the performance falls short of that of modern polysilicon-based panels. Low-temperature CIGS cell deposition advances have eliminated much of this performance disparity. It is well-known for its usage in CIGS solar cells, a thin-film photovoltaic technology [20], [21]. In this role, CIGS has the advantage of being able to be deposited on flexible substrate materials, resulting in highly flexible, lightweight solar

panels. CIGS has become a well-established technology among alternative cell materials due to efficiency advancements.

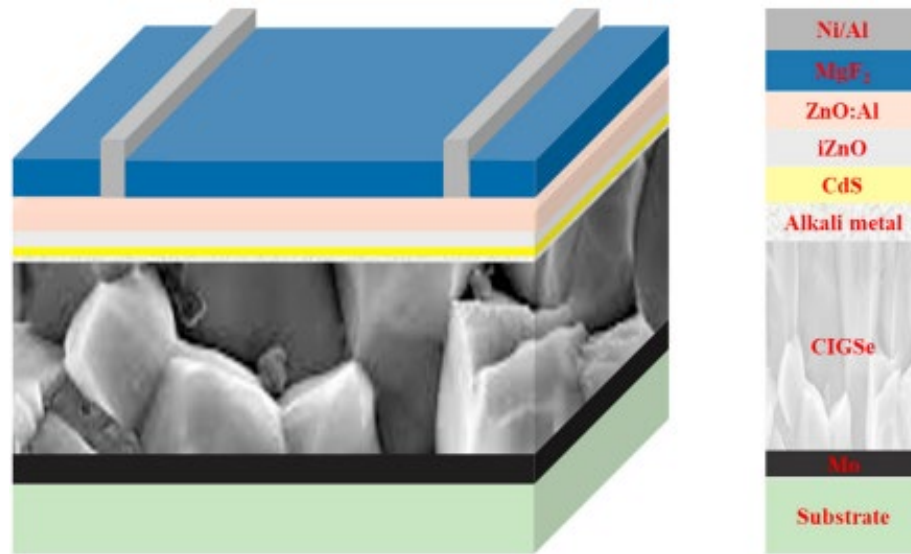


Figure 1. 2: Schematic View of CIGS Solar Cell [20]

1.1.1.3 Quantum Dots Solar Cells

This is a form of solar cell in which quantum dots (QD) are employed as the material of photovoltaic that absorbs light. It intends to replace bulk materials like silicon, CIGS, and CdTe. Bandgaps in QDs may be altered across a full scope of energy levels by simply changing the dot's size. The substance utilized determines the band gap in bulk materials. QDs are intriguing for multi-junction cells because of this feature, which employs a variety of materials to boost efficiency by collecting a wide spectrum of wavelengths from the sun. These are semiconducting particles that have been reduced to a size lower than the Exciton Bohr radius, and the electron energies that may exist within them become finite, like atom energies, due to quantum mechanics considerations. The term "artificial atoms" has been applied to quantum dots. These energy levels may be changed by shifting their size, which determines the bandgap. The dots may be increased in different sizes, letting dots express a wide range of bandgaps without altering the underlying material or manufacturing procedures [22].

Wet chemistry preparations are frequently tuned by adjusting the temperature or duration of synthesis. Quantum dots are intriguing for PV cells due to their ability to regulate the bandgap. Single junction lead sulphide (PbS) CQD implementations have bandgaps that can be turned into the far infrared, which is generally difficult to achieve using traditional approaches. Infrared radiation accounts for half of the solar energy that reaches Earth, with most of it being close infrared. Using a QD, infrared energy is as accessible as any other [23], [24], [25] CQDs are also straightforward to synthesize and produce. They can be easily controlled while floating in a colloidal liquid throughout manufacture, with the most complicated equipment required being a fume hood. CQDs are typically created in small quantities, although they have the potential to be vastly produced. The dots can be manually or mechanically dispersed on a substrate using spin coating. Spray-on or roll-printing processes might be utilized on a wide scale, cutting module construction costs dramatically. Initially, costly molecular beam epitaxy technologies were used, but cheaper manufacturing methods were subsequently established. Wet chemistry (colloidal quantum dots - CQDs) is employed, followed by the processing of the solution. In concentrated solutions of nanoparticles, long hydrocarbon ligands maintain the nanocrystals suspended in the solvent. These solutions are solidified, and the long-chain stabilizing ligands are replaced with short-chain crosslinkers. Chemically altering the surface of a nanocrystal can increase passivation and reduce harmful trap states that might otherwise restrict the performance of the device via recombination of the carrier. This approach has a 7% efficiency [26]. Iodide was initially used as a ligand that does not connect to oxygen in 2014. This keeps stable layers of n-type and p-type, increasing the efficiency of absorption and resulting in up to 8% power conversion efficiency [27].

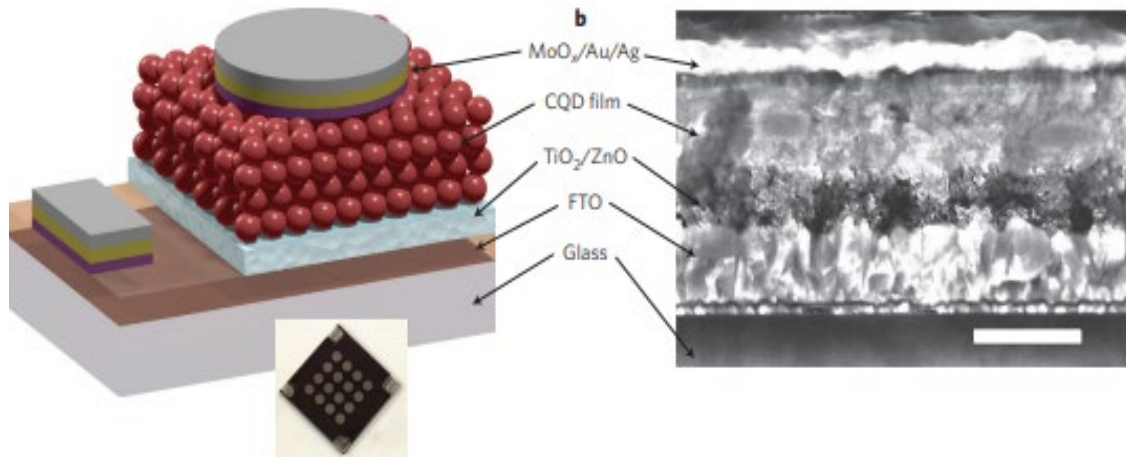


Figure 1. 3: Schematic View of QD Solar Cell [26]

1.1.1.4 DSSC – Dye-Sensitized Solar Cells

Dye-sensitized solar cells are a type of PV cell that transforms any visible light into electrical energy. It is a new type of advanced cell that may be compared to artificial photosynthesis due to the way it duplicates nature's absorption of light energy. DSSC was created in 1991 at École Polytechnique Fédérale de Lausanne (EPFL) in Switzerland by Professor Michael Graetzel and Dr Bridan O'Regan and is mostly known as the Grätzel cell, G-Cell. This technology is game-changing and can be employed to create electrical energy in several lighting situations, both inside and outdoors, allowing users to transform both natural and artificial light into electricity that can be used to electrify many electronic devices. A DSSC is an affordable thin-film solar cell [28], [29]. A photoelectrochemical system is based on the production of a semiconductor by an electrolyte and an illumination-sensitized anode. The DSSC has several enticing functions: it is simple to create using typical roll-printing methods, it is semi-flexible and semitransparent, allowing for a variety of applications not conceivable with glass-based systems, and most of the materials used are affordable. Some expensive components, most notably platinum, and ruthenium, have been difficult to eliminate, and the liquid electrolyte presents a substantial challenge in designing a cell that can be utilized in all-weather situations. Although its PCE is less than the thin-film cells that are best, the ratio of price/performance may be satisfactory to compare with the generation of energy by fossil fuels by achieving grid parity.

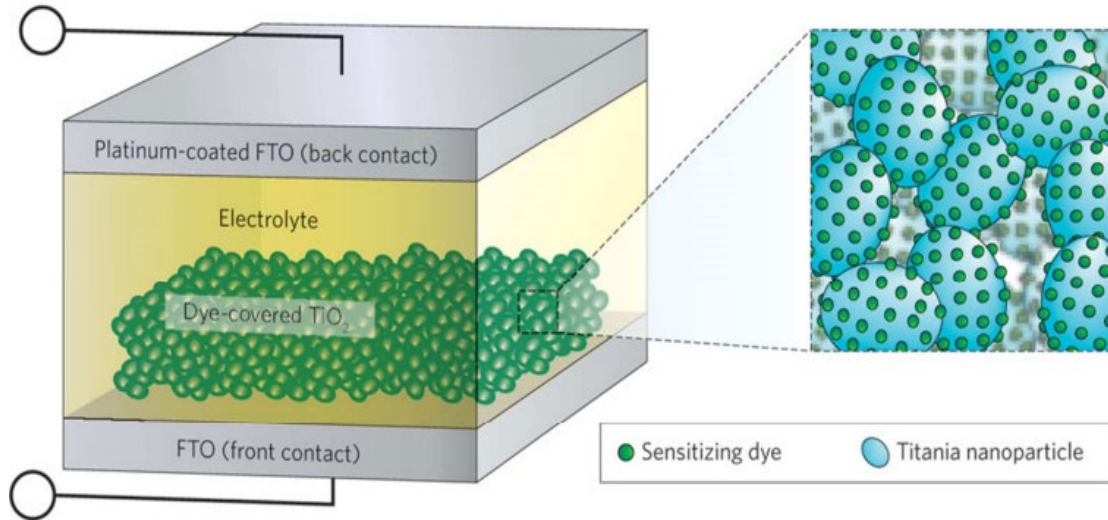


Figure 1. 4: Schematic of DSSC [29]

1.2 Problem Statement

The photovoltaic community has been quite interested in perovskite solar cells throughout the last decade. Thanks to ABX_3 -based perovskite absorbers that have achieved more than 20% efficiency from 2009 till today. Halide perovskite absorbers have superior properties for photovoltaics that cause remarkable improvement in efficiency, like unique tolerance of defects, long length of carrier diffusion, and high optical coefficient of absorption, and, in addition to it can easily be made up by utilizing the processes under low temperature.

There are many challenges in technological advancements of PSCs, although the rapid rise in PCE, prominent of which is the well-known hysteresis in the characteristic curve. This denotes the changes in the sweeps of J-V produced by parameters such as initial biasing, packets of light on the device, scan speed, and scan direction. Before the widespread usage of PSCs, the community of photovoltaics was unaware of the problem of hysteresis. There is little to no hysteresis reported in the literature relating to other solar PVs like silicon, CdTe, and CIGS. It is still under discussion what are the exact reasons for this hysteresis. The plausible explanations that are accepted universally, as the causes of hysteresis, are ion migration, interface capacitance, and interface trap states. J-V measurements which are considered to evaluate the performance of other solar

technologies are not capable of giving an accurate and consistent characterization of the metal halide solar cell technology due to its hysteretic nature. As previously indicated, the results are greatly reliant on the conditions of the voltage scan. The efficiencies obtained from the measurements of J-V that have been published may have underestimated or inflated the performance of perovskite solar cells. Hence, addressing the optimal power point extraction of perovskite-based cells under the hysteresis effect, as well as the impacts of scan direction and initial bias on perovskite solar cell hysteresis, is crucial.

1.3 National Needs

Due to the country's enormous population and limited industrialization, energy sources are limited which results in crucial impacts on the environment, especially in rural areas. Alternative energies resource is needed in today's era. Such energies have a high impact on the economy of a country. All human activities involving education, healthcare, agriculture, and work require energy.

In Pakistan, electricity generation is through fossil fuels (64%), hydropower (27%), nuclear (5%), and solar (1.16%). Only 4% of electricity is from renewable sources. The difference between the supply (~21,191MW) and demand (~27,900MW) of electricity in the country is ~6709MW, causing extended power outages.

Pakistan's topography and climate are suitable for renewable energy like solar power. Solar energy might quickly address Pakistan's electricity issues and various environmental problems like pollution and greenhouse emissions.

Electricity generation in Pakistan is mostly dependent on fossil fuels, whose prices exponentially rise day by day. This price increase poses complex issues for the power industry and makes it difficult for consumers to fulfill their electricity needs. Renewable energy such as solar energy is a cost-effective solution to the previous problem. Silicon-based solar energy is expensive and inadapted for most customers. Therefore, efforts are being made worldwide to create and enhance third-generation solar cells such as perovskite-based solar cells due to the simplicity of manufacturing, and cost reduction.

1.4 Research Motivation

Natural gas, oil, and coal provide energy to most of the world's population. Finite resources dependent on nonrenewable fossil fuels will deplete that will result in ecologically harmful and expensive recovery. The major cause of air pollution is the generation of electricity from fossil fuels. Electricity in the world is mostly produced by nonrenewable power facilities that use fossil fuels (natural gas, oil, and coal). The usage of such resources for electricity production is damaging the environment and has a noteworthy impact, inflicting harm to land, water, and air. To reduce the impacts of pollution and climate change, the best way to generate electricity is from sources of renewables. No carbon dioxide emissions happen by the usage of renewables for generating electricity which ultimately reduces the impact on climate change. The sources of this energy are natural sources that can be easily used without reducing the resources on the planet. Renewables are available in vast quantities over the world and have no or little impact on the environment. Wind, thermal, and solar are some examples of renewables. Natural gas, coal, and oil are not part of renewables because their availability is limited, because economically they do not remain viable sources. These are obtained by natural processes, slow to replace these sources in comparison with their consumption, hence these sources will eventually run out. Sources of renewables are replenished constantly, and these sources will never be depleted. Energy from renewable sources is mostly produced by the sun. Light from solar may directly fall on structures of heat and light, electricity is produced and can be used to meet energy demands like cooling, heating, and many other industrial and commercial purposes. Sun is an infinite source of energy and comparatively distributes a huge amount of energy in an hour as the quantity of energy used in one year. 9.5×10^{25} W of the energy is emitted by the sun, approximately. This solar energy is still undiscovered in regions that are rich in photons. The efficient capture and conversion of photons into energy is still a technological challenge. Today, crystalline silicon on wafers dominates solar technology (ribbon, monocrystalline, and polycrystalline silicon). Over the last three decades, the fundamental motive for PV cell research and development has been to minimize the expenditure of power generated from PV. The price of a PV module is mostly determined by its lifetime of operation, the per unit area cost of manufacturing, and PCE. As a result, the efficiency improvement of silicon PV modules using less costly grades is a

hot topic on the research side. Despite continual advances in bulk crystalline technology in the past few years, numerous photovoltaic approaches have been established concurrently. Thin film technologies with fewer materials and that can be created on less costly, thin substrates using high fabrication procedures have been actively investigated and developed to reduce manufacturing costs. Modeling photovoltaic systems currently involves a variety of techniques, challenges, and approaches. Photovoltaic cells are critical for the following reasons:

- The primary source of renewable energy is Solar which is abundant worldwide.
- Photovoltaic panels have no moving components, run quietly, and produce no pollution.
- Solar technology is very modular and readily scalable to supply the necessary electricity for various loads.

The disadvantages of this energy are that it has an irregular supply of energy because at night, in cloudy conditions, or fog, the sun does not shine, and electricity from solar costs more than that of power from conventional sources. Perovskite cells are a good emerging technology because they can be placed on different substrates like rigid, flexible, or insulator metal, etc., and can be fabricated by different techniques such as PVD, CVD, ECD, hybrid, plasma-based, etc. They have an advantage over crystalline silicon because of the dependence on materials that are highly absorbent and make the photoactive layers much thinner (c-Si). As a result, they may be manufactured utilizing low-cost, high-volume production methods. The thickness of perovskite solar cells is much less than silicon cells. These types of devices that are thin need fewer materials. These devices may be mounted on less costly substrates like foil or glass easily. Highly efficient devices may be constructed across the world if the correct understanding and knowledge of deposition processes are known, like demonstrations of other cells. These cells (TFSC) will soon contribute significantly to global energy consumption.

1.5 Research Objectives

Numerous investigations have been conducted on solar cells like silicon, organic,

and thin film. However, in research simulations, progress has been made by PSCs. For understanding the PSCs, the numerical analysis technique may help thoroughly which is a vital strategy for increasing the efficiency of PSCs. The objectives of this research thesis are:

- To understand the modeling and mechanism of operation of PSCs.
- To study and analyze the impacts of scan rate, and direction on the J-V hysteresis and ultimately, on the performance of PSC.
- To develop a maximum power point tracking (MPPT) algorithm that extracts the maximum power, by predicting the maximum power point, from a perovskite solar cell under the hysteresis effect.

1.6 Applications of the Research

Maximum power extraction from PSC and its modeling study can have many applications, including:

1. Generation of renewable energy: A cost-effective and sustainable energy can be provided by PSCs in terms of renewable energy. By improving the efficiency, stability, and reliability of PSCs can make them a valuable source to produce energy on a large scale.
2. Portable devices: Portable devices can be powered by the energy produced by PSCs such as laptops, mobiles, and wearables.
3. Light-up Homes: Power generated by PSCs can be utilized to light up homes and use electricity to run the electronics. Green and pollutant-free energy can be beneficial for the environment too.
4. Smart integration: PSCs can be integrated into buildings, grounds, and other places to produce clean and green energy for smart cities. It can be a more practical source of energy generation, especially in urban areas due to its improved efficiency, lower cost, and rate of return.

5. Storage: Batteries, supercapacitors, and other storage devices can be integrated with the PSCs to be a source of reliable, interruption-free, and sustainable power. Maximum power extraction and modeling of PSCs and related research can help in the improvement and optimization of PSCs' performance in energy generation and storage systems, enhancing their stability and efficiency.

The research in modeling and maximum power extraction from PSCs has a vast range of potential applications, from the generation of renewable energy applications for space technology, and the development of sustainable solutions of energy can be significantly contributed by the research area in PSCs.

1.7 Thesis Organization

In Chapter 1, a complete introduction about the solar cell history and the solar cell evolution is also mentioned and discussed in detail. The research motivation is also elaborated. Furthermore, research objectives and applications of the topic are also mentioned in it.

Chapter 2 discusses the literature review relating to solar cells, specifically Perovskite Solar Cells (PSCs). The PSC's background, development, and related technologies are also mentioned. Hysteresis in PSCs and the influential factors are elaborated too. After that different MPPT techniques, developed in the literature, and used for the solar cell industry are discussed in detail too. This chapter also discusses the related research already done in the past and highlights the limitations and bottlenecks in them. Based on limitations, the problem statement is elaborated on in this section too.

The modeling and implementation of PSC and the developed novel MPPT algorithm are discussed in Chapter 3, and Chapter 4, respectively, in detail with the mathematical modeling completely. The results obtained by the modeling, implementation in MATLAB, and extraction of maximum power from three layered PSC are discussed in Chapter 5. The impact of scan rate on the J-V hysteresis is analyzed in detail. Extraction of MPP under the hysteresis and under the minimum hysteresis both are highlighted and

compared. In the end, a comparison between the developed MPPT and already defined MPPTs is also elaborated in this chapter.

The last chapter concludes the complete work and future recommendations are also mentioned in this final section.

CHAPTER 2: FUNDAMENTALS AND LITERATURE REVIEW

Green, clean, and limitless energy produced by solar cells, converted to electricity makes them one of the most well-liked and adopted areas in research and development. Our reliance on traditional fossil fuel energy, which emits considerable amounts of greenhouse gas emissions, has been highlighted as a contributor to climate change, and this technology of green energy has been proposed as a potential remedy. The crystalline silicon panels, which provide a high efficiency of 25.6% and exceptional stability, currently dominate the solar or photovoltaic cell market. However, due to the energy-intensive crystal formation and vapor deposition procedures needed to produce ultra-high-purity silicon, these silicon solar cells are quite expensive. Even with government assistance, consumers in the current market are hesitant to embrace this technology to produce electricity. For applications to improve, solar cell production costs must be reduced. New types of Solar PV cells are,

- PSCs – Perovskite solar cells
- OPVs – Organic photovoltaics
- DSSCs – Dye-sensitized solar cells

During the last two decades, the DSSCs and OPVs have progressed significantly. The highest PCE that DSSCs or OPVs can obtain is still low, less than 60% of what cutting-edge silicon panels can accomplish, and is therefore not even close to being a practical consideration. Thankfully, the positive outcomes of PSCs give the profession fresh hope. Even though PSCs have advanced significantly in less than a decade, their maximum PCE has surpassed 23% and is now on par with silicon solar cells. PSCs are currently attracting attention on a global scale, with a strong desire to improve PCE and streamline the production process to reduce costs. Because of its weak resistance to degradation by oxygen, moisture, UV radiation, and heat, PSCs may not be commercially viable. Several experiments have been conducted to increase the resilience of the structure of hybrid perovskite in real-world settings. The most significant hurdle to PSC applications is their dependability. Many means of further stabilizing the cell crystals have been tried to overcome this issue, including:

- The Utilization of Buffer Layers
- Cell Encapsulation
- Perovskite Composition Optimization
- Interface Optimization

Despite these efforts, PSCs are still a long way from obtaining the same level of long-term environmental stability as solar cells made of silicon. PSCs' low stability may be noticed in the structural vulnerability to the circumstances related to applications and in the challenges related to obtaining the performance of solar cell and reliability assessments owing to I-V hysteresis too. Various morphologies of I-V curves were found during the characterization of PSCs, which varied with scan direction, range, and rate. I-V hysteresis is responsible for making it difficult to recreate and explain PSCs in a reproducible way. It is relatively restricted to understand hysteresis at this moment, and its precise explanation is uncertain. However, this is a significant issue that must be addressed, as the efficiency and dependability of PSCs must be appropriately evaluated before moving on to the next application step. Removing hysteresis is a useful strategy for improving PSC solar performance. This might suggest a link between the crucial figures of efficiency, stability, and hysteresis. Charge extraction, for example, is enhanced, nonradiative recombination is reduced, and ion migration is reduced, all of which help to reduce hysteresis while enhancing efficiency. As a result, successfully removing hysteresis is crucial for obtaining correct efficiency and boosting PSCs' total photovoltaic performance [30], [31].

2.1 Perovskite Solar Cell's Background

A paper on a perovskite solar cell with a 10% efficiency was published in Nature in 2012. A great deal of attention should be given to low manufacturing costs, promising commercialization, and excellent performance that has been generated by PSCs, since then [32]. The following are five layers that make up a PSC.

- Perovskite layer
- ETL – Electron transport layer
- HTL – Hole transport layer

- Anode layer (FTO/ITO)
- Metal-based cathode layer.

PSC is composed of these five layers. The architecture of PSC with a planar shape is depicted in Figure 2.1.

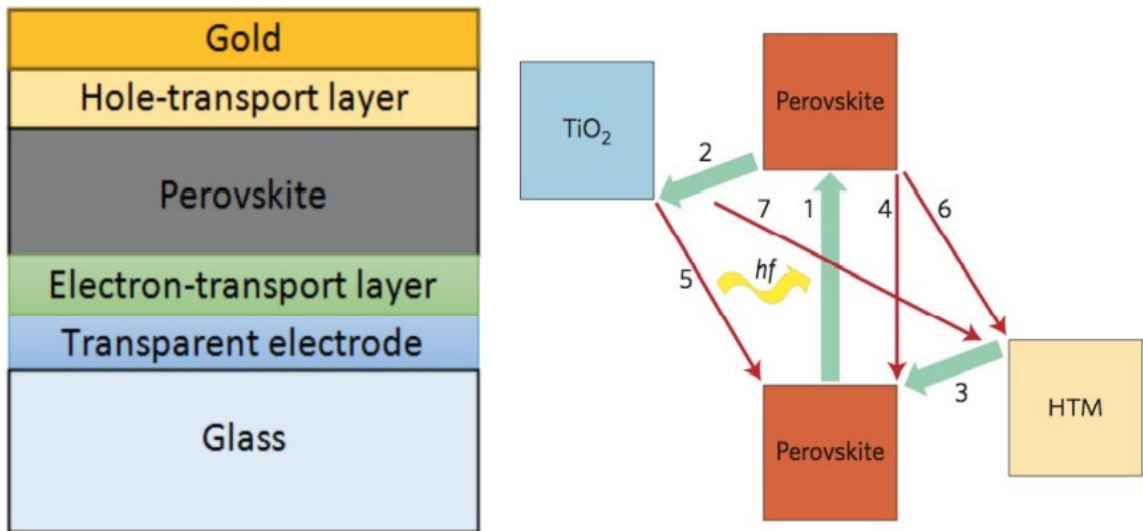


Figure 2. 1: Planar shape of Perovskite Solar Cell [33]

The perovskite layer acts as the absorber of light when the excitation of photons takes place. The holes and electrons are transported to the transport layers and separated, respectively. The ambipolar nature of perovskite is the reason for the fast mobility of holes and electrons in perovskite. ETL's duties include blocking holes and extracting and transporting electrons. The holes are extracted and moved by the HTL layer. It also stops the electrons. High mobility for both holes and electrons and the necessary offsets between ETL, HTL, and perovskite are required [33], [34], [35]. Figure 2.1 depicts the primary charge transport channels in PSCs. Energy conversion processes are reflected by the green arrows like electron transport from the perovskite layer to the ETL, hole transport from perovskite to HTL and photon excitation. Unintended processes in perovskite solar cells, such as charge carrier recombination, reverse electron flow from the ETL, and hole flow from the HTL to the perovskite are illustrated by red arrows and result in energy loss [36].

2.1.1 Materials of Perovskite

Perovskite material, also known as ABX_3 , has a crystal structure comparable to calcium titanate ($CaTiO_3$). As shown in Figure 2.2, organic ammonium is depicted by A, such as $CH_3-NH_3^+$, metal cation is shown by B e.g., Pb^{2+} , and halide anion is shown by X e.g., Cl, Br, I [37].

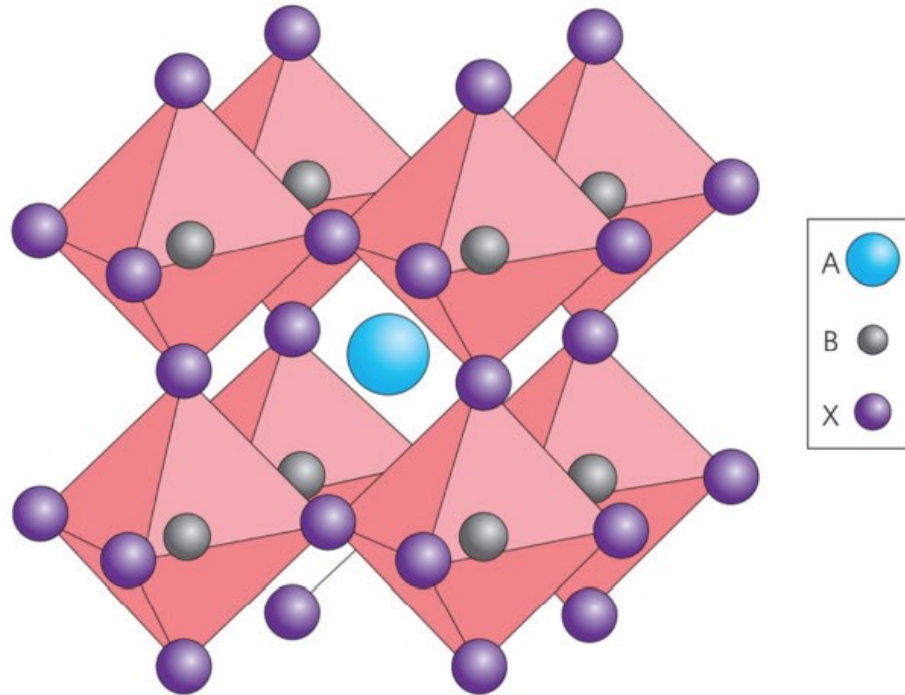


Figure 2. 2: ABX_3 Structure of PSC [37]

The perovskite's crystallographic structure can be determined by using the 't' tolerance factor and 'u' octahedral factor. Equation 2.1 shows the expression for "t".

$$t = \frac{r_A + r_X}{\sqrt{2} * (r_B + r_X)} \quad (2.1)$$

Here, r_X is the ionic radius of X, r_A denotes the radius of A, and the ionic radius of B is represented by r_B .

According to research, the tolerance factor of most perovskite materials lies between 0.75 to 1 [38]. Just analyzing the factor of tolerance, it is inadequate to forecast the perovskite's crystalline structure. 'u' the factor of octahedral is used as the extra signal to anticipate the structure of perovskite's evolution. "u" is also explained using equation 2.2.

$$u = \frac{r_B}{r_X} \quad (2.2)$$

The conditions for production of structure of ABX_3 are $0.442 < u < 0.895$ and $0.813 < t < 1.107$ [39]. Figure 2.3 shows the structural map for ABX_3 when t and u are considered.

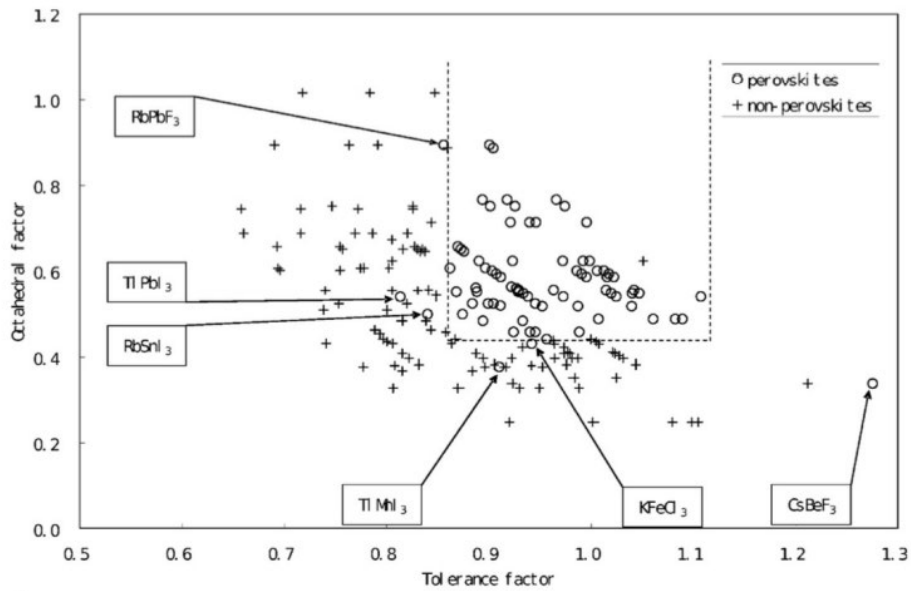


Figure 2. 3: Map of the structure of ABX_3 considering “t” and “u” [39]

Perovskite materials are distinguishable from other materials by their long carrier life, sufficient energy of bandgap (1.55eV), high extinction coefficient, and length of diffusion [40], [41], [42], [43], [44], [45], [46], [47]. Because of its advantageous properties, light absorbers like perovskites are widely used in PV cell systems. There are some limitations in this technology which can cause degradation in performance, as well

as toxicity issues due to Pb^{2+} ions on the human body and environment while using disposal and fabrication processes [40].

2.1.2 *Development of Perovskite Solar Cell*

In 2006, the first solar cell based on perovskite was demonstrated by Miyasaka et al. They created a solar cell with a 2.2% efficiency using the chemical $CH_3NH_3PbBr_3$ [41]. Instead of bromine, iodine was used by Miyasaka et. al, in 2009, resulting in a 3.8% of efficiency [42]. A surface treatment of TiO_2 , in 2011, was utilized by Park and colleagues to enhance efficiency to 6.5%. The quantum dot (QD) PV cells absorb lighter than dye-sensitized PV cells. The QD's stability is poor, however, since QDs degrade in the solution of electrolyte [43]. Liquid electrolytes were replaced with solid-state chemical compounds to avoid the effects of electrolytes by Park et.al. Spiro-MeOTAD-based HTL material was used with mesoscopic TiO_2 as ETL material so that the device stability could be improved. 9.7% of efficiency was obtained by Park et.al in 2012 [44]. PSCs with Spiro-MeOTAD as HTL and Al_2O_3 scaffolds were reported by Snaith and colleagues in the same year. An efficiency of 10.9% was reported for this device. It was demonstrated in this research that using mixed-halide ($CH_3NH_3PbI_{3-x}Cl_x$) can result in improved performance owing to improved charge transport capacities. They also demonstrated bipolar electron and hole charge carrier transport in perovskites [45]. A 12.3% efficiency, using a nano-porous TiO_2 framework infiltrated by mixed-halide perovskite, was reported by Seok, Grätzel, and colleagues in 2013 [46]. A simultaneous efficiency of more than 15%, using TiO_2 scaffolding and iodide deposition, was achieved by Burschka et.al [47]. A planar structure was employed by Snaith, instead of scaffolding, and the same power conversion efficiency was achieved by Burschka et al. [48]. 16.2% and 17.9% efficiencies, in early 2014, were reported using $CH_3NH_3PbI_{3-x}Cl_x$ and a poly-triarylamine HTM by Seok et. al.[49], [50]. In 2016, a PSC was demonstrated, with a 21.1% efficiency, using a triple cation combination (Cs/MA/FA) by Saliba in [51] that depicted excellent stability and repeatability. An approach was proposed by Seok and colleagues in 2017 that removed the defects in the perovskite layer by utilizing an intramolecular swapping mechanism, a very useful technique in reducing the concentration of defects. By doing this, more than 22% efficiency was achieved [52].

2.2 Perovskite Solar Cells and Hysteresis

For evaluating the performance of PSC, the current density–voltage curve [53] is the essential feature. Typically, under $100\text{mW}/\text{cm}^2$ of illumination, the testing and evaluation of the J-V plot is processed. This is now used to assess photovoltaic features i.e., fill factor (FF), power conversion efficiency (PCE), short-circuit current (J_{sc}), and open-circuit voltage (V_{oc}). There is always a hysteresis between the scan directions like forward and backward during the measurement of PSC's current density – voltage characteristics, which means that the reverse and forward scans cannot overlap. Most of the hysteresis reported in PSCs are normal hysteresis, indicating that reverse scanning (RS) outperforms forward scanning (FS). However, reversal hysteresis has been seen under certain situations when the RS result outperforms the FS [54], [55], [56]. This hysteresis is dependent on the scan rate, leading to wrongly reporting the performance of PSCs i.e., underestimating or overestimating the PCE of PSCs [57]. The output of PSC is inconsistent, and hysteresis is the main major factor of it [58], [59], [60].

PV performance and its statistics become doubtful due to this hysteresis problem, making estimating the real performance of PSC problematic[57]. The development of PSCs is therefore restricted due to this issue which majorly makes it unstable for the usage of it commercially. Despite various efforts to know the sources of hysteresis and the steps to eliminate it, this phenomenon remains controversial, and an effective universal approach has yet to be discovered.

2.3 Influential Factors Impacting Hysteresis in Perovskite Solar Cells

PSC's material, architecture, test conditions, and several other factors were discovered to impact hysteresis behavior in PSCs during the researchers' investigation. In other words, these variables might be used to modify hysteresis in PSCs.

2.3.1 *Cell Architecture*

Hysteresis content in PSCs differs depending on cell design. When TiO_2 is used as the ETL material, less hysteresis is exhibited in mesoporous PSCs than in planar heterojunction PSCs. According to the literature and the researchers, more effective

electron transmission and separation are noticed by increasing the contact area between the perovskite materials and mp-TiO₂. In SnO₂-based PSCs, the importance of the mp – ETL in reducing hysteresis is proven. The cell design must be carefully chosen to eliminate or decrease hysteresis [61].

2.3.2 *Perovskite Material*

PSC is completely made up of multiple materials that influence hysteresis in various ways. PSCs, for example, contain light-absorbing perovskite material, which can influence hysteretic behavior. APbX₃ perovskites appear to generate less hysteresis in PSCs than MAPbX₃ due to the photoactive material, FA, and MA at the A site. The type of hysteresis varies as well as the degree of hysteresis. MA_{0.27}FA_{0.73}PbBr_{0.51}I_{2.5}-based PSCs have reversed hysteresis (10 and 100 mV.s⁻¹ scan speeds) and J-V curves with overlapping RS and FS at one point (1000 and 10 000 mV.s⁻¹ scan rates). Furthermore, the crystal size of a certain perovskite influences its hysteresis. By employing the proper composition and perovskite crystal size, PSC hysteresis may be eliminated.

Because the kind of contact can have a substantial influence on the reaction to the accumulation and separation of charge at the interface, the interfaces of the P/ETL, P/HTL, and the HTL/electrode are essential components affecting hysteresis. The importance of energy alignment between extraction layers and perovskite is pointed out by the role of interfaces in PSC's hysteretic behavior [62], [63], [64], [65].

2.3.3 *Impact of Different Testing Conditions*

When evaluating PSC's hysteresis, external test conditions should be considered in addition to the impacts of a few internal components, because the hysteresis is only determined by these conditions but, in some cases, the type of hysteresis is also defined. The hysteresis behavior of PSCs, according to the researchers, varies with the scan rate and intensity of illumination. Slower scan rates increase hysteresis by 0.3-0.011Vs⁻¹ in planar heterojunction PSCs. Traditional PSCs based on mp-TiO₂, exhibit reverse tendency, with hysteresis becoming more visible when the scan rates are high but when the scan rates are slow, it is reduced. Furthermore, starting scan bias influences hysteresis behavior too.

When a scan with a larger negative voltage bias begins, the photovoltaic efficiency seems to fall more dramatically, resulting in significant hysteresis. In a limited scan range, hysteresis diminishes with a slow sweep rate; though, when the scan range is large, this trend changes. Scanning rates and pre-poling bias both influence the hysteresis type. Inverted hysteresis is related to higher scan rates and a negative pre-poling bias, and the other way around. The settling time of voltage influences hysteresis too. In PSCs that are based on mp-TiO₂, it is observed that the hysteresis becomes less after a settling time of 3000ms than after a 200ms settling time, whereas for TiO₂-based planar heterojunction PSCs, its opposite is valid. It is suggested from these outcomes that the intensity of current in PSCs, the shape and structure of solar cells, as well as the voltage settling time, all are significant. Furthermore, the scan period is also responsible for varying the hysteresis in the PSC J-V curve. The hysteresis origin can be further complicated by the electron transport, cell structure, electric field, and other factors that can be responsible for a shift in hysteresis with external test conditions [64], [65], [66], [67].

2.4 Possible Origins of Hysteresis in Perovskite Solar Cells

The studies and research conducted by many researchers in the field of PSCs were evaluated and discovered that materials utilized in the PSC, cell test conditions, cell layout, and several other aspects, have impacted the hysteresis behavior in PSCs. In other words, these variables might be used to modify hysteresis in PSCs.

2.4.1 *Ferroelectric Effect*

Ferroelectric polarization is found in inorganic, organic hybrid perovskites (MAPbX₃, X = Cl, I, Br) in DSSCs which is supported by Fourier transform and Raman spectra, alongside force microscopy's piezo response. The presence of an MA⁺ dipole has been linked to this characteristic that shifts the symmetry of the structure of perovskite between I4/mcm to I4cm. Hysteresis in PSCs might be caused by the ferroelectric activity of hybrid perovskites.

The ferroelectric effect and the negative poling effect can be used to polarize PSCs with the structure as p-i-n. the breath of the depletion area and the built-in field may be

reduced by the opposite direction of the polarization field which reduces the performance of the cell and limits the separation of charges. In contrast, the performance of PV cells can be increased by poling positively which simplifies the extraction of charges and collection too. Hence, the RS in the case of positive bias and RS in the case of negative bias that produces different current-voltage curves can be understood easily. The effect of ferroelectric may help to explain the reason for hysteresis's sensitivity to scan rate, scan starting point, and perovskite layer thickness. The effect of ferroelectric may also explain the reason for the greater hysteresis level in planar PSCs than that of mesoporous PSCs based on TiO_2 to some extent. Few hysteretic occurrences can be characterized rationally in terms of the ferroelectric effect; however, the only source and reason for hysteresis in PSCs does not confirm this hypothesis; there must be other causes too that need to be addressed and investigated [68].

2.4.2 *Unbalance Charge Carrier Transport*

Because halide perovskites are ambipolar, the transport of holes and electrons may take place separately; nevertheless, the difference in the lengths of diffusion for electrons and holes causes the imbalance. Hole separation is more efficient in perovskite than electron separation. To increase the extraction of electrons from the layer of perovskite, PSCs use ETL regularly. This is done to balance the poor transport of electrons in perovskites. Regular mp- TiO_2 -based PSCs exhibit less hysteresis than n-i-p and meso-superstructure PSCs because electrons can be separated by mp- TiO_2 more efficiently than TiO_2 and Al_2O_3 . However, TiO_2 ETL's mobility of electrons ($104 \text{ cm}^2 \text{ V}^{-1} \text{ s}^{-1}$) is slower than the mobility of holes ($103 \text{ cm}^2 \text{ V}^{-1} \text{ s}^{-1}$) of regularly used materials in HTL, including poly[bis(4-phenyl) (2,4,6-trimethylphenyl amine)] (PTAA) and spiro-OMeTAD. As a result, PSCs suffer from unequal charge transfer, which may be mitigated by increasing electron mobility in ETL materials. Because of the imbalance in electron-hole transport, certain electrons result in capacitance. This capacitance responds variably depending on scan orientation and speed, resulting in significant hysteresis. Hysteresis in devices can be decreased by improving the charge transport mechanism due to the unequal electron and hole transport in perovskites [61].

2.4.3 *Migration of Ion Vacancy*

The mobility of ions is common in the structures of perovskite and the presence of interstitials causes the movement of ions or vacancy of ions. Photothermal-induced resonance microscopy was used to find ion electromigration, indicating that the migration of ions is triggered by the electric field that photovoltage creates. Migration of ions can affect hysteretic photocurrent and this hypothesis is supported by this article. The theory of migration of ions states that under forward/reverse bias circumstances, ions and their associated vacancies travel in different directions to the relevant interfaces. Furthermore, the accumulation of positive ions at the interface causes doping of n-type by drawing electrons out of the film to preserve charge neutrality. Similarly, p-type doping is caused by the accumulation of similar negative charges and vacancies on the reverse side. The most important question is establishing which kind of ion transport causes hysteresis in the J-V curve of PSCs. Energy activation needs to be employed can be the one approach in the resolution of this query, and the ion and vacancy migration can be evaluated by this. If the energy of activation for vacancy migration or ions corresponds to the energy of activation for hysteresis, then this movement should be the theoretical factor determining the J-V hysteresis [54].

2.4.4 *Trap Assisted Charge Recombination*

Holes and electrons are trapped, resulting in recombination, as opposed to ion or vacancy migration, which causes charge accumulation. One of the causes of hysteresis has been proposed as the process of charge trapping and de-trapping. At the interfaces, trapping and de-trapping happens between the transport layers, in addition to at the grain boundary of perovskite, where many defects act as trapping sites. Under advanced bias working settings, defects will trap electrons and holes, and the charges that are trapped will be freed under the conditions of short-circuit when the layers of transport separate them while waiting for the faults to be replaced. The time-consuming of trapping the charge and de-trapping technique might add to photocurrent and voltage delays. Several investigations have also shown that by passivating or decreasing the traps on the boundaries or surface of perovskite, hysteresis in PSCs may be reduced. Tuning the annealing duration and

temperature of the perovskite layer, for example, has been used to modify trap densities and hence change the hysteresis [54].

2.4.5 *Challenges to These Possible Origins*

When measuring the timeframe of hysteresis from milliseconds to seconds, these logical reasonings may encounter issues and become contested in some circumstances. Given the speed of the process (1 minute), these occurrences are unlikely to be the source of the hysteresis. When investigated over time, several investigations have cast doubt on the property of ferroelectric and migration of ions as causes of PSC's hysteresis. A growing number of studies in recent years have demonstrated that hysteresis is the consequence of the combined impacts of several factors, rather than an autonomous process directed by a single component. When employing migration of ions to explain the saturation properties of J-V curves, charge recombination, for example, produced by imperfections on the surface, should not be neglected. S-shaped I-V curves can only be produced by the buildup of ions within cells and recombination on the surface. The phenomenon cannot be properly described without the use of such approaches. As a result, it is acceptable to assume that the hysteretic occurrences are the outcome of several complex processes. Because the ionic and charge processes are so inextricably linked, both should be to blame for the dynamic process of hysteresis. Regardless, more research is needed to establish the source of hysteresis [54].

2.5 **Performance Parameters of Solar Cells**

The main parameters for any solar cell that are important to consider are,

- Current Density – Voltage Curve
- Maximum Power
- Open Circuit Voltage
- Fill Factor
- Short Circuit Current
- Output Current

- Quantum Efficiency

These parameters are briefly discussed below and studied from [68][69].

2.5.1 V_{OC} – Open Circuit Voltage

When there is no current noted in the PV cell, the voltage generated is known as open circuit voltage. Equation 2.3 determines the V_{oc} which is the maximum achievable voltage from a PV cell.

$$V_{OC} = \left(\frac{n * k * T}{q} \right) * \ln \left(\frac{I_L}{I_0} + 1 \right) \quad (2.3)$$

In the forward bias quadrant, it is the maximum voltage at the load of the circuit. V_{oc} is depicted in Figure 2.8.

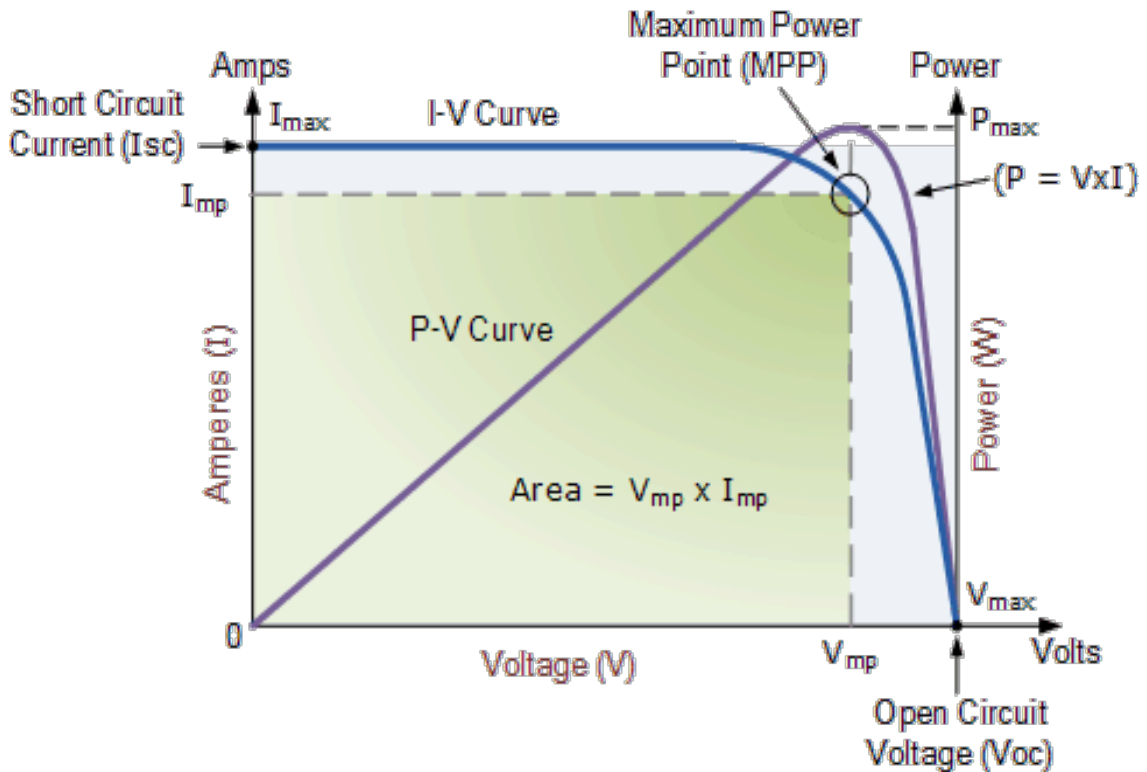


Figure 2. 4: PV and IV Curves with Labels [68][69]

2.5.2 I_{SC} – Short Circuit Current

It is the maximum current that can be drawn from the PV cell. When the circuit is short-circuited, this current can be drawn. I_{SC} is caused by the accumulation and creation of carriers. I_{SC} is largely governed by the area, optical properties, collecting probability, spectrum, and incident photon count of the solar cell. Surface passivation and the length of diffusion are critical variables of material. I_{SC} is shown in Figure 2.8.

2.5.3 FF – Fill Factor

A solar cell's maximum power output is defined by FF , together with I_{sc} and V_{oc} . It is the ratio of maximum power to the product of I_{sc} and V_{oc} . The curve factor, an alternative name of FF , is a graphical representation of the PV cell's "squareness" as well as the size of the largest rectangle that fits inside the J-V curve. '1' is its optimum value; the maximum value for silicon solar cells is 0.88. Its mathematical formula is as follows:

$$FF = \frac{P_{max}}{V_{oc} * I_{sc}} \quad (2.4)$$

2.5.4 Output Current

In equation 2.5, the mathematical expression for current is indicated.

Output Current = Diode Dark Current – Light – Induced Current

$$I = I_0 * \left[\exp\left(\frac{q * V}{k * T}\right) - 1 \right] - I_L \quad (2.5)$$

In this equation, I_0 stands for the current of saturation, also known as diffusion current or leakage current, the charge of an electron is denoted by 'q', and the constant of Boltzmann is denoted by 'k'. The structure of the solar cell influences both I_L and I_0 .

2.5.5 *Maximum Power*

The mathematical relation of power at the output is expressed as follows:

$$P_{out} = V_{out} * I_{out} \quad (2.6)$$

When the circuit is closed or open, no power is produced, and the output power (P) is zero. Maximum power will be offered by the device for maximum I and V values (Pmax).

$$P_{max} = V_{max} * I_{max} \quad (2.7)$$

2.5.6 *Quantum Efficiency*

When light strikes a solar cell, it generates many charge carriers. The ratio of the number of charge carriers captured by a photovoltaic cell to the number of photons of a certain energy shining on the solar cell is referred to as "quantum efficiency." As a result, wavelength or energy is used to determine QE. The efficiency of a PV cell is stated as

$$\eta = \frac{P_{max}}{P_{in}} = \frac{V_{max} * I_{max}}{\text{Incident solar radiation} * \text{Area of Solar Cell}} \quad (2.8)$$

where I_{max} and V_{max} are the maximum current and voltage, respectively. PV cell conversion efficiency is another term for the fraction of solar energy that shines on the device of PV and electrical energy is obtained by the conversion of it.

2.5.7 *J-V Plot – Current Density-Voltage Characteristics*

When lighted, a PV cell operates like a large diode, having the equivalent curve as a diode in forward bias. When lighting, the J-V curve moves by the amount of electricity produced. The change occurs when the light increases. Under these two distinct conditions, the plot of J-V is a superposition of curves. The dark current in the diode increases when the cell is lighting, by diode aw, as quantitatively denoted in equation 2.9.

$$I = I_0 * \left[\exp\left(\frac{q * V}{k * T}\right) - 1 \right] \quad (2.9)$$

Figure 2.8 shows the J-V curve. It sets the minimal amount of current due to minority carriers in the dark. The PV process begins by illuminating the cell on a horizontal plane with a 1-Sun, Air Mass 1.5 global spectrum, and current is generated because the incoming photons produce charge carriers.

2.6 Maximum Power Point Tracking (MPPT) Techniques

Tracking a solar array's maximum power point (MPP) is a key milestone in the development of solar photovoltaics. Many MPPT techniques have been developed, with different strategies available and with certain limitations. It is difficult to decide which MPPT technique will be useful due to several options available. The complexity of the system, digital or analog implementation, number of sensors needed, convergence speed, cost efficiency, and tracking capabilities all vary. The selection of MPPT depends on the application. As a result, this section focuses on the MPPT algorithms that are popular today.

2.6.1 *Perturb and Observe (P&O)*

This algorithm operates by periodically decreasing or increasing the current or terminal voltage of the array, and then comparing the PV output power to that of the previous sample point, as shown in figure 2.9 below. If the operating voltage of the PV array changes and the power increases ($dP/dV \text{ PV} > 0$), the control system shifts the PV array operating point in the other direction [69]. The algorithm continues to operate in the same manner at each perturbation point [70].

The primary benefit of this method is its simplicity. Furthermore, it is not required that it should have prior knowledge of the attributes of PV panels. This method often operates effectively if the sun's irradiation does not shift too frequently. In a stable condition, the point of operation oscillates around the voltage at MPP and generally changes substantially. For the system to be settled before the next disruption, the frequency of perturbation must be low. Furthermore, the step size of perturbation should be high

enough that the noise cannot affect the controller while producing a noticeable change in the output of the solar array [71]. At low levels of irradiance, this technique is inefficient. This is the limitation of the P&O algorithm.

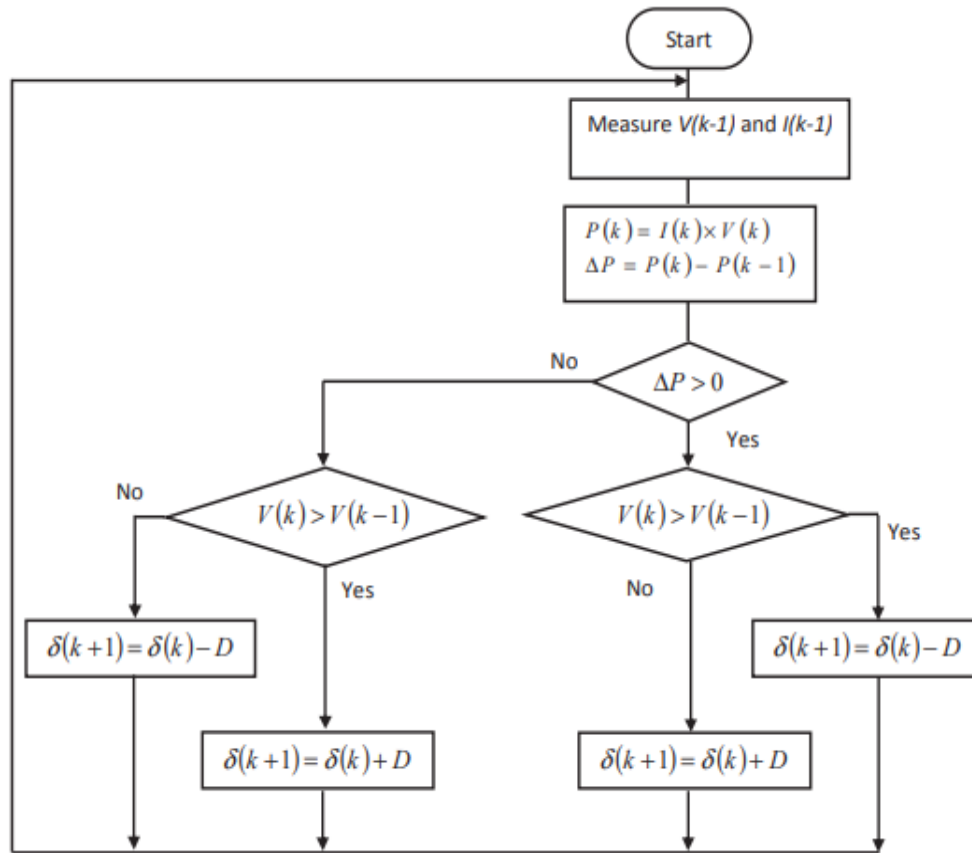


Figure 2. 5: P&O Algorithm [72]

2.6.2 Incremental Conductance (IC)

Figure 2.10 depicts the incremental conductance (IC) technique, which by leveraging the incremental conductance of PVs bypasses the limits of the perturbation and observation. When conductance equals the IC, the voltage operating point is found using this method. Currently, the system stops interfering with the working point. This approach has the advantage of knowing the relative "distance" to the MPP, allowing it to determine when the MPP has been reached. It can also track the MPP more precisely in highly variable weather conditions [73] and exhibits less oscillatory behavior around the MPP than the P

& O approach, even when optimized. The IC technique, on the other hand, has the issue of being unstable due to the use of a derivative operation in the algorithm. Furthermore, at low levels of insulation, the differentiation technique is difficult and susceptible to measurement noise, resulting in unsatisfactory findings [74]. IC tracking approaches, in general, have a constant step size of iteration that is determined by the necessary speed and accuracy. Raising it increases tracking speed while diminishing accuracy. Similarly, precision can be improved by reducing the step size, but it reduces the speed of convergence of the algorithm. To address this issue, B. Hyun Su et.al [75] proposed a technique of incremental conductance with adjustable step sizes. The step size is automatically adjusted by this technique. The algorithm increases the step size to reach the MPP quickly. The operating point is close to the point of operation, lower is the step size. Step size changes result in improved accuracy and speed.

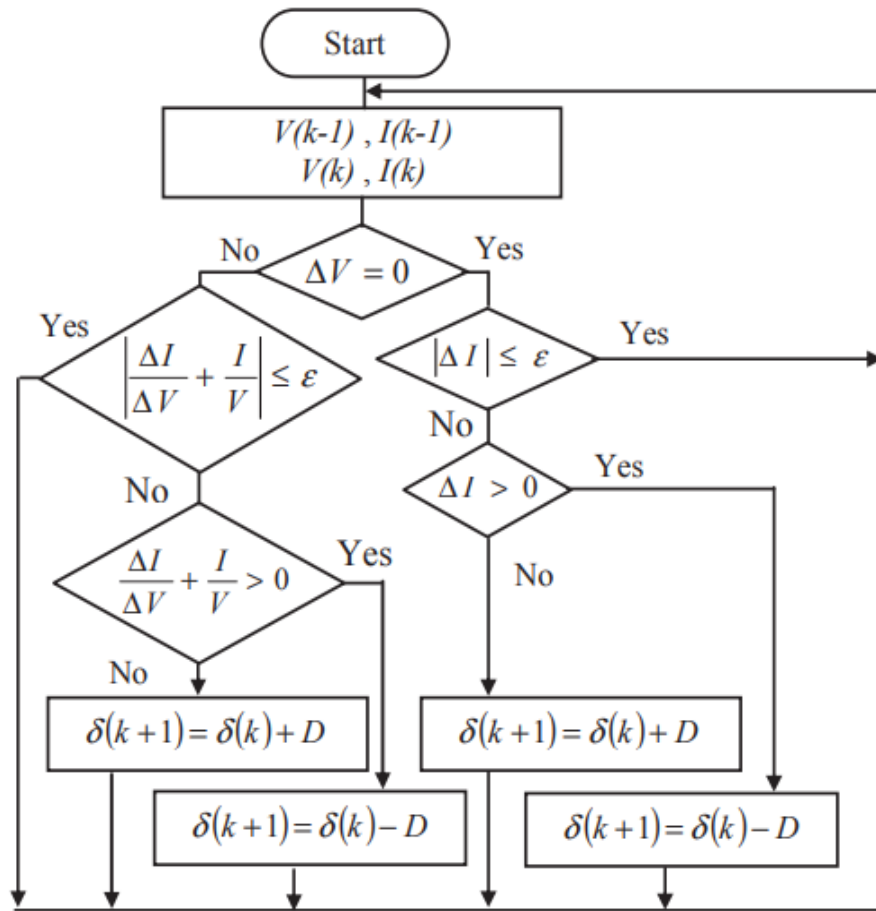


Figure 2. 6: IC Algorithm [72]

2.6.3 *Fuzzy Logic Control (FLC)*

Fuzzy logic control in MPP applications has risen in prominence [74]. The three phases of fuzzy logic controllers are lookup table, fuzzification, and defuzzification. To turn variables of numerical inputs into linguistic variables, multiple predefined membership functions are used by fuzzification. The controller will work more accurately when more membership functions used [76], [77]. An error signal is received by this technique, including the change of error. These signals are subsequently translated into verbal variables that represent the user's interaction with the system. Fuzzy logic control has the advantage of not requiring a precise model of mathematics and can manage non-linearity in the system. This technique has the disadvantage that it is dependent on the competency and knowledge of the user in picking the computation of error. As improved versions of this MPPT, adaptive algorithms that adjust the rule basis table in real-time and membership functions have been given [74].

2.6.4 *Neural Network (NN)*

T. Hiyama [78] and L. Zhang [79] described a neural network-based MPPT. This network is trained to interact with the data of PV and adapt the characteristics of the time-varying system so that it should function properly. This algorithm functions like a black box once it is trained and now no more information is required by this algorithm after training. Three layers of NN were defined by [78]: input, hidden, and the output layer. The user defines the nodes in each tier. Input variables are I_{sc} and V_{oc} . The Power converter is controlled by the signal duty cycle or reference signals which is the output signal. Hidden layers provide the MPP, and the performance of the system is dependent on the training of data of NN [80].

2.7 **Related Research**

Due to ease of fabrication, high efficiency, and fabrication cost, PSCs have developed as a favorable substitute to conventional cells of PV based on silicon. The performance of PSCs has progressed a lot over the past 10 years with more than 20% power conversion efficiencies. The enhancement of new perovskite materials, the incorporation

of new materials into the structure of the device, the improvement in the device's architecture, and many other different approaches made this PCE achievable. Progress and advancements in PSC's research, and the strategies implemented to improve the performance of PSC are overviewed and discussed in this section.

2.7.1 Modeling Solution of Vacancy Motion and Charge Transport in PSCs

For the simulation of charge carriers and ions transport in PSCs, a numerical method has been presented in [81]. The Monte Carlo method combined with a lattice-based approach to model the transport of charge carriers and ions, respectively, was proposed. It is demonstrated by the authors that the numerical method they proposed produces accurate results and is significantly faster than other commonly used numerical methods. A comparison of the developed method in this research is given and discussed with other numerical methods that are used to simulate ion and charge transport in PSCs. For optimizing the cell's performance and simulating the behavior of PSCs under different operating conditions, this methodology can be used.

2.7.2 Modeling of PSC with respect to Structural Similarity

A new model for PSCs is proposed in [82], structurally like thin film inorganic semiconductor solar cells. The operation mechanisms and device physics are compared between thin film solar cells and PSCs by the authors. It is concluded that these two solar cells have many similarities, such as the formation of a built-in potential, the presence of a heterojunction, and a depletion region. A model is developed by considering these similarities in this research that is composed of their unique properties i.e., the perovskite layer's high ionic conductivity and defect density. Experimental measurements and simulations are carried out to validate this model. It is demonstrated and depicted by the results that the model accurately evaluated the performance of PSCs. It is believed and claimed by the authors of this research paper that for designing new structures, and architecture, and optimizing the performance of PSCs, this device model can be useful.

2.7.3 *Progress in PSCs*

In [83], the recent progress and advancements in PSCs are proposed, comprehensively. Advantages and the key features of PSCs are discussed in this dissertation like lost cost, ease of fabrication, and high efficiency. The limitations and major challenges relating to PSCs are also highlighted by the authors i.e., PSC's durability and stability under real-world conditions. Device architecture and structures of PSCs and recent advancements in the materials with an in-depth discussion are provided in this article. The use of new electron and hole transport materials, the incorporation of new device architectures, and the development of new perovskite materials with improved stability, performance, and efficiency of PSCs are also included in the discussion.

The latest insights into the fundamental mechanisms and physics underlying the operation of PSCs, including the recombination processes and the charge carrier transport are reviewed. Furthermore, the effects of ion migration and defects on the performance of PSCs are also mentioned. The challenges relating to the increase in the production of PSCs, and the progress made in the commercialization of such devices are also discussed by the authors. New opportunities and directions relating to further research in this area are also identified and recommended in this review like integration of PSCs into building materials, multijunction PSCs, and tandem PSCs.

2.7.4 *Behavioral Modeling of PSCs*

PSC's behavioral model is proposed in [84]. Composition properties can be studied using this behavioral model. Initially, the basic properties of PSCs like operation, performance parameters, and are discussed. Then a behavioral model for PSCs is proposed considering their important properties, such as the lifetime of carrier of charge and mobility, and absorption coefficient. Simulations and experimental measurements are used to justify this proposed model. The results demonstrate that the performance of PSCs is accurately predicted by this model.

To study the relation between different compositional variations and the performance of PSCs, this model is used. Specifically, it investigates how the performance

of PSCs varies by changing the dopant concentration, cation concentration, and halide composition. Insights into the optimization and design of PSCs are also discussed in detail so that perovskite's performance and stability can be improved.

A valuable contribution to the area of PSCs is provided in this research paper that a new behavioral model can be beneficial and utilized to evaluate the properties of PSCs based on composition, design, and optimization.

2.7.5 *Tracking of MPP by a Predictive Algorithm*

The maximum power point tracking of PSCs is presented in [85] by developing a new predictive algorithm. PSCs have a common phenomenon of JV hysteresis, and it has a great impact on the performance and stability of PSCs. A recursive least-squares algorithm is proposed to track the MPP of hysteretic PSCs. Experiments and simulations are carried out to validate this algorithm and conclude that under different operating conditions, it tracks the MPP of hysteretic PSCs. A comparison of this algorithm is also made with the other MPPT techniques to check its performance and it performed very well as compared to other methods in terms of response time.

For optimizing the stability and performance of PSCs, this algorithm can be beneficial. PSCs or other cells with new architecture, this algorithm can also be used but improvements and changes will be required accordingly.

2.7.6 *Hysteresis in PSCs caused by Ion Migration's Numerical Modeling*

The challenges of PSC's development, and the presence of ion migration which is considered one of the causes of hysteresis in PSCs are discussed by Atul Kumar in [86]. PSC's numerical modeling with many approaches like atomic, mesoscopic, and device-level simulations are presented in this article too. The role of different parameters like electrode materials, device geometry, and composition of the absorber in hysteresis and ion migration are provided by these simulations. Understanding the complexity and importance of material and parameters in PSCs is also highlighted in this research paper.

2.7.7 *MPPT for Measurement of PCE of Metastable PSCs*

A new MPPT algorithm is developed to measure the PCE of metastable PSCs by Hidenori Saito et.al in [87]. To determine the optimized operating point of the PSC so that the accuracy of measuring the PCE of the PSC can be improved, a perturbation signal is used.

The proposed MPPT's design and its implementation are presented, and its validity is checked by comparing experimental results with the conventional MPPT techniques. It is shown by this comparison that the more accurate results in terms of PCE for metastable PSCs are obtained by implementing the proposed algorithm. The importance of accurate PCE for evaluating the performance of PSCs is highlighted and discussed in this article. It is concluded by the authors that the proposed MPPT can be a useful method in improving the efficiency, stability, and accuracy of the measurements of metastable PSC's performance parameters, especially PCE.

2.8 Limitations and Bottlenecks of the Existing Work

There is many progress has been made in the research area relating to PSCs but there are still several limitations present in this area of research. The main bottlenecks in the previous related work are highlighted below:

- In PSCs, one of the main limitations is that they are not very stable and still degrade over time. This limits the durability, reliability, and their performance. To improve the PSC's stability, a lot of research is still required.
- Some of the perovskite materials contain toxic components that react with other materials and are also not beneficial for human health like lead. Perovskite materials that are sustainable and non-toxic are important in PSC so that they can be utilized widely.
- PSCs face variable outcomes in performance when developed under the same conditions and properties. This variability is very challenging in optimization and scale-up to commercialization of PSCs.

- There is also a limitation in the availability of raw materials required for the production of PSCs like lead. The extraction of this material can also have an impact on the environment. Developing alternative and sustainable materials is crucial for reducing the environmental impact and ensuring the scalability of PSCs.
- Integration of solar cell architecture and technology with PSCs is very much needed because practical challenges can only be addressed by this integration.

In the renewable industry, it is very important to address these limitations and bottlenecks so that PSCs can be utilized as a sustainable and viable option in the power production industry. To overcome these challenges and issues, more intense development and research efforts are required so that the true potential of PSCs can be realized effectively.

2.9 Summary

In this chapter, the complete history and evolution of PSCs with their associated literature is discussed. The development of PSCs, related technologies, and hysteresis and their influential factors in PSC are also discussed. The related research work already done in the past in the same field is also mentioned and based on their limitations, defines the problem statement in the end.

CHAPTER 3: MODELING OF PEROVSKITE SOLAR CELL IN MATLAB

The tools of quantum mechanics provide a good description of the foundations of semiconductor physics. According to this perspective, functions of waves define the electrons, the wavelength and frequency of which are connected to the energy and momentum of the particle. This model allows us to understand particle behavior at the atomistic level. In semiconductors, wave packets characterize the electrons very well. The Schrödinger equation, which is at the core of quantum mechanics, can be solved using the wave packet energy and momentum. As a result, the particle's motion may be summed up as a single wave packet that is affected by both the crystal lattice interaction and outside influences [88].

In comparison to semiconductor lattice dimensions, device modeling represents the charge transport problem on a macroscopic scale. This approach assumes Newton's law for electron mobility between collisions and quantum mechanics for interactions with lattice. Distribution functions can be used to describe carriers, obtained by the solution of the equation of Boltzmann. The model of drift-diffusion is a practical system of equations derived from idealistic simplifications of the Boltzmann equation, which is challenging to achieve. These equations are often known as the basic semiconductor equations. They are simply derived from Maxwell's equations 3.1 to 3.6 [89], as demonstrated in the following paragraphs.

$$\nabla * H = J + \frac{\partial D}{\partial t} \quad (3.1)$$

$$\nabla * E = -\frac{\partial B}{\partial t} \quad (3.2)$$

$$\nabla * H = \rho \quad (3.3)$$

$$\nabla * B = 0 \quad (3.4)$$

Where, the electric field is denoted by E , magnetic field by H , electric induction by D , magnetic induction by B , current density by J , and space charge density by ρ .

$$D = \varepsilon E \quad (3.5)$$

$$B = \mu H \quad (3.6)$$

where ε denotes permittivity and μ permeability of the medium.

3.1 Drift Diffusion Method

The Drift-diffusion approach relies heavily on the transport of charges concept. In this section, a model of transport of charges for a planar lead halide PSC with an absorber layer as perovskite between an ETL and HTL[90].

The PSC's structure is shown in Figure 3.1 in which the three-layered standard planar architecture of PSC is highlighted.

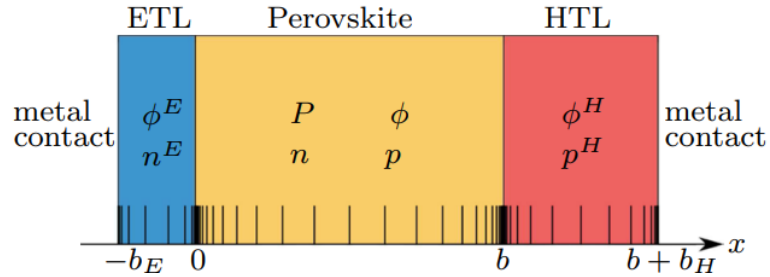


Figure 3. 1: Three-Layered Planar Architecture of PSC [91]

3.1.1 Mathematical Modeling and Equations

The mathematical modeling and equations 3.7 to 3.50 are used from [88], [89], [92], [93], [94]. There are three layers in the planar structure of PSC as shown in Figure 3.1,

1. ETL ($-\mathbf{b}_E < \mathbf{x} < \mathbf{0}$)
2. Absorber layer (perovskite) ($\mathbf{0} < \mathbf{x} < \mathbf{b}$)
3. HTL ($\mathbf{b} > \mathbf{x} > \mathbf{b} + \mathbf{b}_H$)

The mathematical equations corresponding to each layer are as follows:

3.1.1.1 Absorber Layer – Perovskite

The perovskite layer model includes conservation equations for halide ion vacancies, holes, and free electrons, as well as for the $\Phi(x, t)$ – electric potential, Poisson equation. The density of vacancy of the mean ion is defined as N_0 , the flux is defined by $F^P(x, t)$, and the vacancy density of the halide is defined as $P(x, t)$. The layer of perovskite is assumed to have a uniform density of immobile cation vacancies, denoted as N_0 . j_n corresponds to the concentration of electrons n , and j_p corresponds to the concentration of holes p . The charge carrier photogeneration is represented by the $G(x, t)$ function, and the bulk recombination rate is denoted by $R(n, p)$ function. So, we have the following equation in the perovskite layer:

$$\frac{\partial p}{\partial t} + \frac{1}{q} \frac{\partial j^p}{\partial x} = G(x, t) - R(n, p) \quad (3.7)$$

$$j^p = -qD_p \left(\frac{\partial p}{\partial x} + \frac{p}{V_T} \frac{\partial \Phi}{\partial x} \right) \quad (3.8)$$

$$\frac{\partial n}{\partial t} - \frac{1}{q} \frac{\partial j^n}{\partial x} = G(x, t) - R(n, p) \quad (3.9)$$

$$\frac{\partial p}{\partial t} + \frac{\partial F^P}{\partial x} = 0 \quad (3.10)$$

$$F^n = -D_I \left(\frac{\partial P}{\partial x} + \frac{P}{V_T} \frac{\partial \Phi}{\partial x} \right) \quad (3.11)$$

By using the Poisson equation,

$$\frac{\partial^2 \phi}{\partial x^2} = \frac{q}{\epsilon_A} (N_0 - P + n - p) \quad (3.12)$$

Here, the coefficient of diffusion of the vacancies of iodide ion is denoted by D_I , and the absorber layer's (perovskite) permittivity is denoted by ϵ_A .

Conditions for the continuity with transport layers, at the interfaces, are responsible for these differential equations which are discussed in section 3.1.1.4.

3.1.1.2 ETL – Electron Transport Layer

Free electrons act as the majority carriers in the ETL. The Poisson equation coupled with the equation of conservation, ETL is modeled. The coefficient of electron diffusion is denoted by D_E , and the permittivity by ϵ_E , and density of free electrons (owing to doping) is represented by d_E in the ETL.

$$\frac{\partial n}{\partial t} - \frac{1}{q} \frac{\partial j^n}{\partial x} = 0 \quad (3.13)$$

$$j^n = qD_n \left(\frac{\partial n}{\partial x} - \frac{n}{V_T} \frac{\partial \phi}{\partial x} \right) \quad (3.14)$$

$$\frac{\partial^2 \phi}{\partial x^2} = \frac{q}{\epsilon_E} (n - d_E) \quad (3.15)$$

Continuity conditions at the interface are used to couple these equations to the perovskite layer. Continuity conditions are discussed in section 3.1.1.4.

Ohmic boundary conditions are applied to the exterior boundary with the metal contact that is,

$$n = d_E \quad (3.16)$$

Where on $x = -b_E$;

$$\phi = \frac{V_{bi} - V(t)}{2} \quad (3.17)$$

Here, built-in voltage is denoted by V_{bi} , and applied voltage by $V(t)$.

3.1.1.3 HTL – Hole Transport Layer

Holes act as the majority carriers in the HTL. The equations that need to be specified in this case are:

$$\frac{\partial p}{\partial t} + \frac{1}{q} \frac{\partial j^p}{\partial x} = 0 \quad (3.18)$$

$$j^p = -qD_H \left(\frac{\partial p}{\partial x} - \frac{p}{V_T} \frac{\partial \phi}{\partial x} \right) \quad (3.19)$$

$$\frac{\partial^2 \phi}{\partial x^2} = \frac{q}{\epsilon_H} (d_H - \rho) \quad (3.20)$$

Here, intrinsic hole density is represented by d_H , hole diffusion coefficient by D_H , ϵ_H is the permittivity.

Perovskite's equations are coupled with the equation 3.19 to 3.21 using the conditions of continuity. The conditions of Ohmic contact are also satisfied with the metal contact.

$$p = d_H \quad (3.21)$$

where at $x = b+b_H$;

$$\phi = -\frac{V_{bi} - V(t)}{2} \quad (3.22)$$

3.1.1.4 Continuity Conditions at the Interfaces

1. ETL interface / Perovskite

The assumptions associated with these conditions are:

- Electrostatic potential and electric displacement fields both are continuous.
- Vacancies of halide ions have no flux.
- The current density associated with electron flux is conserved.
- ETL's electron density and density of carrier are proportional to each other by the k_E factor, determined by the amendment in the effective density of states and a relevant band of set.
- The current density associated with hole flux is conserved.

Hence, the conditions used for interface ETL / Perovskite are mentioned in equations 3.24 to 3.29.

When x is zero;

$$j^n|_{x=0^-} = j^n|_{x=0^+} - \bar{R}_l \quad (3.23)$$

$$j^p = -q\bar{R}_l \quad (3.24)$$

$$F^p = 0 \quad (3.25)$$

$$\phi|_{x=0^-} = \phi|_{x=0^+} \quad (3.26)$$

$$\epsilon_E \frac{\partial \phi}{\partial x} |_{x=0^-} = \epsilon_A \frac{\partial \phi}{\partial x} |_{x=0^+} \quad (3.27)$$

$$k_E n |_{x=0^-} = n |_{x=0^+} \quad (3.28)$$

2. Perovskite / HTL Interface

At $x = b$;

$$j^p|_{x=b^-} - \bar{R}_r = j^p|_{x=b^+} \quad (3.29)$$

$$j^n = -q\bar{R}_r \quad (3.30)$$

$$\phi|_{x=b^-} = \phi|_{x=b^+} \quad (3.31)$$

$$\epsilon_A \frac{\partial \phi}{\partial x} |_{x=b^-} = \epsilon_H \frac{\partial \phi}{\partial x} |_{x=b^+} \quad (3.32)$$

$$p|_{x=b^-} = k_H p|_{x=b^+} \quad (3.33)$$

- Left side recombination is denoted by R_l (ETL / Perovskite).
- Right-side recombination is denoted by R_r (Perovskite / HTL).
- Constants between concentrations of charge carriers are k_E and k_H .

$$k_E = \frac{g_C}{g_C^E} \exp\left(-\frac{E_C - E_C^E}{k_B T}\right) \quad (3.34)$$

$$k_H = \frac{g_V}{g_V^H} \exp\left(\frac{E_V - E_V^H}{k_B T}\right) \quad (3.35)$$

where effective conduction is denoted by g_c , and the state density of the valence band is denoted by g_v . The energy of the conduction band is by E_C , and the energy of the valence band is by E_V . These formulae rely on the Boltzmann approximation, which describes electron distribution in a non-degenerate semiconductor. The density of effective doping should be 20 times less than the density of states for the confirmation of equilibrium is a few thermal voltages away and more from the boundaries of the band.

3.1.1.5 V_{bi} – Built-in Voltage

The work function's difference between two contacts of metals defines the PSC's built-in voltage. Assuming optimal Ohmic contacts with the next transport layer, the difference

of levels of Fermi can be estimated by statistics of Boltzmann.

$$E_f^E = E_C^E - k_B T \log \left(\frac{g_C^E}{d_E} \right) \quad (3.36)$$

$$E_f^H = E_V^H + k_B T \log \left(\frac{g_V^H}{d_H} \right) \quad (3.37)$$

So, the built-in voltage is:

$$V_{bi} = E_C^E - E_V^H - k_B T \log \left(\frac{g_C^E g_V^H}{d_E d_H} \right) \quad (3.38)$$

3.1.1.6 Generation and Recombination Rates

A relation is defined by Courtier et.al [91], [95] to evaluate the generation rate of carrier of charge shown in equation 3.41.

$$G(x, t) = I_S(t) F_{ph} \alpha \exp \left(-\alpha \left[\frac{b}{2} + l \left(x - \frac{b}{2} \right) \right] \right) \quad (3.39)$$

where F_{ph} is the flux of photons, $I_S(t)$ denotes irradiance and the parameter 'l' selection can be done as per the desired entrance of illumination i.e., -1 from the right (through the HTL) and +1 from the left.

Courtier et.al also defined bulk recombination as a combination of trap-assisted Shockley-Read-Hall (SRH) and bimolecular mechanisms of recombination. So, equation 3.42 shows the relation of the rate of bulk recombination.

$$R(n, p) = \beta(np - n_i^2) + \frac{np - n_i^2}{\tau_n(p + p_t) + \tau_p(n + n_t)} \quad (3.40)$$

here, the bimolecular rate constant is denoted by β , intrinsic carrier concentration is n_i charge carrier lifetimes are denoted by τ_n and τ_p . Assuming the energy level of the trap state and intrinsic energy of perovskite's potential are close to each other, the following approximation can be used:

$$p_t = n_i = n_t \quad (3.41)$$

The \bar{R}_l and \bar{R}_r , fluxes of interfacial recombination fluxes, are given by the combination of SRH, and bimolecular recombination, using the approximation, as follows:

At $x = 0^+$:

$$\bar{R}_l \left(\frac{n}{k_E}, p \right) = \frac{\beta^E}{k_E} (np - n_i^2) + \frac{np - n_i^2}{\frac{k_E}{v_n^E} (p + n_i) + \frac{1}{v_p^E} (n + n_i)} \quad (3.42)$$

At $x = b$:

$$\bar{R}_r \left(n, \frac{p}{k_H} \right) = \frac{\beta^H}{k_H} (np - n_i^2) + \frac{np - n_i^2}{\frac{1}{v_n^H} (p + n_i) + \frac{k_H}{v_p^H} (n + n_i)} \quad (3.43)$$

3.1.1.7 J – Total Current Density

Total current density is calculated by the relation developed by [91], [95], obtained by solving the drift-diffusion numerically and shown in equation 3.46. In the same domain, this equation can be used anywhere. The density of current is estimated at the center of perovskite, where the spacing of the grid is bigger and to reduce the inaccuracy in the numerical solution, the solution becomes smoother than in the layers of Debye.

$$J(t) = \begin{cases} j^n + j^p - \frac{\partial}{\partial t} \left(\varepsilon_A \frac{\partial \phi}{\partial x} \right) + qF^P, & \text{for } 0 < x < b \\ j^n - \frac{\partial}{\partial t} \left(\varepsilon_E \frac{\partial \phi}{\partial x} \right), & \text{for } -b_E < x < 0 \\ j^p - \frac{\partial}{\partial t} \left(\varepsilon_H \frac{\partial \phi}{\partial x} \right), & \text{for } b < x < b + b_H \end{cases} \quad (3.44)$$

3.2 Grid Discretization

A numerical method is developed in [90], [91], [95] that solves the PSC model in the program. The model assumed uniform potential within the transport layers, reducing the equations to the perovskite absorber layer. The finite element approach is used for a three-layered model's solution.

The computational grid defines the discretization with points that are positioned non-uniformly 'N + N_E + N_H + 1'. The $x \in [-w_E, 1 + w_H]$ domain is divided into subintervals like 'N + N_E + N_H'. N + 1 grid points are present in the layer of perovskite by including the interfaces, designated by 'x = x_i where i = 0, ..., N'. $\Delta_{i+1/2} = x_{i+1} - x_i$ are the widths of subintervals. N_E and N_H are the grid points of ETL and HTL, respectively, these are represented as x = x_E for i = 0, ..., N_E - 1 and x = x_H for i = 1, ..., N_H, having appropriate notations.

If the 'tanh' is extended, given in [90], [91], [95], then a grid can be formed.

$$x_i = \frac{1}{2} \left[\frac{\tanh \left[s \left(\frac{2i}{N} - 1 \right) + 1 \right]}{\tanh(s)} \right], \quad \text{for } i = 0, \dots, N \quad (3.45)$$

$$x_i^E = \frac{w_E}{2} \left[\frac{\tanh \left[s \left(\frac{2i}{N_E} - 1 \right) - 1 \right]}{\tanh(s)} \right], \quad \text{for } i = 0, \dots, N_E - 1 \quad (3.46)$$

$$x_i^H = \frac{w_H}{2} \left[\frac{\tanh \left[s \left(\frac{2i}{N_H} - 1 \right) + 1 \right]}{\tanh(s)} \right], \quad \text{for } i = 0, \dots, N_H \quad (3.47)$$

According to numerical studies, a good general rule of thumb is to set s so that 20 percent of points of the grid should be within one Debye length of the perovskite's interface that is, $x \in [1 - \lambda, 1]$ and $x \in [0, \lambda]$ after solving the equation 3.50.

$$\lambda = \frac{1}{2} \left(\frac{\tanh(0.6)}{\tanh(x)} + 1 \right) \quad (3.48)$$

The algorithm selects grid points N_E and N_H , resulting in roughly equal spacing on both sides of the interface based on N (input).

3.3 Implementation in MATLAB

[95] developed a robust numerical solver, based on the method of drift-diffusion, known as IonMonger, to analyze the performance of PSC using MATLAB. This method employs MATLAB's ode15s integrator to evolve the system over time while employing the discretization of the finite element scheme in the spatial dimension. Stiff differential algebraic equations can be handled by the solver, utilizing a variety of numerical methods, including a nonlinear adaptive time-step and grid [90], [91].

The steps involved in the implementation of IonMonger by [91] the solutions of experimental simulations for analysis of different parameters of perovskite solar cells are shown in Figure 3.2.

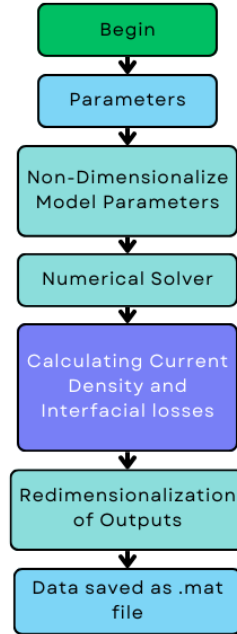


Figure 3. 2: Implementation Flow Chart in MATLAB

The details of each step are as follows:

3.3.1 *Input Parameters and Initial Conditions*

In IonMonger [81], [91],[95] ‘params’ is defined as a MATLAB structure that is passed between different functions of the whole algorithm environment. It contains the voltage protocol $V(t)$, illumination protocol $G(x, t)$, solver options, and all the necessary parameters required in the computation of the system and getting the desired outputs. The parameters used in this research work are shown as:

Table 3.1 contains the values used for the resolution and error tolerances, the physical constants, perovskite parameters, HTL and ETL parameters, ion parameters, bulk recombination, and interface recombination parameters.

Table 3. 1: Input Parameters Used [90], [93], [96]

| Resolution and Error Tolerance | |
|--|-------------------------|
| Number of sub-intervals | N = 400 |
| Solver's Tolerance (ode15s) – relative | 10^{-6} |
| Solver's Tolerance (ode15s) – Absolute | 1e-10 |
| Electric potential's displacement factor (V_T) | 100 |
| Physical Constants | |
| Incident photon flux (m^2 / s) | 1.4×10^{21} |
| Permittivity of free space (F / m) | 8.85×10^{-12} |
| Charge (C) | 1.602×10^{-19} |
| Boltzmann constant (eV / K) | 8.617×10^{-5} |
| Illumination's Direction ['false' for a standard architecture cell (light entering from ETL), 'true' for an inverted architecture cell (light entering from HTL)] | false; |
| Perovskite Parameters | |
| Temperature (K) | 300 |
| Perovskite layer width (m) | 300×10^{-9} |
| Permittivity (F / m) | 24.1*eps0 |
| Absorption coefficient (m^{-1}) | 1.3×10^7 |
| Minimum conduction band (eV) | -3.7 |
| Maximum valence band (eV) | -5.4 |
| Diffusion coefficient of Perovskite's electron (m^2/s) | 1.7×10^{-4} |
| Diffusion coefficient of Perovskite's hole (m^2/s) | 1.7×10^{-4} |
| The density of states of the conduction band (m^{-3}) | 8.1×10^{24} |
| The density of states of the valence band (m^{-3}) | 5.8×10^{24} |
| ETL Parameters | |
| Effective doping density (m^{-3}) | 10^{24} |
| Doped electron quasi-Fermi level (eV) | -4.1 |
| Effective conduction band DoS (m^{-3}) | 5×10^{25} |
| Reference energy of conduction band (eV) | -4.0 |
| Width (m) | 100×10^{-9} |
| Permittivity (F/m) | 10*eps0 |
| Electron diffusion coefficient (m^2 / s) | 10^{-5} |
| Electron mobility ($m^2/V/s$) | 3.8×10^{-4} |
| HTL Parameters | |
| Effective doping density (m^{-3}) | 10^{24} |
| Doped electron quasi-Fermi level (eV) | -4.9 |
| Effective conduction band DoS (m^{-3}) | 5×10^{25} |
| Reference energy of conduction band (eV) | -5.1 |
| Width (m) | 200×10^{-9} |
| Permittivity (F/m) | 3*eps0 |
| Electron diffusion coefficient (m^2 / s) | 10^{-6} |
| Electron mobility ($m^2/V/s$) | 3.8×10^{-5} |
| Ion Parameters | |

| | |
|---|---|
| Typical density of ion vacancies (m^{-3}) | 1.6×10^{25} |
| Diffusivity relation | $D = @(D_{inf}, EA)$ $D_{inf} * \exp(-EA/(k_B * T))$ |
| High-temp. vacancy diffusion coefficient (m^2/s) | 6.5×10^{-8} |
| Activation energy iodide vacancy (eV) | 0.58 |
| Iodide ion's diffusion coefficient (m^2/s) | $DI = D (DI_{inf}, EAI)$ |
| Bulk Recombination | |
| Pseudo-lifetime of electron for SRH (s) | 3×10^{-9} |
| Pseudo-lifetime of the hole for SRH (s) | 3×10^{-7} |
| Bimolecular recombination rate (m^3/s) | 0 |
| Electron-dominated Auger recombination rate (m^6/s) | 0 |
| Auger recombination rate dominated by hole (m^6/s) | 0 |
| Interfacial Recombination (max. velocity = 1×10^5) | |
| Effective ETL/perovskite bimolecular rate (m^3/s) | 0 |
| Effective bimolecular rate of perovskite/HTL (m^3/s) | 0 |
| Electron recombination velocity for SRH (m/s) | 10^5 |
| The velocity of recombination of the hole for SRH (m/s) | 10 |
| The velocity of recombination of electron for SRH (m/s) | 0.1 |
| Effective hole's velocity of recombination SRH (m/s) | 10^5 |

It is difficult to find the initial conditions that satisfy the required constraints for boundary. The code describes the initial configuration of a quasi-equilibrium device, where the $V(t)$ is set to the V_{oc} . This guarantees that the cell will not generate any current. The first step in identifying the initial conditions where the $V(t)$ equals the V_{bi} is to obtain an authentic solution at a steady state for the model of PSC. The function `initial_conditions.m` takes on this job. An extra attempt is subsequently made to whichever `precondition.m` or `find_Voc.m`, respectively, to begin the simulation process from open-circuit conditions or a different applied voltage value.

3.3.2 *Non-Dimensionalization of Model Parameters*

In the [91], [95], the program gives the solution of dimensionless parameters, and the output is then re-dimensionalized automatically by the code. The following equations demonstrate the non-dimensionalization of the model parameters.

$$x = bx^* \quad (3.49)$$

$$t = \tau_{ion}t^* \quad (3.50)$$

$$\phi = V_T\phi^* \quad (3.51)$$

$$p = d_H p^* \quad (3.52)$$

$$n = d_E n^* \quad (3.53)$$

$$P = N_0^{\wedge} P^* \quad (3.54)$$

$$j^p = qG_0 b j^{p*} \quad (3.55)$$

$$j^n = qG_0 b j^{n*} \quad (3.56)$$

$$F^P = \frac{D_I N_0^{\wedge}}{b} F^{P*} \quad (3.57)$$

Here, the characteristic timeframe for the mobility of ions into the Debye layers is represented by τ_{ion} , and G_0 is the value of G , given by

$$G_0 = \frac{Fph}{b} (1 - e^{-ab}) \quad (3.58)$$

$$\tau_{ion} = \frac{b}{D_I} \sqrt{\frac{V_T \epsilon_A}{qN_0^\wedge}} \quad (3.59)$$

The Debye length of perovskite is given as

$$L_D = \sqrt{\frac{V_T \epsilon_A}{qN_0^\wedge}} \quad (3.60)$$

Similarly, the other constants and input functions are rescaled and non-dimensionalized in the same way, as mentioned in [91], [95].

3.3.3 Numerical Solver

A finite element scheme is used by the [89], [91], [93], [95], specifically in IonMonger to get the solution of the system of equations numerically in which each dependent variable is roughly represented as a combination (linear) of compactly supported piecewise linear basis functions.

From the solution given by IonMonger (dimensionless), the total current density is by using equations 3.63 and 3.64:

$$J(t) = j_{k+\frac{1}{2}}^n + j_{k+\frac{1}{2}}^p - \frac{\epsilon_A V_T}{\hat{t}qG_0 b^2 \tau_{ion}} \left(\frac{\phi_{k+1} - \phi_k}{\Delta_{k+\frac{1}{2}}} |_{t-\hat{t}} - \frac{\phi_{k+1} - \phi_k}{\Delta_{k+\frac{1}{2}}} |_{t-t^\wedge} \right) + \frac{D_I N_0^\wedge}{G_0 b^2} F_{k+\frac{1}{2}}^P \quad (3.61)$$

Here, the grid point index at the midpoint of the perovskite layer is denoted by:

$$k = \text{ceil}\left(\frac{N + 1}{2}\right) \quad (3.62)$$

It is seen that the impact of the third and fourth term is very small as compared to the addition of the first two terms. Before re-dimensionalization, the density of current losses due to interfacial recombination is estimated with the total current density by using the equations 3.65 and 3.66.

$$J_l(t) = -\bar{R}_l\left(\frac{n_l}{k_E}, p_l\right) \quad (3.63)$$

$$J_r(t) = -\bar{R}_r\left(n_N, \frac{p_N}{k_H}\right) \quad (3.64)$$

Finally, the solution that is carried out by the IonMonger is re-dimensionalized, as mentioned by Courtier et.al in [91], [95], and by Anderson in [93] and save all the solution variables like ϕ , ϕ^E , ϕ^H , n^E , P , n , p , p^H , time, spatial vector x , x_E , and x_H , applied voltage and current densities in .mat data file.

3.4 Summary

Drift-diffusion method is the technique that is used to analyze the performance parameters and characteristics of PSC. In this chapter, the mathematical modeling and equations that are associated with the drift-diffusion method are discussed in detail. IonMonger, designed and formulated by Courtier et.al [91], [95] is used to implement the drift-diffusion method in MATLAB. The flow of the code is also discussed in which after initializing all the necessary input parameters, the model parameters are converted to dimensionless parameters which are required to process and get the desired solutions. The function params.m is then passed to the numerical solver i.e., Finite Element Scheme to process, and provide the calculated outputs like the current densities and their associated losses. After that, the outputs are converted from dimensionless to dimensionalized outputs, and all the data is saved in a .mat data file.

CHAPTER 4: RANDOM FOREST REGRESSION BASED MPPT

MPPT is a technique that predicts the maximum available power in a solar PV system and ensures that the PV system continuously controls this MPP despite any fault or changing conditions. Various MPPT algorithms have been developed for maximum power tracking in solar PV systems like Incremental Conductance, Perturb and Observe, Simple Neural Network, and Fuzzy Logic Control. Besides the advantages of these techniques, there are certain drawbacks (discussed in Chapter 2). Specifically, in the case of PSC, these techniques underestimate or overestimate the performance of PSC, majorly because of the occurrence of hysteresis in the JV curve.

For this reason, a novel MPPT technique is developed that is based on a machine learning model named Random Forest Regression.

4.1 Random Forest Regression – RFR-MPPT

Random Forest Regression (RFR) is a technique of machine learning that uses the concept of ensemble learning to make predictions. Ensemble learning is a method in which the outcomes of all the models are averaged to give the final outcome. Random Forest (RF) is a collection of multiple decision trees, and each tree is different from the other decision trees. It operates by averaging all the predictions of each tree in the forest. The idea of building RF was based on the main drawback of decision trees which is that the single decision tree might provide a good prediction but it overfits the training data. So, if many trees are built together, each tree has the overfitting of data, and the impact of overfitting gets reduced by averaging the results obtained. In building a good RF, many decision trees need to be built; every decision tree should predict the acceptable target and it should also be different from other decision trees. RFs inject randomness when building the decision trees so that each tree should be different from the other one. The steps involved in the procedure of the RF algorithm are,

1. Bootstrap sampling
2. Construction of decision trees
3. Prediction Aggregation

4.1.1 *Bootstrap Sampling*

Bootstrap Sampling also known as ‘Bagging’ is a method in which the RF randomly selects the subsets of data with replacement from the original dataset. These subsets are used then to train the decision trees. Each subset of data is used to train each tree in the forest. For example, if there are T samples of training, B bootstrap samples will be generated. This bootstrap sampling is done randomly by selecting T samples from the original data with replacement. The bootstrap sampling is a crucial part of RFR because it adds randomness. The main reasons for its importance for RFR are;

- It ensures the diversity in the building of trees which means that every decision tree has a different training data. This leads to the fact that each tree is not identical to the other tree and can capture various aspects of data.
- It reduces the overfitting problem that occurs in deep decision trees mostly. So, RF reduces this overfitting because there is a diverse subset of data for decision trees in RF, and averaging the outcomes of each tree ultimately reduces the overfitting of data.

4.1.2 *Construction of Decision Trees*

A decision tree splits the data based on the features so that the error in predicting the values of labels can be minimized. Decision trees are the basics of random forests. Due to the overfitting problem of decision trees, the random forest technique is used so that the problem of overfitting can be overcome. Splitting the nodes has many advantages relating to this problem and in the random forest regression algorithm to ensure every tree provides a unique outcome because of the bootstrap sampling. There are many other objectives for splitting the nodes in the construction of decision trees but the major objective of this splitting of data is to make sure that the label values remain homogeneous.

A decision tree is created for each bootstrap sample. For it, two things are required;

- Splitting of nodes in which, from all features, a subset of randomly selected features is used and for the best split to be selected, equation 4.1 is used

$$Best\ Split = \min \left(\frac{1}{N_L} \sum_{i \in L} (y_i - \hat{y}_L)^2 + \frac{1}{N_R} \sum_{i \in R} (y_i - \hat{y}_R)^2 \right) \quad (4.1)$$

where R and L are the right and left nodes extracted from the splits, the number of samples is denoted by N_R and N_L and mean values of the target are denoted by \hat{y}_R and \hat{y}_L .

- The tree grows in a repetitive method until a stopping criterion is not met. In this regression task, the Mean square error is used which is shown in equation 4.2.

$$MSE = \frac{\sum_{x=1}^n (\text{predicted value}_x - \text{Actual value}_x)^2}{n} \quad (4.2)$$

4.1.3 Prediction Aggregation

After the construction of decision trees, the Random Forest Regression predicts the final prediction of the system by averaging the outcomes of all individual decision trees. In mathematical form, it is shown in equation 4.3.

The averaging of predictions of all decision trees helps reduce the overfitting problem that occurs in the decision trees especially when the trees are deep. The decision tree technique is very useful in regression tasks but due to the overfitting problem in bigger scenarios, it cannot be used as the predictions become doubtful. So, RFR resolves this issue effectively by averaging the predictions of each tree in the forest. This lowers the impact of overfitting collectively.

The proposed strategy for extracting maximum power from PSC by using a Random Forest Regressor has two phases shown in Figure 3.3. One is the data collection and creation of the RF model. The second is to implement the RF model to predict the true maximum power point.

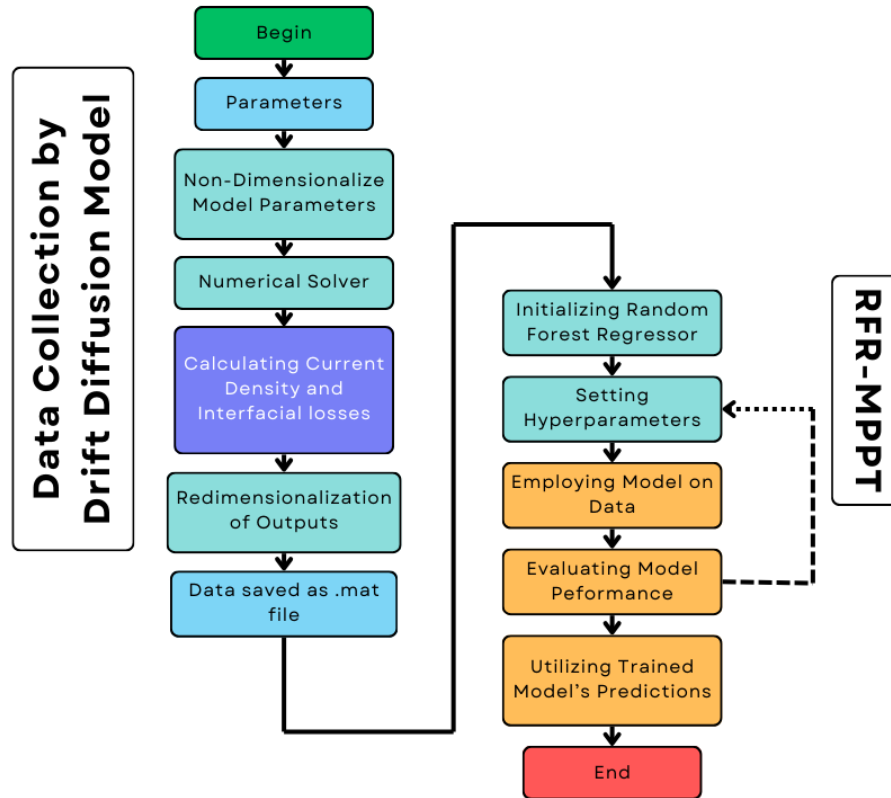


Figure 4. 1: RFR-MPPT's Flow Chart

4.1.4 Data Collection and Building of Random Forest (RF) Model

The voltage and current density data are required to employ the MPPT model so that the maximum power from PSC can be predicted. So, the parameters gathered from the modeling of PSC, as discussed previously, were used as the data for the MPPT. The forward and reverse scan voltages and current densities are saved in a .mat file along with the calculated forward and reverse scan powers and this data is used as the input data to the MPPT model. The reason for using both forward and reverse scan results is that it is required to predict the maximum power of PSC under its J-V hysteresis.

The forward and reverse voltages and currents are the features of the dataset whereas the calculated forward and reverse powers are the labels.

The process that is followed in the implementation of random forest regression mppt is shown in Figure 4.1. Each step is discussed in detail below;

The first step is the initialization of random forest regression. In this step, the dataset is loaded which is created by using the drift-diffusion modeling of perovskite solar cells. Forward and reverse scan voltages, current densities, and respective power are included in the dataset.

Forward and reverse scan voltages and currents were declared as features, and forward and reverse scan powers were declared as the target variables. 80% of data was assigned for the training set and 20% for the testing set. This split of data for training and testing is done by comparing the results with other combinations.

The second step is to do the settings of the hyperparameters for random forest regression. The hyperparameters are very important in any machine learning algorithm and their setting values have a direct impact on the predictions of the target. Here, for random forest regression, the important hyperparameters are

- The number of estimators
- Maximum depth
- Minimum samples split
- Minimum samples of leaf
- Maximum features
- Bootstrap Sampling
- Random states

The number of estimators defines the number of decision trees in the random forest regression. There is no direct method to calculate the best number of estimators for a given problem. By hit and trial method, this setting is performed. In this RFR-MPPT, the number of estimators is 100. This setting is performed because below 100, the variance of the algorithm increased, and above 100 there is a marginal effect in the predictions, but overfitting of data is seen. So, that's why the number of estimators is set to 100.

The rest of the hyperparameters were used as default because the random forest regression was used to extract the maximum power from perovskite solar cells under the hysteresis it has. So, if we do not go deep down to the building of decision trees, there is a chance of underestimating or overestimating the performance of perovskite solar cells. Setting these hyperparameters to default ensures that the final prediction has no ambiguity in describing the true performance of perovskite solar cells specifically under the noticeable hysteresis.

The random states hyperparameter is set to 42. It is just a number but by fixing random states, the results can be reproducible. If random states are not fixed, the results will change after every experiment.

4.1.5 *Prediction Strategy for RFR-MPPT*

The random forest is based on the number of decision trees that connect to form a forest i.e., the number of estimators. In Random Forest, each decision tree is built independently from other trees and to make sure each tree is different from the other ones, the algorithm makes random choices. The random forest randomly selects the features and evaluates for the best available test involving one of these features.

After the splitting of data into training data and testing data and building of different trees based on the number of estimators, the prediction of each tree in the RF is made by the algorithm, and then the results of each tree obtained are averaged to get the MPP of the PSC. In mathematical terms, it can be shown as:

$$y_f = \frac{1}{n} \sum_{x=1}^n y_x \quad (4.3)$$

Where y_f is the final value of the prediction, n is the number of estimators (number of trees) included in the random forest, and y_x is the prediction of the x^{th} tree.

The accuracy of the outcome is checked by root mean square error (RMSE). The mathematical relation used for RMSE is:

$$RMSE = \sqrt{\frac{\sum_{x=1}^n (\text{predicted value}_x - \text{Actual value}_x)^2}{n}} \quad (4.4)$$

4.2 Summary

In this chapter, complete Random Forest Regression and the maximum power point tracking algorithm based on it are discussed. The dataset used for RFR – MPPT is obtained for the drift-diffusion modeling of a three-layered perovskite solar cell. All the data i.e., the forward and reverse scan voltages, currents, and powers was loaded from the .mat file created after the modeling of the perovskite solar cell. Voltages and currents were declared as features, and power was used as the target variable. The number of estimators was set to 100 and fixed the random states to 42. The RFR-MPPT averaged the prediction of all individual trees in the forest. The root mean squared error is used as the criterion for checking the best split of random forest regression.

CHAPTER 5: RESULTS AND DISCUSSION

The results, for studying the scan rate and direction's effect on the J-V characteristics of PSC having a three-layered structure as shown in figure 3.1, are obtained by using the well-developed environment on MATLAB, named IonMonger, by [91], [95]. Initially, the model parameters that were used to study the hysteresis effect on PSC are shown in Table 3.1. At different scan rates and sweep directions, the performance of PSC is studied and analyzed. Then the developed MPPT technique was implemented under every scan rate scenario so that it can predict the maximum power and compare it with other MPPTs.

After this, the values of bulk recombination, and the ETL and HTL's doping densities were optimized respectively to analyze the changing behavior of PSC and its associated J-V curves under different scan rates and directions. It is the accepted cause mentioned in the literature related to PSCs that recombination and ion migrations are responsible for this unusual hysteresis in PSCs.

To start the process, the PSC was preconditioned for 5s before the voltage was scanned from 1.2V to 1V (Reverse scanning) and back to 1.2V (Forward scanning). Allowing the simulation to start at a steady-state initial voltage during the preconditioning procedure prevents transient behavior or hysteresis from impacting the simulation in its early stages. As a result, the simulation results could be more precise and reliable. Preconditioning can also ensure that the simulation starts with a known initial condition, which is useful for comparing and assessing the results of several simulations. All the experiments are conducted on the same standard testing condition (STC) irradiance and temperature i.e., 1000 W/m^2 and 25°C . The constant line, shown in Figure 5.1, at 1 displays the irradiance equivalent to STC irradiance.

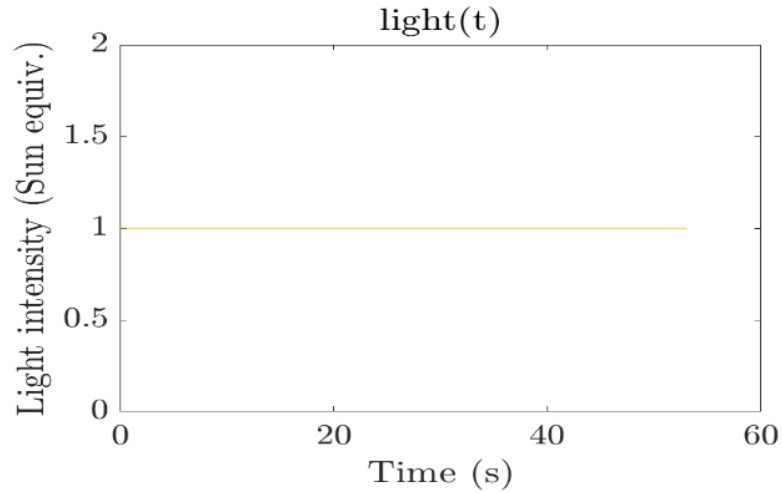


Figure 5. 1: Light Intensity (Irradiance)

5.1 Impact of Scan Rate on J – V Hysteresis

Hysteresis occurs at a wide range of scan rates. Ion vacancy migration is quick enough to allow for modest changes in the applied potential while keeping the distribution of ion vacancy near quasi-equilibrium at low scan rates. As a result, the measured current is solely determined by the applied voltage $V(t)$ and is mostly unaffected by the direction of the scan. At high and moderate scan rates, the scan rate has a significant impact on the measured current and internal electric fields, as well as the distribution of ion vacancies. Due to this, the hysteresis is likely to occur in J-V, with currents measured on the reverse scan (at the same voltage) deviating dramatically from forward scan currents.

The results obtained by using the model parameters mentioned in Table 3.1, at different scan rates are shown in Table 5.1.

Table 5. 1: Impact of Scan Rate on Hysteresis Before Changing Input Parameters

| ScanRate (mV/s) | 50 | | 100 | | 150 | | 200 | |
|--------------------|-----------|-----------|-----------|-----------|-----------|-----------|-----------|-----------|
| | <i>FS</i> | <i>RS</i> | <i>FS</i> | <i>RS</i> | <i>FS</i> | <i>RS</i> | <i>FS</i> | <i>RS</i> |
| Voc (V) | 1.0329 | 1.0844 | 1.0128 | 1.0816 | 0.99501 | 1.0805 | 0.96758 | 1.08 |
| Jsc | 22.119 | 22.1648 | 22.1979 | 22.2232 | 22.2526 | 22.2639 | 22.2812 | 22.2855 |

| | | | | | | | | |
|--|---------|---------|---------|---------|---------|---------|---------|---------|
| (mA/cm²) | | | | | | | | |
| V_{max} (V) | 0.888 | 0.984 | 0.816 | 0.984 | 0.708 | 0.984 | 0.588 | 0.984 |
| J_{max} (mA/cm²) | 19.6964 | 21.4132 | 17.7515 | 21.3864 | 16.0236 | 21.371 | 15.2378 | 21.3617 |
| FF (%) | 76.5545 | 87.6656 | 64.4318 | 87.5535 | 51.2372 | 87.4131 | 41.5599 | 87.3333 |
| PCE (%) | 17.4904 | 21.0706 | 14.4852 | 21.0443 | 11.3447 | 21.029 | 8.9598 | 21.0199 |
| HI | 0.16991 | | 0.31168 | | 0.46052 | | 0.57375 | |

5.1.1 At the Scan Rate of 50mV/s

At a 50mV/s scan rate, figure 5.2 shows the graphical representation of the results obtained. As discussed earlier the applied voltage is preconditioned for 5s, shown in Figure 5.2 (a), so that if there is any uncertainty or transient already present before the system runs, it could be settled down. The voltage was then swept from 1.2V to 0, for the reverse scan, and then back to 1.2V, for the forward scan. The V_{OC} , J_{SC} , FF, PCE, and the corresponding hysteresis index in reverse and forward scans, are shown in Figure 5.2, and Table 5.1 demonstrates the graphical representation of the performance of PSC at 50mV/s. The main and accepted reasons for hysteresis occurrence, unanimously as discussed in the previous section and also in the literature, are the recombination rate and doping levels. The losses that occurred by the interfacial recombination can be depicted in Figure 5.2 (b). The hysteresis index is evaluated using the following mathematical expression:

$$HI = \frac{RS_{PCE} - FS_{PCE}}{RS_{PCE}} \quad (5.1)$$

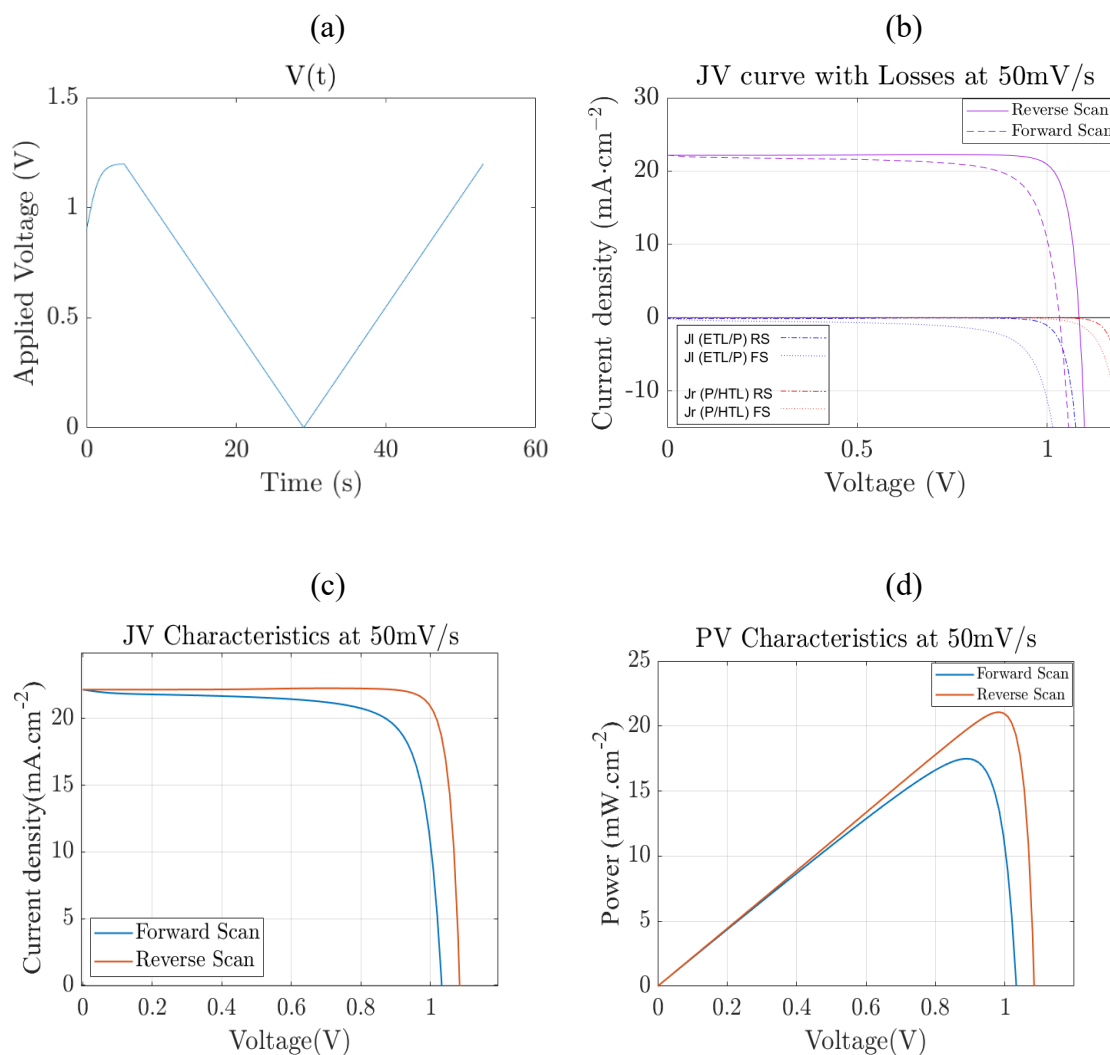


Figure 5. 2: Graphical Representation of Hysteresis at a Scan Rate of 50mV/s. (a) Applied Voltage is displayed with respect to time taken for the complete process. (b) J-V characteristic curve with the current-density Losses due to Interfacial Losses. (c) J-V characteristic curve showing the hysteresis content present. (d) Hysteresis content showing in PV curve.

5.1.2 At the Scan Rate of 100mV/s

The period for the applied voltage at the 100 mV/s scan rate (Figure 5.3 (a)) reduced to almost half from the case of 50mV/s. Figure 5.3 and Table 5.1 illustrate that the hysteresis level is increased from 0.16991 to 0.31168. The change in performance parameters is also depicted in Table 5.1. The values for V_{OC} , FF, and PCE reduced

significantly. This happened due to the increase in the transport layer losses like the current density loss J_l in the ETL/Perovskite layer and current density loss J_r in the Perovskite/HTL layer, shown in figure (b).

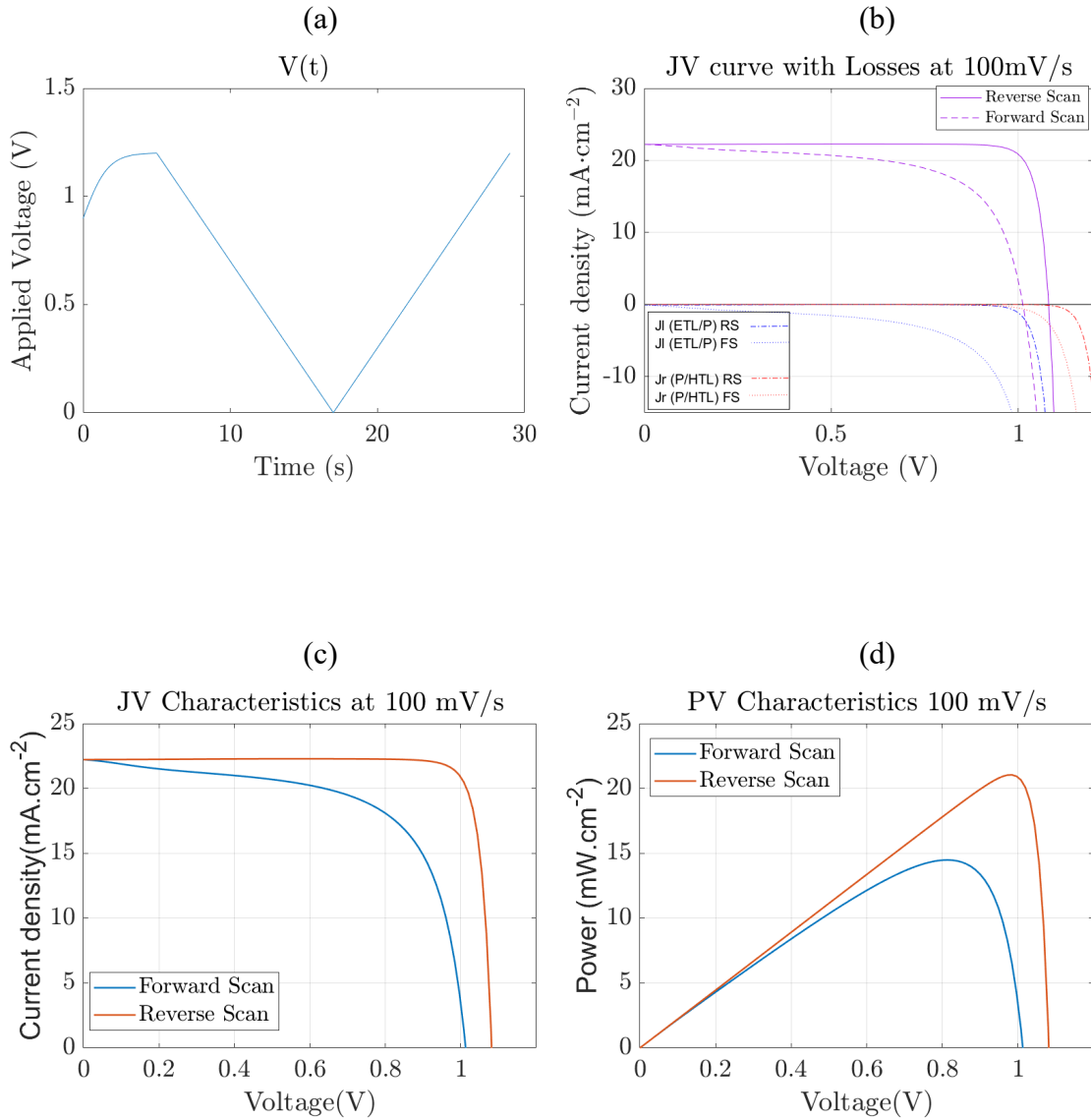


Figure 5. 3: Graphical Representation of Hysteresis at a Scan Rate of 100mV/s. (a) Applied Voltage is displayed with respect to time taken for the complete process. (b) J-V characteristic curve with the current-density Losses due to Interfacial Losses. (c) J-V characteristic curve showing the hysteresis content present. (d) Hysteresis content showing in PV curve.

5.1.3 At the Scan Rate of 150mV/s

Now, at 150mV/s scan rate, the period for applied voltage is further reduced concerning previous cases, and in turn, the losses increase further due to the interfacial recombination and charge transport.

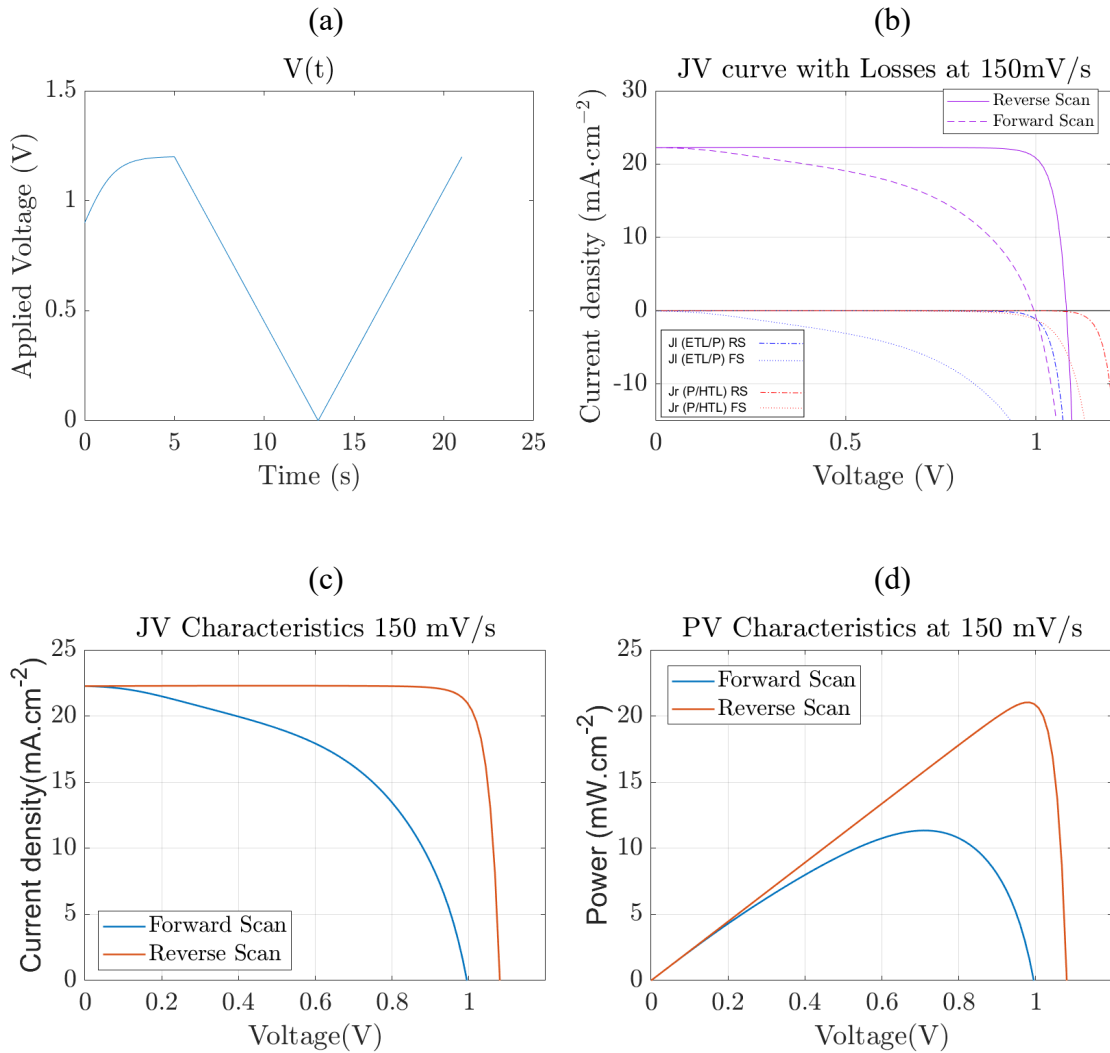
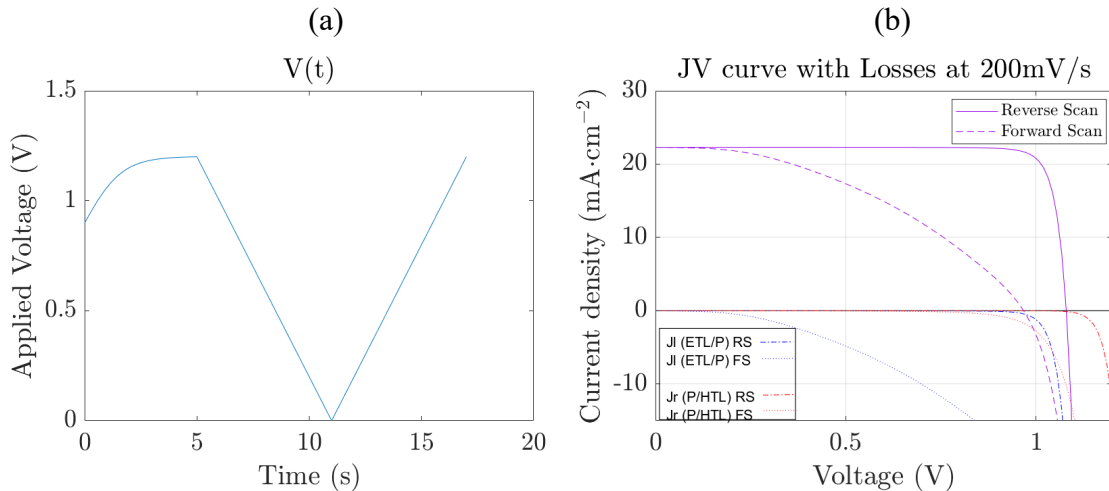


Figure 5. 4: Graphical Representation of Hysteresis at a Scan Rate of 150mV/s. (a) Applied Voltage is displayed with respect to time taken for the complete process. (b) J-V characteristic curve with the current-density Losses due to Interfacial Losses. (c) J-V characteristic curve showing the hysteresis content present. (d) Hysteresis content showing in PV curve.

This rapid change in applied voltage, and the scan rate impacted the ion vacancy distribution, internal electric field, and ultimately the current densities. This led to noticeable JV hysteresis having a difference between the current density of the reverse scan from the current density of the forward. Table 5.1 and Figure 5.4 show this difference in the form of performance parameter values and graphical representation. The hysteresis index jumped to 0.46052 which is quite high and showed the reduced performance of PSC.

5.1.4 At the Scan Rate of 200mV/s

Similarly, the trend followed from the previous cases that as the scan rate increased to 200mV/s, the applied voltage changed rapidly i.e., the period, for voltage sweep from open circuit to short circuit and then back to open circuit, is reduced which, in turn, lead to increase the interfacial recombination's losses. The hysteresis noticed in this case jumped to 0.57375 and the worst performance is depicted in Table 5.1 and Figure 5.5.



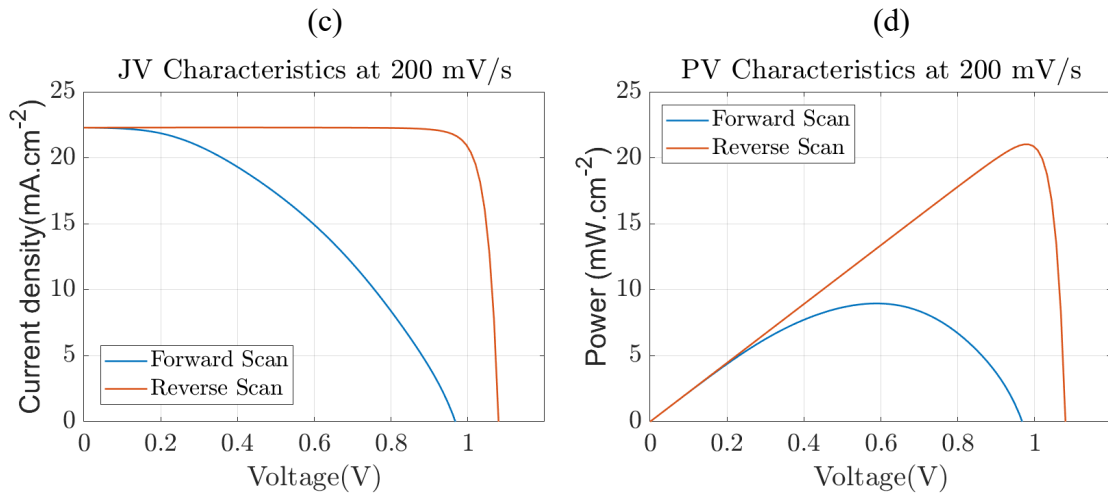


Figure 5. 5: Graphical Representation of Hysteresis at a Scan Rate of 200mV/s. (a) Applied Voltage is displayed with respect to time taken for the complete process. (b) J-V characteristic curve with the current-density Losses due to Interfacial Losses. (c) J-V characteristic curve showing the hysteresis content present. (d) Hysteresis content showing in PV curve.

It is evident from the mentioned results in figures 5.2 to 5.5, and Table 5.1 that at low scan rates, applied potential changed slowly due to which the distribution of ion vacancy remained near to equilibrium and in turn, measured current densities, forward and reverse, showed less-to-minimum difference between them. This means that at a low scan rate, the current density is less dependent on the scan rate and more dependent on the applied voltage – $V(t)$. However, the J-V curve showed noticeable hysteresis in the current densities of forward and reverse scans at high scan rates. The ion vacancy distribution is impacted by high scan rates and ultimately, the performance of PSC is reduced.

So, it is clear that the JV hysteresis level is dependent on the charge carrier recombination which is affected by the voltage distribution due to a change in ion vacancy distribution.

5.1.5 Impact of Parameter's Changing on $J - V$ Hysteresis

The following input parameters are adjusted to study and analyze the impact of doping levels (in transport layers), ion vacancy, and recombination on J-V hysteresis.

Table 5. 2: Optimization of PSC's Parameters

| Parameter | Previous Value | Tuned Value |
|--|----------------------|----------------------|
| Ion Vacancy Diffusion Coefficient ($\text{m}^2.\text{s}^{-1}$) | 6.5×10^{-8} | 10×10^{-17} |
| ETL's Effective Doping Density (m^{-3}) | 1×10^{24} | 2×10^{24} |
| HTL's Effective Doping Density (m^{-3}) | 1×10^{24} | 2×10^{24} |
| Hole Recombination Velocity for SRH (ms^{-1}) | 10 | 1 |
| Electron Recombination Velocity for SRH (ms^{-1}) | 0.1 | 0.01 |

Ion vacancy diffusion coefficient in PSC has an impactful role which highlights the transport properties in PSC. Ion vacancy or defect is represented by this coefficient. Hysteresis in the J-V curve is highly influenced by it. Doping densities in HTL and ETL are also important factors in PSCs and have a noticeable effect on the hysteresis of J-V. Interfacial recombination, as discussed in previous sections, is also an important parameter in evaluating and analyzing hysteresis.

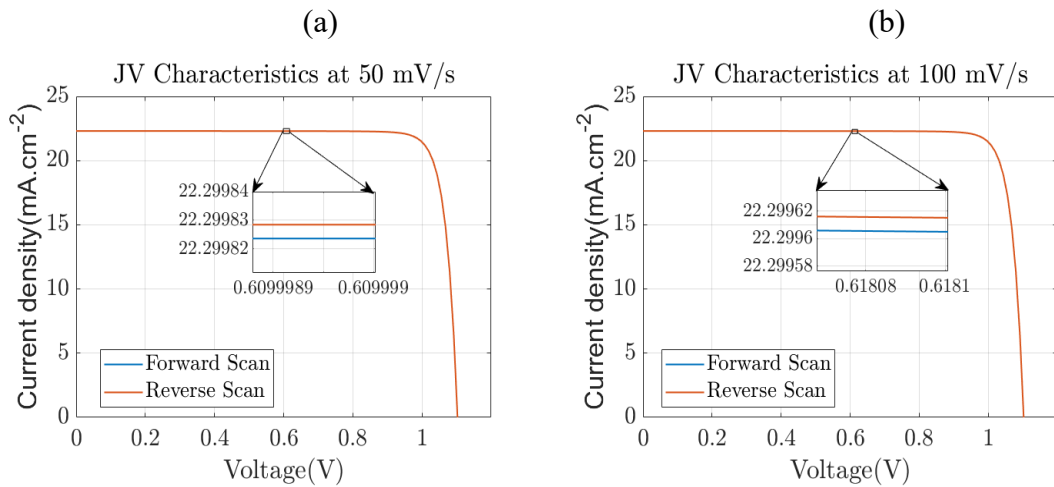
Table 5.3 and Figure 5.6 show the outputs and responses after changing the parameters, as shown in Table 5.2. At the high ion vacancy diffusion coefficient's value, the power conversion efficiency reduced a lot and ultimately the hysteresis level increased a lot. So, its value is reduced stepwise to $10 \times 10^{-17} \text{ m}^2.\text{s}^{-1}$ which improved the results and reduced the hysteresis. Similarly, at low doping densities of ETL and HTL, it was noticed that the PCE reduced, hence, its value was tuned to $2 \times 10^{24} \text{ m}^{-3}$ which also reduced the hysteresis. Doping densities ensure the electric field, and device performance is highly dependent on it so there is still much room for improvement in it. One of the key reasons for hysteresis in PSC is the interfacial recombination and it is almost accepted by everyone in literature and the field working on PSCs. It is a phenomenon of electron-hole recombination in semiconductor physics, known as carrier recombination. Shockley Red Hall recombination is the phenomenon in which the electrons or holes recombine with the carriers of the same energy and ultimately destroy it. At low velocities, this recombination reduces, increasing the performance of PSC. This is the reason, the velocity of electron

recombination is reduced to 0.01 ms^{-1} , reducing the hysteresis and improving the performance.

Collectively, five parameters are mentioned above that have a very dominant impact on the hysteresis of the J-V curve that negligible Hysteresis Index is noted, which is depicted in table 5.3 and figure 5.6.

Table 5. 3: Results obtained after changing PSC's Input Parameters

| Scan Rate (mV/s) | 50 | | 100 | | 150 | | 200 | |
|-------------------------------------|------------|-----------|------------|-----------|------------|-----------|------------|-----------|
| | <i>FS</i> | <i>RS</i> | <i>FS</i> | <i>RS</i> | <i>FS</i> | <i>RS</i> | <i>FS</i> | <i>RS</i> |
| Voc (V) | 1.1027 | 1.1027 | 1.1027 | 1.1027 | 1.1027 | 1.1027 | 1.1027 | 1.1027 |
| Jsc (mA/cm²) | 22.304 | 22.304 | 22.304 | 22.304 | 22.304 | 22.304 | 22.304 | 22.304 |
| Vmax(V) | 0.996 | 0.996 | 0.996 | 0.996 | 0.996 | 0.996 | 0.996 | 0.996 |
| Jmax (mA/cm²) | 21.547 | 21.547 | 21.547 | 21.547 | 21.547 | 21.547 | 21.547 | 21.547 |
| FF (%) | 87.261 | 87.261 | 87.261 | 87.261 | 87.261 | 87.261 | 87.261 | 87.261 |
| PCE (%) | 21.461 | 21.461 | 21.461 | 21.461 | 21.461 | 21.461 | 21.461 | 21.461 |
| HI | 2.8424e-07 | | 4.9736e-07 | | 6.7369e-07 | | 9.5932e-07 | |



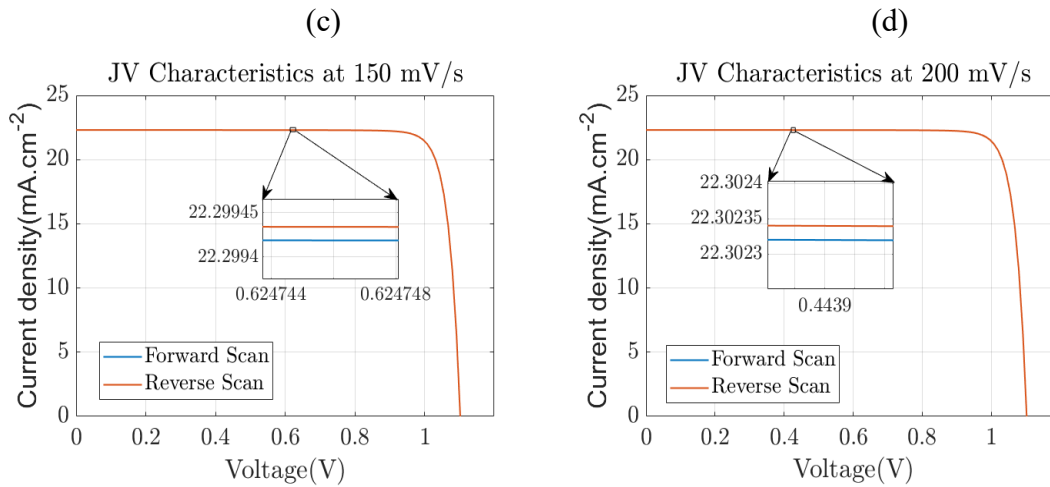


Figure 5. 6: Results obtained after changing the PSC's Parameters that lead to minimum hysteresis at each Scan Rate

An important thing noticed here is that after changing the parameter values, the impact of the scan rate became negligible. As the J-V hysteresis became very low, increasing the scan rate to high values did not impact the performance of PSC. This evaluation is depicted in Table 5.3.

5.2 Prediction of MPP and Extraction of Maximum Power

Algorithms of MPPT are very significant in maximum power extraction from solar cells. The operating points of photovoltaics are optimized by MPPTs so that the PV array can produce power at its maximum capacity under changing conditions. The MPPT algorithm works in such a way that it initially measures the current and voltage of the solar photovoltaic under the system's inputs, calculates power, and then adjusts its parameters like voltage to check where it is getting the maximum power. After finding the maximum power, it locks the MPP voltage current and power that allows the PV module to produce power at its maximum efficiency. Under changing conditions, the MPPT also makes sure that the MPP of a system does not change.

Random forest regression (RFR) based MPPT algorithm is developed here to cope with the effects of hysteresis in the plot of J-V. The data of calculated current densities,

voltages, and calculated powers for both reverse and forward scans were utilized as input to the RFR-MPPT. The reverse and forward scan data are concatenated into a single data variable of voltage, a single data variable of currents, and a single data variable of powers. Voltages and currents were considered as features and powers as targets. The data was then split into training and testing data. The random seed of reproducibility was set to 42 so that the environment's sequence remained the same during the whole process. 80% data was declared for training and 20% data was declared for testing. The RFR was then built and trained in which the number of estimators (number of trees) was selected as 100. The prediction of each tree was made by the RFR and then took an average of all the predictions to get the final prediction of MPP i.e., voltage and current at MPP. The accuracy of the algorithm was checked using root mean square error.

The RFR-MPPT was evaluated under two cases;

1. Under the hysteresis of J-V at different scan rates (section 5.1.1 to 5.1.4)
2. Under reduced hysteresis of J-V at different scan rates (section 5.1.5)

5.2.1 *Extraction of Maximum Power under J – V Hysteresis*

The maximum power point values, i.e., MPP voltage, current, and power, obtained by implementing RFR-MPPT are shown in Table 5.4 and the respective J-V curves are shown in Figure 5.7. It is observed that even when the hysteresis level increases, the RFR-MPPT predicted the maximum power point accurately and preserved it. There is a negligible difference of 0.01mW/cm² or 0.047% change per 50mV/s increase in scan rate.

Table 5. 4: Prediction of Maximum Power Point Values by implementation of RFR-MPPT under Noticeable Hysteresis

| Scan Rate (mV/s) | 50 | 100 | 150 | 200 |
|--|-----------|------------|------------|------------|
| V_{mpp} (V) | 0.97 | 0.97 | 0.97 | 0.97 |
| J_{mpp} (mA/cm²) | 21.64 | 21.63 | 21.62 | 21.62 |

| | | | | |
|--------------------------------|----------|-----------|-----------|-----------|
| Pmpp(mW/cm²) | 21.04 | 21.03 | 21.02 | 21.01 |
| RMSE | 6.547486 | 22.537564 | 35.212822 | 41.882379 |

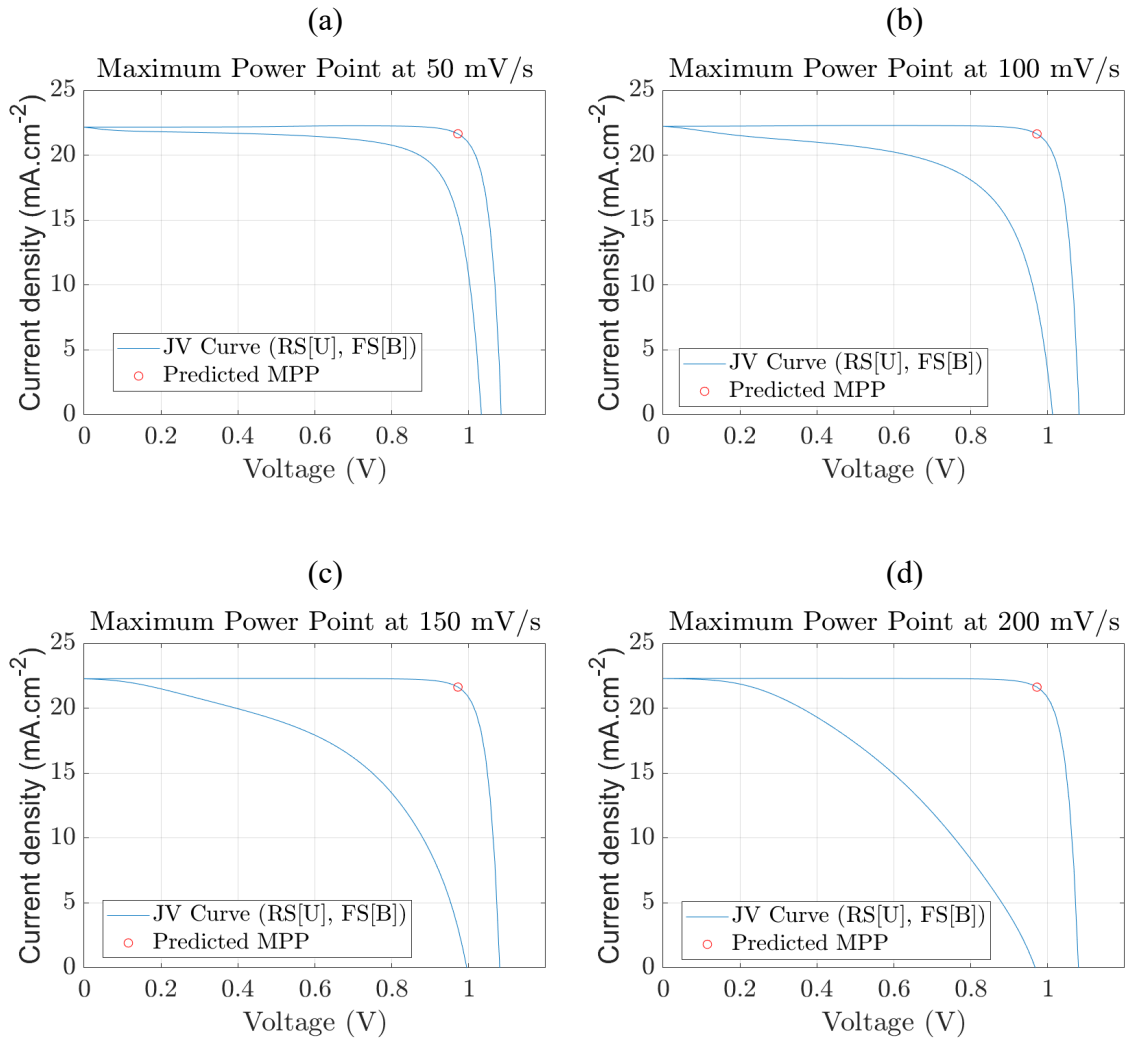


Figure 5. 7: RFR-MPPT's Prediction and Tracking of Maximum Power Point, under hysteresis, shown in red circle on the J-V curves at Scan Rate (a) 50mV/s (b) 100mV/s (c) 150mV/s (d) 200mV/s. 'U' means 'upper line showing Reverse Scan', 'B' denoting 'Bottom line showing Forward Scan'.

It is evident by analyzing Table 5.4 and Table 5.1 that RFR-MPPT did not overestimate the performance of the system and predicted the true performance parameters of the system even under the immense hysteresis. As the scan rate increased, the root mean

square error also increased due to the increased hysteresis but the RFR-MPPT did not underestimate or overestimate the PSC's performance and predicted and preserved the best maximum power point.

5.2.2 *Extraction of Maximum Power under Negligible J – V Hysteresis*

The RFR-MPPT is also implemented on the data obtained after the changing in input parameters to reduce J-V hysteresis to as minimum as possible (shown in section 5.1.5) so that the performance of MPPT can be verified. It is concluded from Table 5.5 and Figure 5.8, and by comparing these results with the results shown and displayed in Table 5.4 and Figure 5.7 that the RFR-MPPT predicted the true MPP. When there is minimum hysteresis in the J-V curves of PSC under different scan rates, the MPP values are almost the same in comparison to the MPP values when there is noticeable J-V hysteresis with a difference of 0.42mW/cm² or 1.9% in MPP power. This slight difference is due to the hysteresis level difference in both cases and this difference is also evident from the RMSE. However, the RFR-MPPT did not underestimate or overestimate the PSC's performance.

Table 5. 5: Prediction of Maximum Power Point by implementation of RFR-MPPT Values under Minimum Hysteresis

| ScanRate(mV/s) | 50 | 100 | 150 | 200 |
|--|-----------|------------|------------|------------|
| V_{mpp} (V) | 1.00 | 1.00 | 1.00 | 1.00 |
| J_{mpp} (mA/cm²) | 21.55 | 21.55 | 21.55 | 21.55 |
| P_{mpp}(mW/cm²) | 21.46 | 21.46 | 21.46 | 21.46 |
| RMSE | 0.191078 | 0.341024 | 0.530100 | 0.530668 |

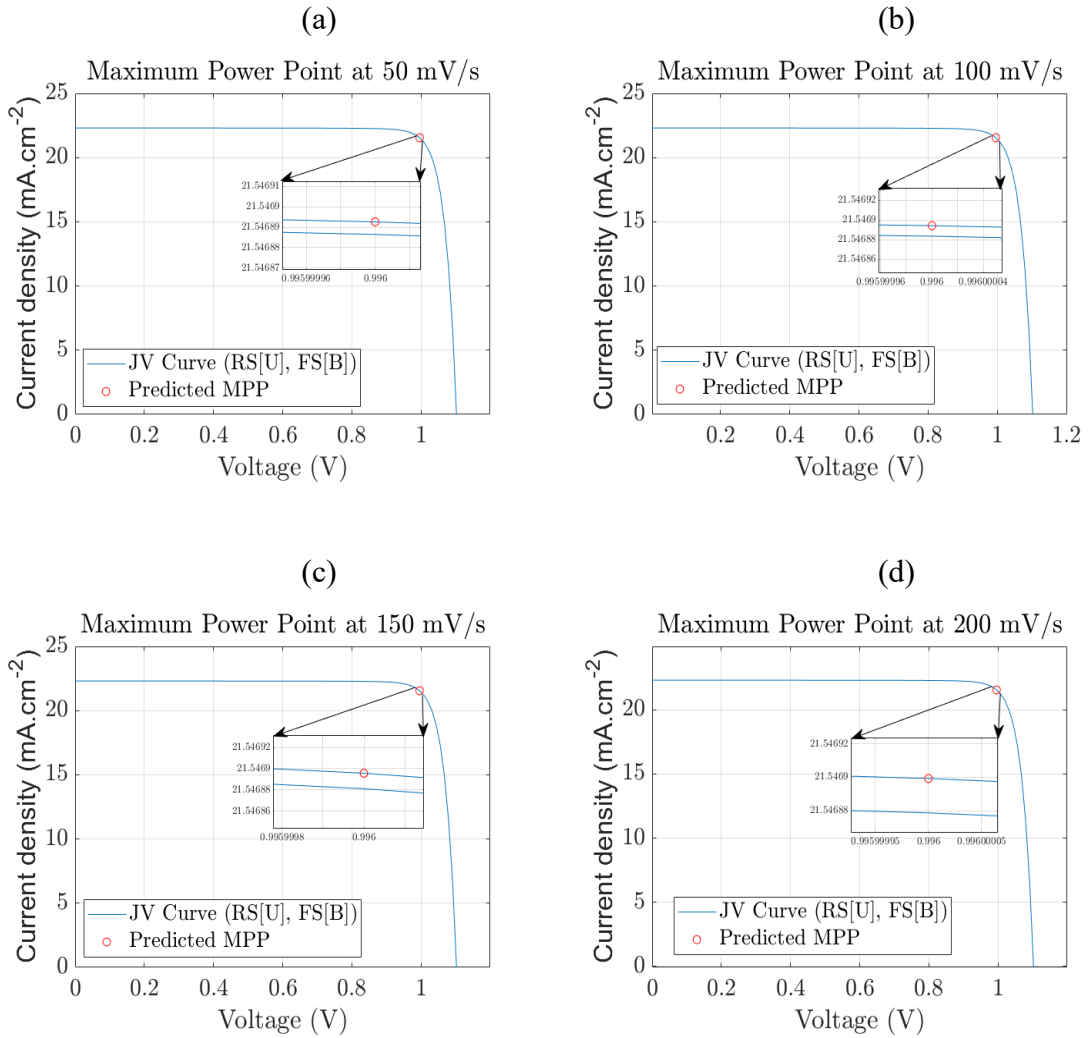


Figure 5. 8: RFR-MPPT's Prediction and Tracking of Maximum Power Point, under hysteresis, shown in red circle on the J-V curves at Scan Rate (a) 50mV/s (b) 100mV/s (c) 150mV/s (d) 200mV/s. 'U' means 'upper line showing Reverse Scan', 'B' denoting 'Bottom line showing Forward Scan'.

5.3 Comparison of RFR – MPPT with Conventional MPPTs

Many MPPTs are developed in the literature for finding the maximum power point of different 1st and 2nd generation solar cells, in which the popular ones are;

1. Perturb & Observe
2. Incremental Conductance

The comparison of RFR-MPPT with these already developed techniques is discussed below so that the compatibility of RFR-MPPT for PSCs can be checked and verified.

5.3.1 P&O – Perturb and Observe

As discussed in section 2.7.1, the P&O technique simply adds perturbations to the voltage while tracking the maximum power point. Its major advantage is its simple methodology.

The results obtained by implementing this technique on PSC are mentioned in Table 5.6 and displayed in Figure 5.9. Under hysteresis, it is evident that it overestimated the performance of PSC and did not track the maximum power point accurately. If these results of P&O are compared with RFR-MPPT, Table 5.4 and Figure 5.7, the RFR-MPPT algorithm worked very well and predicted the MPP accurately. As the scan rate increased, the P&O further shifted the MPP out of the J-V curve. So, this method of tracking the MPP cannot be used for PSCs as there is a problem with J-V curve hysteresis in PSCs. Once the J-V curve hysteresis is removed by some methodology, this technique can be useful in determining the MPP of PSCs too.

Table 5. 6: MPP Tracking by Implementing P&O Algorithm under Noticeable Hysteresis

| Scan Rate (mV/s) | 50 | 100 | 150 | 200 |
|--|-----------|------------|------------|------------|
| V_{mpp} (V) | 0.9890 | 0.9940 | 0.9990 | 1.0040 |
| J_{mpp} (mA/cm²) | 21.4132 | 21.3864 | 21.3710 | 21.3617 |
| P_{mpp} (mW/cm²) | 21.177 | 21.258 | 21.349 | 21.447 |

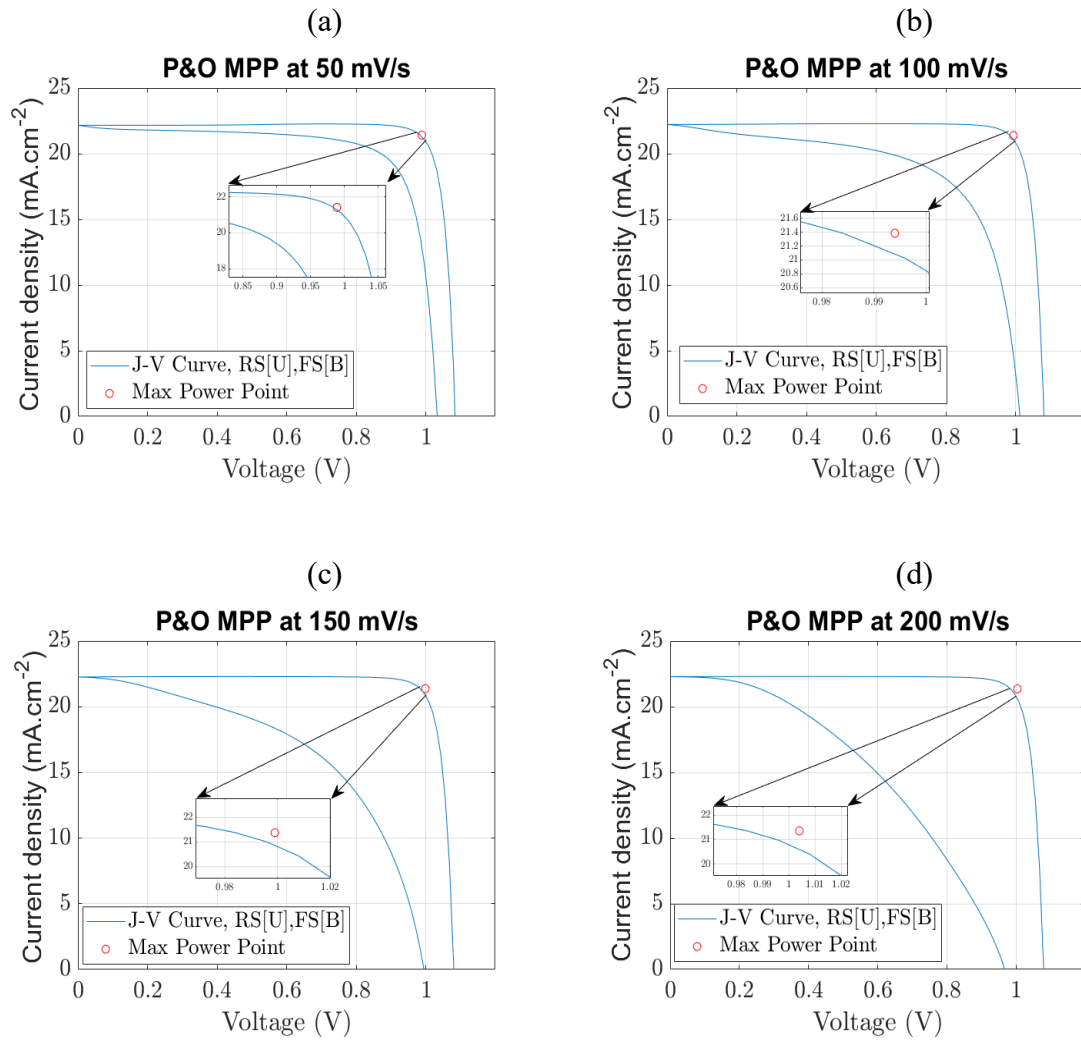


Figure 5. 9: MPP Tracking by P&O under Noticeable Hysteresis at Scan Rate (a) 50mV/s (b) 100mV/s (c) 150mV/s (d) 200mV/s.

5.3.2 IC – Incremental Conductance

Incremental conductance MPPT works by adjusting the duty cycle to find the MPP of solar cells. But it has many limitations like it cannot track the MPP when there is noise, ripple, or hysteresis present in the J-V or P-V curves. This is why, this technique badly failed in tracking the MPP of PSC here. It is evident from the results shown in Table 5.7 and Figure 5.10 that the IC tracked the MPP inaccurately. Hence this technique can never be used, solely, for tracking maximum power from PSCs.

Table 5. 7: MPP Tracking by Implementing IC Algorithm under Noticeable Hysteresis

| Scan Rate (mV/s) | 50 | 100 | 150 | 200 |
|--|---------|---------|---------|---------|
| V_{mpp} (V) | 0.5520 | 0.3000 | 0.0960 | 0.0120 |
| J_{mpp} (mA/cm²) | 22.2273 | 22.2578 | 22.2719 | 22.2855 |
| P_{mpp}(mW/cm²) | 11.6023 | 6.6774 | 2.138 | 0.2674 |

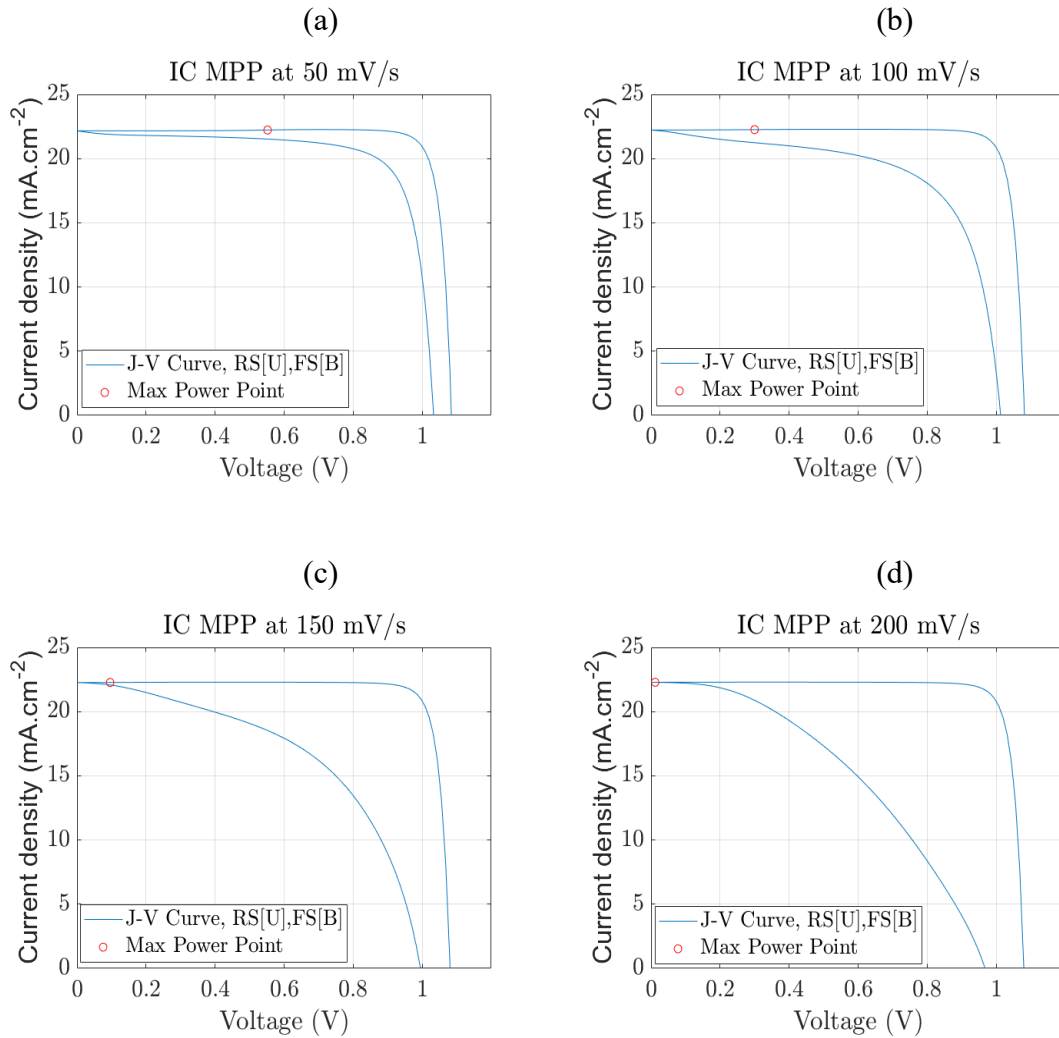


Figure 5. 10: MPP Tracking by IC under Noticeable Hysteresis at Scan Rate (a) 50mV/s (b) 100mV/s (c) 150mV/s (d) 200mV/s.

5.4 Summary

In this chapter, J-V hysteresis impacted by scan rate is discussed, with results in detail. J-V hysteresis increases as the scan rate increases because of doping densities and interfacial recombination. The hysteresis index is used for evaluating these hysteresis contents in the plots of J-V. When doping densities of ETL and HTL, ion vacancy diffusion coefficient, and interfacial recombination values were tuned and optimized, the hysteresis level in J-V curves reduced to a minimum level that the impact of scan rate became negligible. But practically, it will be very difficult to build a PSC with such accuracy that it can optimize the parameters as optimized in this work while simulation of a three-layered PSC. This was done to check how much a hysteresis level can be reduced by tuning the above parameters. This optimization also helped in determining the performance of a novel RFR-MPPT algorithm. More intensive research is required to optimize the parameters, practically, to get rid of this anomalous hysteresis.

The RFR-MPPT algorithm is developed to track the true MPP parameters of a three-layered PSC under the influence of immense hysteresis in the plot of J-V at different scan rates. It is observed from the results mentioned and discussed in this chapter that the RFR-MPPT predicted the MPP accurately irrespective of the hysteresis level. The RMSE was increased a little bit by increasing the scan rate and hysteresis level. However, the novel algorithm developed in this work performed accurately and did not disturb the predicted MPP. The predicted MPP values are almost the same when there was noticeable hysteresis and when the hysteresis was reduced to the minimum. RFR-MPPT also performed marvelously well when compared to the highly adopted MPPT algorithms in the solar industry i.e., Incremental Conductance, and Perturb and Observe.

CHAPTER 6: CONCLUSION AND RECOMMENDATIONS

In this thesis, the impact of scan rates on the hysteresis of J-V curves has been investigated and studied. This has helped to understand the behavior of a three-layered PSC. By increasing the scan rate from 50mV/s to 200mV/s in steps, it was concluded that the period for the applied voltage was reduced at each step means it quickly completed the process. This led to an increase in the losses of current density due to doping densities and interfacial recombination that ultimately increased the level of hysteresis to very high values. Contrary to this, at low scan rates like 50mV/s, the period for applied voltage was sufficient which led to the current density remaining near the equilibrium, hence, the level of hysteresis was low. For this study, IonMonger, a MATLAB environment developed by Courtier et.al in [91], [95], was used that help in understanding the behavior of hysteresis in PSC. Ion vacancy distribution, doping densities, and rates of interfacial recombination are the main causes of this noticeable PSC hysteresis in the plots of J-V. When the values for interfacial recombination rates, and doping densities were tuned and changed, it was noticed that the impact of scan rate became negligible, and the level of hysteresis was reduced to very low values. There was almost no change in the performance parameters of PSCs after this change in parameters, even at high scan rates, there was negligible hysteresis content. Hence, the modeling and operation of a three-layered (ETL, Perovskite, HTL) PSC, and the impact of scan rate and its direction on the performance of PSC were understood by this study. This study also helped in understanding and confirming the basic causes of hysteresis i.e., the interfacial recombination rates and effective doping densities.

To develop a technique or algorithm that should be efficient enough to predict the true MPP of PSCs even under noticeable J-V curve hysteresis was one of the main objectives of this thesis. RFR-MPPT effectively did this and predicted the Maximum Power Point values very efficiently. Under high hysteresis level, the RFR-MPPT did not overestimate and underestimate the performance of the three-layered PSC which is also depicted in the results shown and discussed in the results and discussion sections. A good MPPT does not change the MPP of the solar cell, of a P-V system, at any cost. It is depicted in the results and discussion, for the same level of applied voltage and system

specifications, the RFR-MPPT predicted almost the same MPP under hysteresis and under minimum hysteresis, whatever the scan rate was, with a slight difference of $0.42\text{mW}/\text{cm}^2$ or 1.9% in the MPP power.

RFR-MPPT was also compared with the ‘Perturb & Observe’ and ‘Incremental Conductance’ MPPT algorithms to check their credibility of it. The P&O technique was implemented, in literature, to track the MPP of different PSCs but not under hysteresis. Here, in this thesis, it was concluded that the algorithm of P&O did not predict the MPP accurately. It pointed the MPP out of the plots and overestimated the performance. Increasing the scan rate, further shifted the MPP and the overestimation error increased. This was because the level of hysteresis was increasing.

When the IC algorithm was implemented on the same PSC, it was noticed that the IC technique misjudged and tracked the wrong MPP values. The main reason for this worst output in the case of IC MPPT is that it has many limitations like it cannot track the MPP when there is noise, ripple, or hysteresis present in the J-V or P-V curves. That’s why, this technique badly failed in tracking the MPP of PSC. It is evident from the results shown in Table 4.7 and Figure 4.10 that the IC tracked the MPP inaccurately. Hence this technique can never be used, solely, for tracking maximum power from PSCs.

This comparison has shown that the RFR-MPPT performed very efficiently and effectively in predicting the MPP and extraction of maximum power from PSC.

For future consideration, it is recommended that more intensive research is needed in the reduction of J-V hysteresis as it affects the stability and credibility of the PSC. The ion vacancy migration, interfacial recombination, and effective doping densities were noticed as the main pinpoints in increasing or decreasing the hysteresis level. But it is very difficult to achieve such values. As already a lot of research is proceeding in building more stable and hysteresis-free PSCs, these three main parameters should be considered in developing PSCs. MPPT is the main part of the solar PV industry. RFR-MPPT has performed very well in predicting the MPP and extracting the maximum power. It is recommended to implement this novel MPPT, practically, on developed PSCs. There is room for improvement in the reduction of RMSE, and the 1.9% predicted MPP power

difference, by improving the data, input parameters, and tuning the hyperparameters i.e., estimators of this machine learning network. Predicting the parameters of PSCs using the Random Forest, modeling the PSC, and then implementing RFR-MPPT to check the performance of PSC can be a good topic of research in the future by using this dissertation

REFERENCES

- [1] F. C. Treble and C. Eng, "Solar cells."
- [2] T. Jenkins, "A brief history of ... semiconductors A brief history of... semiconductors," 2005. [Online]. Available: <http://iopscience.iop.org/0031-9120/40/5/002>
- [3] B. W. G A, "On the Action of Light on Selenium. 113 V. 'The Action of Light on Selenium.'" [Online]. Available: <https://royalsocietypublishing.org/>
- [4] S. P. Langley, "The Bolometer and Radiant Energy," 1880.
- [5] S. Sun, Z. Fan, Y. Wang, and J. Haliburton, "PHOTOVOLTAIC MATERIALS AND PHENOMENA SCELL-2004 Organic solar cell optimizations."
- [6] L. O. Grondahl and R. Lsborofory, "The Copper-Cuprous-Oxide RectNer and Photoelectric Cell," 1933.
- [7] E. Tomaszewski, "Jan CzochralskiFfather of the Czochralski method," 2002.
- [8] D. M. Chapin, C. S. Fuller, and G. L. Pearson, "A new silicon p-n junction photocell for converting solar radiation into electrical power [3]," *Journal of Applied Physics*, vol. 25, no. 5. pp. 676–677, 1954. doi: 10.1063/1.1721711.
- [9] D. M. Chapin, C. S. Fuller, and G. L. Pearson, "A New Silicon p-n Junction Photocell for Converting Solar Radiation into Electrical Power," in *WORLD SCIENTIFIC eBooks*, 1991, pp. 969–970. doi: 10.1142/9789814503464_0138.
- [10] E. T. Efaz1 *et al.*, "A review of primary technologies of thin-film solar cells," *Engineering Research Express*, vol. 3, no. 3. IOP Publishing Ltd, Sep. 01, 2021. doi: 10.1088/2631-8695/ac2353.
- [11] W. H. Nguyen, C. D. Bailie, E. L. Unger, and M. D. McGehee, "Enhancing the hole-conductivity of spiro-OMeTAD without oxygen or lithium salts by using spiro

(TFSS)2 in perovskite and dye-sensitized solar cells,” *J Am Chem Soc*, vol. 136, no. 31, pp. 10996–11001, Aug. 2014, doi: 10.1021/ja504539w.

- [12] A. M. Bothwell, J. A. Drayton, and J. R. Sites, “Performance Analysis of 0.4-1.2- μm CdTe Solar Cells,” *IEEE J Photovolt*, vol. 10, no. 1, pp. 259–266, Jan. 2020, doi: 10.1109/JPHOTOV.2019.2947556.
- [13] S. K. Pandey and K. Kumar, “Device modeling, optimization and analysis of CdTe solar cell,” in *2016 IEEE Uttar Pradesh Section International Conference on Electrical, Computer and Electronics Engineering, UPCON 2016*, Institute of Electrical and Electronics Engineers Inc., Apr. 2017, pp. 295–299. doi: 10.1109/UPCON.2016.7894668.
- [14] J. Peng, L. Lu, and H. Yang, “Review on life cycle assessment of energy payback and greenhouse gas emission of solar photovoltaic systems,” *Renewable and Sustainable Energy Reviews*, vol. 19. Elsevier Ltd, pp. 255–274, 2013. doi: 10.1016/j.rser.2012.11.035.
- [15] V. Fthenakis, C. Athias, A. Blumenthal, A. Kulur, J. Magliozzo, and D. Ng, “Sustainability evaluation of CdTe PV: An update,” *Renewable and Sustainable Energy Reviews*, vol. 123. Elsevier Ltd, May 01, 2020. doi: 10.1016/j.rser.2020.109776.
- [16] B. K. Ghosh, I. Saad, K. T. K. Teo, and S. K. Ghosh, “mcSi and CdTe solar photovoltaic challenges: Pathways to progress,” *Optik*, vol. 206. Elsevier GmbH, Mar. 01, 2020. doi: 10.1016/j.ijleo.2020.164278.
- [17] F. Ise and P. Projects GmbH, “Photovoltaics Report.” [Online]. Available: www.ise.fraunhofer.de
- [18] A. Mohammad Bagher, “Types of Solar Cells and Application,” *American Journal of Optics and Photonics*, vol. 3, no. 5, p. 94, 2015, doi: 10.11648/j.ajop.20150305.17.

- [19] A. Bosio, G. Rosa, and N. Romeo, "Past, present and future of the thin film CdTe/CdS solar cells," *Solar Energy*, pp. 31–43, Nov. 2018, doi: 10.1016/j.solener.2018.01.018.
- [20] O. Nwakanma, S. Velumani, and A. Morales-Acevedo, "Review on the effects due to alkali metals on copper–indium–gallium–selenide solar cells," *Materials Today Energy*, vol. 20. Elsevier Ltd, Jun. 01, 2021. doi: 10.1016/j.mtener.2020.100617.
- [21] F. W. Liu *et al.*, "High-yield recycling and recovery of copper, indium, and gallium from waste copper indium gallium selenide thin-film solar panels," *Solar Energy Materials and Solar Cells*, vol. 241, Jul. 2022, doi: 10.1016/j.solmat.2022.111691.
- [22] G. S. Selopal, H. Zhao, Z. M. Wang, and F. Rosei, "Core/Shell Quantum Dots Solar Cells," *Adv Funct Mater*, vol. 30, no. 13, Mar. 2020, doi: 10.1002/adfm.201908762.
- [23] Q. Zhao *et al.*, "High efficiency perovskite quantum dot solar cells with charge separating heterostructure," *Nat Commun*, vol. 10, no. 1, Dec. 2019, doi: 10.1038/s41467-019-10856-z.
- [24] E. H. Sargent, "Infrared quantum dots," *Advanced Materials*, vol. 17, no. 5, pp. 515–522, Mar. 2005, doi: 10.1002/adma.200401552.
- [25] J. Yuan *et al.*, "Metal Halide Perovskites in Quantum Dot Solar Cells: Progress and Prospects," *Joule*, vol. 4, no. 6. Cell Press, pp. 1160–1185, Jun. 17, 2020. doi: 10.1016/j.joule.2020.04.006.
- [26] A. H. Ip *et al.*, "Hybrid passivated colloidal quantum dot solids," *Nat Nanotechnol*, vol. 7, no. 9, pp. 577–582, 2012, doi: 10.1038/nnano.2012.127.
- [27] A. H. Ip *et al.*, "Hybrid passivated colloidal quantum dot solids," *Nat Nanotechnol*, vol. 7, no. 9, pp. 577–582, 2012, doi: 10.1038/nnano.2012.127.
- [28] H. A. Maddah, V. Berry, and S. K. Behura, "Biomolecular photosensitizers for dye-sensitized solar cells: Recent developments and critical insights," *Renewable and*

Sustainable Energy Reviews, vol. 121. Elsevier Ltd, Apr. 01, 2020. doi: 10.1016/j.rser.2019.109678.

- [29] A. Mohammad Bagher, “Types of Solar Cells and Application,” *American Journal of Optics and Photonics*, vol. 3, no. 5, p. 94, 2015, doi: 10.11648/j.ajop.20150305.17.
- [30] D. H. Kang and N. G. Park, “On the Current–Voltage Hysteresis in Perovskite Solar Cells: Dependence on Perovskite Composition and Methods to Remove Hysteresis,” *Advanced Materials*, vol. 31, no. 34. Wiley-VCH Verlag, Aug. 01, 2019. doi: 10.1002/adma.201805214.
- [31] P. Liu, W. Wang, S. Liu, H. Yang, and Z. Shao, “Fundamental Understanding of Photocurrent Hysteresis in Perovskite Solar Cells,” *Adv Energy Mater*, vol. 9, no. 13, pp. 1–33, 2019, doi: 10.1002/aenm.201803017.
- [32] H. J. Snaith, “Perovskites: The emergence of a new era for low-cost, high-efficiency solar cells,” *Journal of Physical Chemistry Letters*, vol. 4, no. 21. pp. 3623–3630, Nov. 07, 2013. doi: 10.1021/jz4020162.
- [33] Z. He, C. Zhong, S. Su, M. Xu, H. Wu, and Y. Cao, “Enhanced power-conversion efficiency in polymer solar cells using an inverted device structure,” *Nat Photonics*, vol. 6, no. 9, pp. 591–595, Sep. 2012, doi: 10.1038/nphoton.2012.190.
- [34] L. Zhao *et al.*, “High-Performance Inverted Planar Heterojunction Perovskite Solar Cells Based on Lead Acetate Precursor with Efficiency Exceeding 18%,” *Adv Funct Mater*, vol. 26, no. 20, pp. 3508–3514, May 2016, doi: 10.1002/adfm.201601175.
- [35] H. S. Kim, S. H. Im, and N. G. Park, “Organolead halide perovskite: New horizons in solar cell research,” *Journal of Physical Chemistry C*, vol. 118, no. 11, pp. 5615–5625, Mar. 2014, doi: 10.1021/jp409025w.
- [36] A. Marchioro *et al.*, “Unravelling the mechanism of photoinduced charge transfer processes in lead iodide perovskite solar cells,” *Nat Photonics*, vol. 8, no. 3, pp. 250–255, Mar. 2014, doi: 10.1038/nphoton.2013.374.

- [37] N. G. Park, "Perovskite solar cells: An emerging photovoltaic technology," *Materials Today*, vol. 18, no. 2. Elsevier B.V., pp. 65–72, Mar. 01, 2015. doi: 10.1016/j.mattod.2014.07.007.
- [38] C. Li, K. C. K. Soh, and P. Wu, "Formability of ABO₃ perovskites," *J Alloys Compd*, vol. 372, no. 1–2, pp. 40–48, Jun. 2004, doi: 10.1016/j.jallcom.2003.10.017.
- [39] C. Li, X. Lu, W. Ding, L. Feng, Y. Gao, and Z. Guo, "Formability of ABX₃ (X = F, Cl, Br, I) halide perovskites," *Acta Crystallogr B*, vol. 64, no. 6, pp. 702–707, 2008, doi: 10.1107/S0108768108032734.
- [40] T. A. Berhe *et al.*, "Organometal halide perovskite solar cells: Degradation and stability," *Energy and Environmental Science*, vol. 9, no. 2. Royal Society of Chemistry, pp. 323–356, Feb. 01, 2016. doi: 10.1039/c5ee02733k.
- [41] A. Kojima, K. Teshima, T. Miyasaka, and Y. Shirai, "Novel Photoelectrochemical Cell with Mesoscopic Electrodes Sensitized by Lead-halide Compounds (2)."
- [42] A. Kojima, K. Teshima, Y. Shirai, and T. Miyasaka, "Organometal halide perovskites as visible-light sensitizers for photovoltaic cells," *J Am Chem Soc*, vol. 131, no. 17, pp. 6050–6051, May 2009, doi: 10.1021/ja809598r.
- [43] J. H. Im, C. R. Lee, J. W. Lee, S. W. Park, and N. G. Park, "6.5% efficient perovskite quantum-dot-sensitized solar cell," *Nanoscale*, vol. 3, no. 10, pp. 4088–4093, Oct. 2011, doi: 10.1039/c1nr10867k.
- [44] H. S. Kim *et al.*, "Lead iodide perovskite sensitized all-solid-state submicron thin film mesoscopic solar cell with efficiency exceeding 9%," *Sci Rep*, vol. 2, 2012, doi: 10.1038/srep00591.
- [45] M. M. Lee, J. Teuscher, T. Miyasaka, T. N. Murakami, and H. J. Snaith, "Efficient hybrid solar cells based on meso-superstructured organometal halide perovskites," *Science (1979)*, vol. 338, no. 6107, pp. 643–647, Nov. 2012, doi: 10.1126/science.1228604.

- [46] O. Malinkiewicz *et al.*, “Perovskite solar cells employing organic charge-transport layers,” *Nat Photonics*, vol. 8, no. 2, pp. 128–132, Feb. 2014, doi: 10.1038/nphoton.2013.341.
- [47] J. Burschka *et al.*, “Sequential deposition as a route to high-performance perovskite-sensitized solar cells,” *Nature*, vol. 499, no. 7458, pp. 316–319, 2013, doi: 10.1038/nature12340.
- [48] M. Liu, M. B. Johnston, and H. J. Snaith, “Efficient planar heterojunction perovskite solar cells by vapour deposition,” *Nature*, vol. 501, no. 7467, pp. 395–398, 2013, doi: 10.1038/nature12509.
- [49] M. A. Green, A. Ho-Baillie, and H. J. Snaith, “The emergence of perovskite solar cells,” *Nature Photonics*, vol. 8, no. 7. Nature Publishing Group, pp. 506–514, 2014. doi: 10.1038/nphoton.2014.134.
- [50] M. Saliba *et al.*, “Cesium-containing triple cation perovskite solar cells: Improved stability, reproducibility and high efficiency,” *Energy Environ Sci*, vol. 9, no. 6, pp. 1989–1997, Jun. 2016, doi: 10.1039/c5ee03874j.
- [51] W. S. Yang *et al.*, “Iodide management in formamidinium-lead-halide-based perovskite layers for efficient solar cells.” [Online]. Available: <http://science.sciencemag.org/>
- [52] O. K. Simya, A. Mahaboobbatcha, and K. Balachander, “Compositional grading of CZTSSe alloy using exponential and uniform grading laws in SCAPS-ID simulation,” *Superlattices Microstruct*, vol. 92, pp. 285–293, Apr. 2016, doi: 10.1016/j.spmi.2016.02.019.
- [53] D. H. Kang and N. G. Park, “On the Current–Voltage Hysteresis in Perovskite Solar Cells: Dependence on Perovskite Composition and Methods to Remove Hysteresis,” *Advanced Materials*, vol. 31, no. 34. Wiley-VCH Verlag, Aug. 01, 2019. doi: 10.1002/adma.201805214.

- [54] P. Liu, W. Wang, S. Liu, H. Yang, and Z. Shao, "Fundamental Understanding of Photocurrent Hysteresis in Perovskite Solar Cells," *Advanced Energy Materials*, vol. 9, no. 13. Wiley-VCH Verlag, Apr. 04, 2019. doi: 10.1002/aenm.201803017.
- [55] E. W. Chang, J. Y. Huang, and Y. R. Wu, "Analysis of the hysteresis effect in Perovskite solar cells for the traditional and inverted architectures," in *Conference Record of the IEEE Photovoltaic Specialists Conference*, Institute of Electrical and Electronics Engineers Inc., Jun. 2020, pp. 0897–0901. doi: 10.1109/PVSC45281.2020.9300759.
- [56] Y. Rong *et al.*, "Challenges for commercializing perovskite solar cells," *Science*, vol. 361, no. 6408. American Association for the Advancement of Science, Sep. 21, 2018. doi: 10.1126/science.aat8235.
- [57] F. Wu, R. Pathak, and Q. Qiao, "Origin and alleviation of J-V hysteresis in perovskite solar cells: A short review," *Catal Today*, vol. 374, pp. 86–101, Aug. 2021, doi: 10.1016/j.cattod.2020.12.025.
- [58] B. Chen, M. Yang, S. Priya, and K. Zhu, "Origin of J-V Hysteresis in Perovskite Solar Cells," *Journal of Physical Chemistry Letters*, vol. 7, no. 5. American Chemical Society, pp. 905–917, Mar. 03, 2016. doi: 10.1021/acs.jpcllett.6b00215.
- [59] M. K. Rao, D. N. Sangeetha, M. Selvakumar, Y. N. Sudhakar, and M. G. Mahesha, "Review on persistent challenges of perovskite solar cells' stability," *Solar Energy*, vol. 218. Elsevier Ltd, pp. 469–491, Apr. 01, 2021. doi: 10.1016/j.solener.2021.03.005.
- [60] H. J. Snaith *et al.*, "Anomalous hysteresis in perovskite solar cells," *Journal of Physical Chemistry Letters*, vol. 5, no. 9, pp. 1511–1515, May 2014, doi: 10.1021/jz500113x.
- [61] P. Liu, W. Wang, S. Liu, H. Yang, and Z. Shao, "Fundamental Understanding of Photocurrent Hysteresis in Perovskite Solar Cells," *Advanced Energy Materials*, vol. 9, no. 13. Wiley-VCH Verlag, Apr. 04, 2019. doi: 10.1002/aenm.201803017.

- [62] Y. Rong *et al.*, “Tunable hysteresis effect for perovskite solar cells,” *Energy Environ Sci*, vol. 10, no. 11, pp. 2383–2391, Nov. 2017, doi: 10.1039/c7ee02048a.
- [63] Z. Li *et al.*, “Acid Additives Enhancing the Conductivity of Spiro-OMeTAD Toward High-Efficiency and Hysteresis-Less Planar Perovskite Solar Cells,” *Adv Energy Mater*, vol. 7, no. 4, Feb. 2017, doi: 10.1002/aenm.201601451.
- [64] W. Tress, J. P. Correa Baena, M. Saliba, A. Abate, and M. Graetzel, “Inverted Current–Voltage Hysteresis in Mixed Perovskite Solar Cells: Polarization, Energy Barriers, and Defect Recombination,” *Adv Energy Mater*, vol. 6, no. 19, Oct. 2016, doi: 10.1002/aenm.201600396.
- [65] S. Ravishankar *et al.*, “Influence of Charge Transport Layers on Open-Circuit Voltage and Hysteresis in Perovskite Solar Cells,” *Joule*, vol. 2, no. 4, pp. 788–798, Apr. 2018, doi: 10.1016/j.joule.2018.02.013.
- [66] H. S. Kim *et al.*, “Control of I-V Hysteresis in CH₃NH₃PbI₃ Perovskite Solar Cell,” *Journal of Physical Chemistry Letters*, vol. 6, no. 22, pp. 4633–4639, Nov. 2015, doi: 10.1021/acs.jpcllett.5b02273.
- [67] G. A. Sepalage *et al.*, “A facile deposition method for CuSCN: Exploring the influence of CuSCN on J-V hysteresis in planar perovskite solar cells,” *Nano Energy*, vol. 32, pp. 310–319, Feb. 2017, doi: 10.1016/j.nanoen.2016.12.043.
- [68] J. Wei *et al.*, “Hysteresis analysis based on the ferroelectric effect in hybrid perovskite solar cells,” *Journal of Physical Chemistry Letters*, vol. 5, no. 21, pp. 3937–3945, Nov. 2014, doi: 10.1021/jz502111u.
- [69] M. Kamran, M. Mudassar, M. R. Fazal, M. U. Asghar, M. Bilal, and R. Asghar, “Implementation of improved Perturb & Observe MPPT technique with confined search space for standalone photovoltaic system,” *Journal of King Saud University - Engineering Sciences*, vol. 32, no. 7, pp. 432–441, Nov. 2020, doi: 10.1016/j.jksues.2018.04.006.

- [70] V. Kumar and M. Singh, "Derated Mode of Power Generation in PV System Using Modified Perturb and Observe MPPT Algorithm," *Journal of Modern Power Systems and Clean Energy*, vol. 9, no. 5, pp. 1183–1192, Sep. 2021, doi: 10.35833/MPCE.2019.000258.
- [71] M. A. Elgendy, B. Zahawi, and D. J. Atkinson, "Assessment of perturb and observe MPPT algorithm implementation techniques for PV pumping applications," *IEEE Trans Sustain Energy*, vol. 3, no. 1, pp. 21–33, Jan. 2012, doi: 10.1109/TSTE.2011.2168245.
- [72] D. Beriber and A. Talha, "MPPT techniques for PV systems," in *International Conference on Power Engineering, Energy and Electrical Drives*, 2013, pp. 1437–1442. doi: 10.1109/PowerEng.2013.6635826.
- [73] R. Kumar, S. Khandelwal, P. Upadhyay, and S. Pulipaka, "Global maximum power point tracking using variable sampling time and p-v curve region shifting technique along with incremental conductance for partially shaded photovoltaic systems," *Solar Energy*, vol. 189, pp. 151–178, Sep. 2019, doi: 10.1016/j.solener.2019.07.029.
- [74] S. E. Babaa, M. Armstrong, and V. Pickert, "Overview of Maximum Power Point Tracking Control Methods for PV Systems," *Journal of Power and Energy Engineering*, vol. 02, no. 08, pp. 59–72, 2014, doi: 10.4236/jpee.2014.28006.
- [75] Jae Ho Lee, HyunSu Bae, and Bo Hyung Cho, "Advanced Incremental Conductance MPPT Algorithm with a Variable Step Size," *Institute of Electrical and Electronics Engineers (IEEE)*, Feb. 2009, pp. 603–607. doi: 10.1109/epepmc.2006.4778466.
- [76] M. Aly and H. Rezk, "An improved fuzzy logic control-based MPPT method to enhance the performance of PEM fuel cell system," *Neural Comput Appl*, vol. 34, no. 6, pp. 4555–4566, Mar. 2022, doi: 10.1007/s00521-021-06611-5.
- [77] P. Verma, R. Garg, and P. Mahajan, "Asymmetrical interval type-2 fuzzy logic control based MPPT tuning for PV system under partial shading condition," *ISA Trans*, vol. 100, pp. 251–263, May 2020, doi: 10.1016/j.isatra.2020.01.009.

- [78] T. Hiyama, S. Kouzuma, and T. Imakubo, "Identification of Optimal Operating Point of PV Modules using Neural Network for Real Time Maximum Power Tracking Control," *IEEE Transactions on Energy Conversion*, vol. 10, no. 2, pp. 360–367, 1995, doi: 10.1109/60.391904.
- [79] L. Zhang, Y. Bai', A. Ai-Amoudi, and P. Group, "GA-RBF NEURAL NETWORK BASED MAXIMUM POWER POINT TRACKING FOR GRID-CONNECTED PHOTOVOLTAIC SYSTEMS."
- [80] S. Srinivasan, R. Tiwari, M. Krishnamoorthy, M. P. Lalitha, and K. K. Raj, "Neural network based MPPT control with reconfigured quadratic boost converter for fuel cell application," *Int J Hydrogen Energy*, vol. 46, no. 9, pp. 6709–6719, Feb. 2021, doi: 10.1016/j.ijhydene.2020.11.121.
- [81] N. E. Courtier, G. Richardson, and J. M. Foster, "A fast and robust numerical scheme for solving models of charge carrier transport and ion vacancy motion in perovskite solar cells," *Appl Math Model*, vol. 63, pp. 329–348, Nov. 2018, doi: 10.1016/j.apm.2018.06.051.
- [82] T. Minemoto and M. Murata, "Device modeling of perovskite solar cells based on structural similarity with thin film inorganic semiconductor solar cells," *J Appl Phys*, vol. 116, no. 5, Aug. 2014, doi: 10.1063/1.4891982.
- [83] C. Zuo, H. J. Bolink, H. Han, J. Huang, D. Cahen, and L. Ding, "Advances in perovskite solar cells," *Advanced Science*, vol. 3, no. 7. Wiley-VCH Verlag, Jul. 01, 2016. doi: 10.1002/advs.201500324.
- [84] G. Kabadi and O. Ray, "Behavioral modeling of perovskite solar cells and study of its properties based on composition," in *9th IEEE International Conference on Power Electronics, Drives and Energy Systems, PEDES 2020*, Institute of Electrical and Electronics Engineers Inc., Dec. 2020. doi: 10.1109/PEDES49360.2020.9379804.

- [85] A. J. Cimaroli *et al.*, “Tracking the maximum power point of hysteretic perovskite solar cells using a predictive algorithm,” *J Mater Chem C Mater*, vol. 5, no. 39, pp. 10152–10157, 2017, doi: 10.1039/c7tc03482b.
- [86] A. Kumar, “Numerical modelling of ion-migration caused hysteresis in perovskite solar cells,” *Opt Quantum Electron*, vol. 53, no. 4, Apr. 2021, doi: 10.1007/s11082-021-02806-1.
- [87] H. Saito, D. Aoki, T. Tobe, and S. Magaino, “Development of a new maximum power point tracking method for power conversion efficiency measurement of metastable perovskite solar cells,” *Electrochemistry*, vol. 88, no. 3, pp. 218–223, 2020, doi: 10.5796/electrochemistry.20-00022.
- [88] O. Nwe, “Derivation and Numerical Approximation of the Quantum Drift Diffusion Model for Semiconductors,” 2004.
- [89] “8.1 Drift diffusion model Advanced theory 1 Basic Semiconductor Equations,” 2010.
- [90] N. E. Courtier, J. M. Cave, J. M. Foster, A. B. Walker, and G. Richardson, “How transport layer properties affect perovskite solar cell performance: Insights from a coupled charge transport/ion migration model,” *Energy Environ Sci*, vol. 12, no. 1, pp. 396–409, Jan. 2019, doi: 10.1039/c8ee01576g.
- [91] N. E. Courtier, J. M. Cave, A. B. Walker, G. Richardson, and J. M. Foster, “IonMonger: a free and fast planar perovskite solar cell simulator with coupled ion vacancy and charge carrier dynamics,” *J Comput Electron*, vol. 18, no. 4, pp. 1435–1449, Dec. 2019, doi: 10.1007/s10825-019-01396-2.
- [92] “Drift-Diffusion Model: Introduction Dragica Vasileska.”
- [93] N. J. Anderson, “A Python Implementation of a Drift-Diffusion Model to Capture Ion Migration in Perovskite Solar Cells,” 2021.

- [94] C. Yang, X. Shan, and T. Xie, “Insights of hysteresis behaviors in perovskite solar cells from a mixed drift-diffusion model coupled with recombination,” *Photonics*, vol. 7, no. 7, Sep. 2020, doi: 10.3390/PHOTONICS7030047.
- [95] W. Clarke, L. J. Bennett, Y. Grudeva, J. M. Foster, G. Richardson, and N. E. Courtier, “IonMonger 2.0: software for free, fast and versatile simulation of current, voltage and impedance response of planar perovskite solar cells,” *J Comput Electron*, vol. 22, no. 1, pp. 364–382, Feb. 2023, doi: 10.1007/s10825-022-01988-5.
- [96] A. D. K. Kenfack, N. M. Thantsha, and M. Msimanga, “Simulation of Lead-Free Heterojunction CsGeI₂Br/CsGeI₃-Based Perovskite Solar Cell Using SCAPS-1D,” *Solar*, vol. 3, no. 3, pp. 458–472, Aug. 2023, doi: 10.3390/solar3030025.